PEKKA LAURIKAINEN

Characterisation and Validation of the Microscale Testing of Fibre Matrix Interphases

PEKKA LAURIKAINEN

Characterisation and Validation of the Microscale Testing of Fibre Matrix Interphases

ACADEMIC DISSERTATION
Tampere University, Faculty of Engineering and Natural Sciences
Finland

Responsible supervisor and Custos	Assoc. Prof. Essi Sarlin Tampere University Finland	
Pre-examiners	Prof. Dr. rer. nat. Hanna Brodowsky HWTK Leipzig Germany	Dr. Maria Sammalkorpi Aalto University Finland
Opponents	Dr. Liu Yang University of Strathclyde United Kingdom	Assoc. Prof. Andrea Dorigato University of Trento Italy

The originality of this thesis has been checked using the Turnitin OriginalityCheck service.

Cover design: Roihu Inc.

HIILINEUTRAALI PAINOTUOTE

ClimateCalc CC-000025/FI
PunaMusta Printing

Carbon dioxide emissions from printing Tampere University dissertations have been compensated.

Dedicated to my mother, who – among many other things – taught me that everyone has their own challenges.

And more importantly that facing challenges makes you *better equipped to deal with them*.

And to my favourite storytellers who helped me absorb that lesson through a lens of wonder and *fantasy*.

Who, with their stories taught me that among the great forces of the world stands the indomitable human spirit. Bolstered, even created, by the connections – the *friends* – we meet along the way.

And without which, this book would never have been possible.

"In one fleeting moment, lives come and go. Ever moving towards the unknown. And in that fleeting moment, they cry for the answer to the question: Why, given life, are they meant to suffer. To die...

As fragmented, imperfect beings, yours is a never-ending quest. A quest to find your purpose, knowing your end is assured. To find the strength to continue, when all strength has left you. To find joy, even as darkness descends...

...And amidst deepest despair, *light everlasting...*"

PREFACE

Here we are, at a journey's end. And while it is my name on the cover, this would not have been possible alone. The research presented in this dissertation was carried out during 2018-2023 in the Materials Science and Environmental Engineering unit of Tampere University. The funding comprised mainly personal grants from the Tampere University Doctoral School and the Jenny and Antti Wihuri foundation. I am very grateful for the chance afforded by these grants to work practically full time on this dissertation.

I am also very grateful to my Supervisor, Associate Professor Essi Sarlin, who was able to guide and focus the sometimes incoherent jumble of my chosen topics of research into something worth publishing – and to even be little proud of. Without her support, guidance and time this book simply would not exist.

Of the many colleagues, friends and/or fellow sufferers of the path towards a doctoral degree – all of whom are deserving of my thanks – I would like to give special shout-outs to Sarianna Palola, Markus Kakkonen, Royson Dsouza, Farzin Javanshour, Olli Orell, Ilari Jönkkäri, Jarno Jokinen, Óscar Rodera García and Nazanin Pournoori. You made the journey memorable and much more fun than I ever expected. The rest of the Fibrobotics Oy team alongside Markus were also an absolute joy to work with – not to mention instrumental to this work (pun intended). I would also like to thank Associate Professor Mikko Kanerva and Assistant Professor Gaurav Mohanty for their contributions. I cannot thank you all enough!

Finally, I would also like to thank Tuire and the rest of my friends and family for being there. Your support – whether near or far – was there to lean on whenever it was needed. Kiitos ja anteeksi.

Tampere, September 2023

Pekka Laurikainen

ABSTRACT

The critical contribution of the interface – or interphase – to the final composite properties is a widely acknowledged pillar of the composite industry. However, many aspects of the composition and optimisation of interfacial performance remain closely guarded secrets in the halls of fibre manufacturers. Additionally, studies of the interphase, commonly through microcomposite characterisation methods such as the fibre pull-out or the microbond test, remain hindered by the overly argumentative discussion and haphazard approaches to studying them – the former being quite understandable considering the latter. Microcomposite testing has been frequently cited as suffering from large and unpredictable scatter of the experimental results, which can often – if not always – originate from poorly designed experimentation. While many great successes exist, they tend to get lost amidst a vast amount of unremarkable or even misguided work.

This work aims to lift these aforementioned successes, from our research and that of others, to the forefront. To use the data and analysis therein – supported by selected approaches from outside the topic of interphases and microcomposites – to build a more comprehensive overview of the topic of the interphase and its testing while simultaneously hoping to begin to solve the identified key issues limiting the microcomposite characterisation methods. The majority of the discussion presented in the work revolves around this field of topics: the methodology of microcomposite testing in quasi-static and cyclic loading, and the limitations and advantages of microcomposite testing. These are presented along with the improvements made to achieve the current state-of-the-art, developed in parallel to – and in part based on – this work. The primary aim was to achieve statistical reliability within microbond testing. This work demonstrates that the issue of experimental scatter could be mitigated effectively by a properly designed testing setup. What scatter remained in the data originated mainly from variations at the interphase and in the resin properties. The contributions from resin should be mitigated, and significant effort was

afforded to addressing this issue in the work. Variation of the interphase within the same fibre matrix combination was expected and represents an important aspect of understanding the overall performance of the interphases in composites.

For studies on the interphase, the dependency on resin properties remains an issue. To fully realise the potential of microcomposite testing, the methods should be applicable to most, if not all, fibre matrix combinations and offer comparable results at least for the same method. As the interphase cannot exist without the presence of resin, this problem can never be fully resolved. Instead, it needs to be understood and mitigated. This highlights the second major topic of this study: The degree of cure of the resin, specifically as a part of a microcomposite sample. Many methods are available to characterise the degree of cure at the macroscale but, as many research groups have recently demonstrated, the curing of picolitre volume droplet-on-fibre systems differs significantly from those of bulk resin. The easiest potential explanation was identified as surface-to-volume ratio and vapour pressure causing the volatile components of the resin to evaporate, and as a result the degree of cure of the droplet system remains at a much lower level compared to bulk. This theory holds for both two-component (resin/hardener) systems and reactive solvent systems such as epoxy resins and polyester resins, respectively. Both types of thermoset resins have been shown to suffer from similar issues in microcomposite curing. As direct characterisation of the droplet degree of cure is very challenging, the approach focused more on understanding the underlying phenomena and structure property relationships of the resin. Atomistic scale modelling along with experimental thermal analysis were used to understand the curing process and how it translates to resin properties, while the experimental comparison for mechanical performance was provided through nanoindentation – as close to scale as possible. The primary conclusion was that while the degree of cure has some effect on the final properties at all levels, above a critical threshold the effect becomes sufficiently minor to not affect the measurement itself. The differences in the curing states of the resin were noted to go beyond the expected dependence on degree of cure and evaporation-related changes in stoichiometry, highlighting the need for further understanding of the development of morphology in the curing resins.

Based on this work, several possible and quite universally applicable steps could be suggested to minimise the effect of resin conversion during microcomposite sample preparation. In order to have the most accurate analysis possible, the conversion-

related properties, such as modulus, strength and curing shrinkage, should be addressed droplet by droplet, but this goes beyond the scope of this work and remains an interesting future challenge. Another future topic highlighted by the results of this work is how the aspects of the resin conversion affect the overall structure of the interphase. The atomistic simulations presented in the work highlight the importance of non-covalent bonding to both the curing kinetics and network structure formation, and most of these findings have significant implications to the formation of the interphase as well.

x

TIIVISTELMÄ

Rajapinnan kriittinen rooli komposiittimateriaalien ominaisuuksien muodostumisessa on merkittävä komposiittiteollisuuden peruspilari. Jopa laajasti käytössä olevien komposiittimateriaalien osalta rajapinnan rakenne on kuitenkin monille tuntematon, sillä sen rakenneosat – itse hartsia ja kuitua lukuun ottamatta – sekä tutkimustyö nykyisten ratkaisujen takana ovat lujitekuituvalmistajien tarkoin varjelemia kauppasalaisuuksia. Rajapinnan tutkimusta puolestaan hidastaa usein käytettyjen mikrokomposiittimenetelmien huono maine, jonka taustalla on osittain huonolaatuiset mittaustulokset. Huonolaatuisella tarkoitetaan tässä yhteydessä vaikeasti toistettavaa ja suuren tilastollisen hajonnan omaavaa mittausta. Yleinen käsitys menetelmistä onkin, että niiden hajonta peittää kaikki mahdolliset merkittävät johtopäätökset eivätkä mittaukset ole vertailukelpoisia. Myös paljon laadukasta tutkimusta on tehty näiden menetelmien kehittämiseksi, sekä niitä hyödyntäen, mutta nämä onnistumiset edustavat vähäistä osaa kokonaisuudesta ja jäävät siksi herkästi huomiotta.

Tämän työn suurimpiin tavoitteisiin lukeutui tuoda näitä onnistumisia esiin sekä omasta että muiden tutkimustyöstä. Työssä pyritään käyttämään esitettyjä tuloksia – muun tutkimustyön tukemana – luomaan parempi käsitys rajapintatutkimuksen menetelmistä ja toivottavasti itse rajapinnasta. Osana tätä, työssä pyrittiin tunnistamaan ja ratkaisemaan avainhaasteita menetelmien kehitykselle sekä laajemmalle käyttöönotolle. Valtaosa työstä käsitteleekin tätä aihepiiriä: mikrokomposiittitestauksen menetelmien kehitystä, sekä menetelmien etujen ja rajoitteiden tunnistamista. Varsinainen mittauslaitteiston kehitystyö tapahtui muiden toimesta työn rinnalla ja osittain työn tarpeisiin perustuen. Kehitystyön tavoite oli statistisesti luotettavan microbond laitteiston kehitys. Tämä osa-alue työstä näyttää, että hajontaa saadaan pienennettyä merkittävästi asianmukaisella laitteen suunnittelulla. Jäljelle jäävä hajonta aiheutui pääosin rajapinnan ja hartsin ominaisuuksien vaihteluista. Näistä jälkimmäisen rooli tulisi pyrkiä minimoimaan ja tämän ongelman ratkaisu nousikin tärkeäksi osaksi työtä. Rajapinnan ominaisuuksien vaihtelu puolestaan on merkit-

tävässä roolissa osana kokonaisvaltaista ymmärrystä komposiittirajapintojen käyt-
täytymisestä.

Mittaustuloksen riippuvuus hartsin ominaisuuksista on merkittävä haaste mikrokom-
posiittitestien käytettävyydelle. Jotta menetelmien täysi potentiaali voidaan saavut-
taa, niiden tulisi olla käyttö- ja vertailukelpoisia mahdollisimman laajalle osalle mah-
dollisista kuitu-hartsi kombinaatioista. Rajapintaa ei kuitenkaan ikinä muodostu il-
man hartsia (tai kuitua), mikä tarkoittaa, että hartsi vaikuttaa vääjäämättä menetelmän
tuloksiin. Koska ongelmaa ei voida poistaa, se pitää sen sijaan ymmärtää ja sen
vaikutukset minimoida. Tästä muodostuu toinen työn aihekokonaisuus. Hartsin
kovettuminen ja tarkemmin sen rooli mikrokomposiittinäytteen käyttäytymiseen.
Makroskooppisten näytteiden kovettumisaste on määritettävissä laajasti saatavilla
olevilla testimenetelmillä, mutta mikrokomposiittinäytteiden koko ja tilavuus ai-
heuttavat merkittäviä haasteita. Tilavuudeltaan pikolitroissa tarkasteltavien hartsinäyt-
teiden kovettuminen eroaa merkittävästi yleisimpien sovelluskohteiden olosuhteista.
Tämä ongelma on jo aiemmin osoitettu useampien tutkimusryhmien toimesta ja
looginen selitys ilmiölle löytyy hartsin pinta-tilavuussuhteesta ja sen vaikutuksesta
hartsikomponenttien höyrynpaineeseen, mikä voi johtaa matalamoolimassaisten kom-
ponenttien haihtumiseen hartsiseoksesta. Hartsinäytteen lopullinen tila eroaa siis
merkittävästi niin sanotusta "bulkkinäytteestä" eli suuremmasta kovettuvasta tilavuu-
desta. Samankaltaista haihtumista ilmenee sekä kaksikomponenttihartseilla, että
reaktiivisiin liuottimiin perustuvilla hartseilla, kuten epoksit ja polyesterihartsit,
tässä järjestyksessä. Koska hartsipisaroiden kovettumisasteen suora määritys on lähes
mahdotonta, tässä työssä keskityttiin tutkimaan kovettumisreaktioon vaikuttavia
ilmiöitä ja hartsien kemiallisen rakenteen ja ominaisuuksien riippuvuutta. Atom-
iskaalan mallinnuksen ja kokeellisen termisen analyysin menetelmillä pyrittiin keräämään
tietoa kovettumisreaktion etenemisestä hartsissa ja miten ne johtavat hartsin eri omi-
naisuuksiin. Mekaanisten ominaisuuksien osalta kokeellinen vastine saatiin nanoin-
dentaatiolla suoraan oikean mittakaavan näytteistä. Hartsin ominaisuuksien tärkein
rooli mittaustulokseen on hartsin johdonmukainen käyttäytyminen mittausten aikana.
Tämä saavutetaan useimmissa tapauksissa, kun kovettumisaste ylittää tietyn kriit-
tisen tason. Kovettuneen hartsin käyttäytymisessä havaittiin myös merkittäviä eroja
erilaisten kovettumista edesauttavien lämpökäsittelyjen seurauksena. Nämä erot eivät
korreloineet määritetyn kovettumisasteen kanssa eikä voida myöskään selittää haih-
tumisesta aiheutuvalla stoikiometrian muutoksella. Tutkimuksen seurauksena havait-

tiinkin tärkeäksi ymmärtää myös hartsin morfologian muodostumien kovettumisen edetessä.

Työssä kerrytetty teoreettinen pohjatieto hartsin kovettumisen ilmiöistä mahdollistaa hartsikohtaisia ratkaisuja kovettumisen roolin minimointiin mikrokomposiittinäytteiden valmistuksessa. Mahdollisimman tarkan analyysin saavuttamiseksi olisi kuitenkin syytä tarkastella hartsin ominaisuuksia näytekohtaisesti, sillä ne voivat vaihdella jopa samankaltaisten näytteiden välillä. Näin yksityiskohtainen tarkastelu on kuitenkin tämän työn aihepiirin ulkopuolella ja on yksi seuraavien kehitysasteiden merkittävistä haasteista. Toinen työssä esille noussut tärkeä aihepiiri on hartsin kovettumisen rooli rajapinnan kemiallisen rakenteen muodostumisessa. Työssä esitetyt atomiskaalan mallinnustulokset osoittavat ei-kovalenttisten sidosten – pääosin erilaisten vetysidosten – vaikutuksen tärkeän roolin kovettumisreaktion etenemisessä sekä hartsin rakenteen muodostumisessa, joilla on suora yhteys myös rajapinnan rakenteeseen.

CONTENTS

List of Tables

ABBREVIATIONS

CA   Coupling agent, a compatibiliser between a non-organic fibre surface and organic polymer.

DFT   Density functional theory, a computational chemistry method for faster approximations of the results of *ab initio* calculations.

DGEBA   Diglycidyl ether of bisphenol-A, a common epoxy prepolymer and vinyl ester precursor.

e.g.   for example, from Latin *exempli gratia*.

et al.   and others, from Latin *et alii*.

FBG   Fiber Bragg grating, optical fibre sensing technology based on manufactured regions of varying refractive index. Facilitates monitoring strain in the fibre, for example.

FEA   Finite element analysis, a computational method for solving mechanics problems at various length scales based on input material models and structures.

FRC   Fibre-reinforced composite, a group of materials comprising fibre reinforcements and a matrix material binding the fibres together.

FTIR   Fourier transform infrared spectroscopy

GPU   Graphical processing unit, an additional computing unit utilised in computers for efficient parallelisation of specific computation tasks such as computer graphics or particle simulations.

i.e.   that is, from Latin *id est*.

IFSS   Interfacial shear strength, the most commonly used term for the strength of the interface/interphase

IPN   Interpenetrating network, a mainly conceptual structure of two crosslinked networks mixing with little to no actual covalent bonds between them.

m-PP   Maleated polypropylene, a functionalised polypropylene copolymer to introduce large polar sidegroups in the form of maleic anhydrite

MD   Molecular dynamics, a computational chemistry/physics method for predicting the responses of chemical structures to certain sets of conditions.

TGA   Thermogravimetric analysis.

UP   Unsaturated polyester, a thermoset resin cured through polymerisation of the reactive solvent styrene and unsaturated polyester oligomers.

VE   Vinyl ester, like unsaturated polyester but the crosslinking component is a vinyl ester prepolymer (often epoxy-based).

w-%   Percent weight, signifying the weight of a component of the total weight of the material or solution in percentage.

SYMBOLS

A_{emb} Embedded area, the total surface area of contact between the fibre and the matrix in microcomposite samples. Calculated from L_{emb} and ϕ_{fibre}.

E_f Fibre Young's modulus.

E_m Matrix Young's modulus.

F_d Debond force, the force level required to initiate debonding damage during a microcomposite test. Lower than F_{max} as the friction and thermal stresses contribute to the overall measured force.

F_{fric} Friction force, the friction component of the total force measured during a microcomposite test. Determined either from the behaviour of F_d in relation to F_{max} or from the sliding friction of a debonded droplet.

F_{max} Maximum force, the peak force measured in a microbond test.

G_c Critical energy of debonding, a parameter representing the energy associated with damage propagation at the interphase in the traction-separation law utilised in FEA.

G_f Fibre shear modulus.

G_m Matrix shear modulus.

V_f Fibre volume fraction, volumetric portion of the embedded fibre in a microcomposite sample.

V_m Matrix volume fraction, as V_f but for the matrix resin.

α_f Fibre coefficient of thermal expansion.

α_m	Matrix coefficient of thermal expansion.
β	The shear lag parameter, two variants are used in this work: Nayfeh (β_N) and Cox (β_C) shear lag parameters.
$\phi_{droplet}$	Diameter of the droplet, the maximum value along the droplet edge profile.
ϕ_{fibre}	Diameter of the fibre.
τ_T	The thermal component of stress in a microbond test.
τ_c	Critical stress, a parameter representing stress level of damage onset at the interphase in the traction-separation law utilised in FEA.
τ_d	Debonding stress, the strength of the interphase.
τ_{fric}	The friction component of stress in a microbond test.
τ_{app}	Apparent interfacial shear stress, often also denoted as IFSS.
l_{emb}	Embedded length, the length of fibre embedded in matrix. In microbond, the distance between the ends of the droplet menisci.
r_f	Fibre cross-sectional radius.
T_g	Glass transition temperature, the temperature at which the chain mobility of an amorphous polymer phase changes leading to a glass-melt transition significantly affecting heat capacity and expansivity.

ORIGINAL PUBLICATIONS

Publication I   P. Laurikainen, M. Kakkonen, M. von Essen, O. Tanhuanpää, P. Kallio and E. Sarlin. Identification and compensation of error sources in the microbond test utilising a reliable high-throughput device. *Composites Part A: Applied Science and Manufacturing* 137 (2020), 105988. ISSN: 1359-835X. DOI: `10.1016/j.compositesa.2020.105988`.

Publication II   P. Laurikainen, R. Dsouza, M. Kakkonen, M. Kanerva and E. Sarlin. Exploring the role of fibre sizing to the fatigue of glass fibre composites using a novel, reliable micro-fatigue test. *Composites Part A: Applied Science and Manufacturing* (2023), 107425. ISSN: 1359-835X. DOI: `10.1016/j.compositesa.2023.107425`.

Publication III P. V. Laurikainen and E. L. Sarlin. Cut-off Scale and Complex Formation in Density Functional Theory Computations of Epoxy-Amine Reactivity. *ACS Omega* 6.44 (2021), 29424–29431. DOI: `10.1021/acsomega.1c03229`.

Publication IV   P. Laurikainen, S. Bhusare, G. Mohanty and E. Sarlin. Length-scale discrepancy in the properties of epoxy resin specimens. *Polymer* 283 (2023), 126148. ISSN: 0032-3861. DOI: `https://doi.org/10.1016/j.polymer.2023.126148`.

AUTHOR'S CONTRIBUTION

Publication I   The author conducted the experiments along with M. Kakkonen, analysed the results and prepared the first draft with M. Kakkonen. M. Kakkonen was also responsible for the method development along with M. von Essen and O. Tanhuanpää.

Publication II   The author conducted the experiments and prepared the manuscript along with R. Dsouza. The author also prepared all the samples and analysed the experimental results. R. Dsouza performed the FE simulations with valuable input and suggestions from M. Kanerva. M. Kakkonen was responsible for the development of the experimental setup with suggestions from the author and R. Dsouza.

Publication III   The author conducted all the DFT computations and the analysis of the results and prepared the manuscript.

Publication IV   The author performed the thermal analysis experiments and the simulation work and prepared the first draft of the manuscript. The test matrix and selection of sample types for nanoindentation was a joint effort by all authors. S. Bhusare conducted the nanoindentation experiments and analysis with input and suggestions from G. Mohanty.

The co-authors provided valuable inputs and suggestions to all drafts leading to the published manuscripts and helped outline the goals and concept of each manuscript through text and discussions both.

xxx

1 INTRODUCTION

One can scarcely argue that the importance of fibre-reinforced composite (FRC) materials has been – and is still – increasing in high-end engineering applications. The combination of high specific strength and tailorability through the vast selection of available components often makes FRC the only real option for lightweight structures intended for long-lasting use. This is especially true for applications where corrosive or other aggressive environments are expected or even intended, as the main contenders – metals – are usually either unsuited, too heavy or too expensive for the intended application. With proper design, glass and carbon-fibre-reinforced materials can easily replace or even surpass metals in many applications. However, the design and manufacturing of an FRC part differs in most ways from that of a metal part, making a "drop-in" replacement often impossible, instead requiring complete redesign to incorporate the FRC. Both materials have their own complexities, but the anisotropy and complex nature of the composite components presents many unique challenges.

To achieve optimal properties, every part of the composite needs to function as intended. In addition to proper selection of the material and the manufacturing method, the design needs to consider a multitude of factors ranging through multiple length scales. Taking a thermoset resin as an example, everything from mixing with proper stoichiometric ratios, reaction times for the curing (i.e. pot-life), fibre layup and load transfer to rheology, proper curing and post-curing conditions, wetting of the fibres and the interplay of the separate components contributes to the durability of the final component – namely through the functionality of the interphase. All this needs to be properly considered to create a durable final product. Failing at even one can lead to severe consequences, which might not be immediately notable but might break the part decades before the intended end of use. And where thermoset-based FRCs are considered, these failures are often catastrophic or at the very least extremely difficult to repair. Couple this with the inherent difficulties with reuse and

recycling of End-of-Life (EoL) composite waste, "good enough" is rarely an option these days.

To dive even deeper into the issue, some of these aforementioned aspects are still less than fully understood. The greatest unknowns are related to the interphase – i.e. the region between the fibre reinforcement and the bulk resin matrix formed from mixing and interacting of the matrix with the fibre surface treatment known as a sizing. This region is often considered a separate third component of a composite material, as it is absolutely critical in maximising the properties of an FRC [1, 2]. However, as cannot exist without the other two main components, characterising its structure and properties has proven to be a difficult challenge.

The main issue should be quite evident at this point. The level of scientific progress behind composite materials is not as well developed as e.g. the corresponding knowledge for metals. In metallurgy, understanding of the material is well established throughout the scale hierarchy, and the different physical and chemical – and at higher length scales morphological – phenomena can be predicted with suitable accuracy and their importance to another scale can be predicted with already established methodology. Naturally, this is a generalisation and applies best to the "everyday materials" of the group. The situation is completely different for composites, as the aforementioned unknowns exist just as much in materials discussed in terms of tonnage annually as they do in emerging materials just conceived in research labs.

Hence, to reach a similar technological level with FRCs, reliable methods of characterising the interphase are a natural next step towards better understanding the materials. This is especially true in terms of the long-term durability – including both physico-chemical phenomena (ageing) and fatigue caused by mechanical loading cycles. As such, the exploring and improving of the selection of experimental methods and the chemical structure of the interphase represent interesting challenges and are the primary topics of this dissertation. The following Chapters present the scientific basis of the interphase, the methodologies used to study it and the detailed scope and aims of the work, summarising the most important aspects of this research in terms of methodology, key results, discussion and final conclusions. The main body of work is represented in the four original research articles included at the end of this thesis.

2 SCOPE AND AIMS

This study aims to improve the current state-of-the-art of microscale interfacial testing and to spread the information on best practices identified from both literature and the experimental improvements tested in this work. The current contradictory and overly argumentative scientific discussion on the topic is one of the biggest current hindrances to progress. Therefore, the core tenet of this work has been from the outset to collect and disseminate as much of the multidisciplinary knowledge required to solve or mitigate the biggest points of conflict and uncertainty related to microscale interfacial testing as possible. Several experimental approaches for such tests have been proposed, and those most widely employed are discussed in Section 3.2. This study utilises and further develops the approach known as the microbond test. In addition to seeking to identify best practices, this core tenet included evaluating and combining existing theories on the structure and formation of the interphase to then identify what requirements the interphase itself sets on the methodology.

The identified scientific gaps and the approaches to solve them have been formulated into four key research questions (RQ), which are as follows:

RQ1 The microbond test is under much scrutiny as an arduous and inconsistent experimental approach. Can state-of-the-art improvements to the experimentation result in a reliable and versatile testing system? (Publications I, II and IV)

RQ2 What conclusions about the interphase structure can be drawn from the results of state-of-the-art microcomposite testing? (Publications II and IV)

RQ3 What is the role of non-covalent bonding in epoxy curing and fibre-matrix interphase formation? (Publication III)

RQ4 How does the length scale and the surrounding environment affect the properties of a microcomposite sample? Can we quantify the difference to bulk resin samples? (Publications I, III and IV)

3 SCIENTIFIC BACKGROUND

3.1 Chemistry of the interphase

The discussion and research around fibre sizings and the interphase tend to focus around glass fibres due to their complex nature. Without tailoring the interactions between the glass surface and the polymer matrix, the very limited interactions between the disparate materials cause a fundamental problem to the functionality of the composite: inadequate stress transfer. The interphase needs to also maintain this stress transfer capability throughout the lifetime of the material, through the environments and loading states and the variations it can experience.

For other reinforcements, such as carbon fibres, the situation is somewhat easier, if not necessarily simpler, due to the fact that "like attracts like" – a well-known core tenet of chemical interactions. As most polymers used in FRCs are carbon-based with polar functional groups, they are already somewhat capable of non-covalent interactions with the fibres, and thus requiring little – if any – interphase tailoring [3]. This along with compressive forces is sufficient for the needs of many carbon fibre FRC applications and routes for further improvement are also actively studied [4, 5]. The more recently emerging natural fibre reinforcements share similar advantages with carbon fibres. Therefore, due to the compositionally more complex case and especially their significantly more widespread use, this work focuses mainly on glass fibres – pointing out some commonalities with other fibre types where applicable.

For the matrix, the discussion will mainly focus on thermosetting resins with a strong emphasis on epoxy. Epoxy resins represent the widest range in performance and applications in current state-of-the-art and are therefore the logical starting point for this type of study. Another reason for selecting epoxy for laboratory-scale work is the use of styrene as reactive solvent in unsaturated polyester (UP) and vinyl ester (VE) resins, which carries inherent workplace safety implications. The applicability

of the various approaches to other resins can be discussed separately, but generally most experimental approaches and concepts excluding the direct chemical bonding of the resin to the fibres should be directly applicable from epoxies to other thermoset and even thermoplastic resins as long as the differences are carefully considered. For example, vinyl ester resins share much of their chemical functionality with epoxies but differ significantly in their curing, while the molecular mobility thermoplastic polymer chains are vastly different to that of thermoset prepolymers (mono and oligomers).

3.1.1 Fibres and matrix

While the region we consider the interphase is in large part a result of the sizing applied on the fibre surface, the only logical starting point of discussion is the contribution of the primary components – the fibre and the matrix. This is due to the fact that without them there is also no interphase – causing significant challenges in measuring and determining the properties of the interphase. In addition to setting the limits of performance achievable for a given combination, the fibre and matrix also have crucial a role in the environmental durability of the composite. While the ageing is not the topic of this study, the complex physico-chemical interactions involving all three components of the composite are very indicative of the overall structure and crucial to the reasoning behind the selection of the components – making them relevant background information for further discussion.

The glass fibre surface is a morphologically unique form of glass. Luckily for those among us seeking to bond it with organic materials it is already somewhat functionalised with silanol groups [6, 7]. While this functional surface can already provide some non-covalent interactions – and therefore strength to the fibre-matrix interface – the glass and polymer tend to be too dissimilar to allow for any type of effective stress transfer through such a limited region of space. Such an interphase would also be extremely vulnerable to various environmental conditions, with moisture being among the most significant among them. Hydrogen-bonded structures can interact with water molecules to create hydrogen-bonded networks that expand the structure and weaken the interphase. This vulnerability to moisture is frequently cited as the primary reason for the use of silane coupling agents (CA) [6, 8]. While the discussion over whether or not this proves the presence of covalent bonding of

the silane remains on-going, an inarguable wealth of data clearly shows that an un-sized interphase has very poor durability in hydro- or hydrothermal conditions for all fibre types [6, 7, 8, 9, 10]. Another factor directly related to the glass fibre is the durability of the glass itself. An unfortunately common misconception that glass fibres are an inert part of the composite material during ageing conditions persists in the composites industry. The critical issue of boron content in E-glass has largely been solved in the industry by replacing E-glass with more durable grades – usually ECR glass. It is, however, important to understand that even ECR glass is resistant to ageing in the aqueous environments due to the formation of an equilibrium state. This means the ageing can penetrate only a limited distance into the glass structure. The surface of the glass is still leached of some of its non-silica components, especially if an acidic medium is responsible for the ageing, and the specific effects this has on the interphase region remain unknown [11].

The role of the matrix in the interphase is also quite complex. Thermosetting resins are generally mixed to stoichiometric ratios of epoxide/hardener to maximise the resin properties. Unreacted resin or hardener acts as a plasticiser in the structure and tends to also provide free volume for moisture to penetrate into the structure – furthering the plasticising effect in addition to enabling other ageing effects. CAs and the film former, for the sake of compatibility, are often selected with the same functional groups as the resin system, e.g. aminosilanes and epoxide functional silanes for epoxy matrices. These functional groups are outside the consideration of the resin stoichiometry, and while some are likely used for bonding between the CA and film former, a significant number can be expected to be available for interaction with the matrix as well. Therefore it is probable that the interphase region contains a large number of unreacted functional groups, thus remaining quite ductile due to the prominence of non-covalent interactions and plasticising material in its structure, which can even be advantageous to the overall performance through stress relaxation and prevention of irreversible damage formation at the interphase [6, 7, 9].

3.1.2   Sizing formulation

The foundation of glass fibre coupling with the polymer matrix is a component frequently nominated as the coupling agent (CA). For glass fibres the most effective

CAs are usually organosilanes with a single longer organic side-chain. The original hypothesis for the functionality of these silanes was that after the hydrolysis of the small side-groups the silanol groups of the CA would bond with the silanol groups of the glass surface, forming a covalently bonded organic surface for the glass. This organic coating could then, in turn, bond with the polymer matrix. The increase in interfacial properties for this type of surface treatments has, however, been noted as significantly lesser than expected [12] for a fully covalently bonded structure. The ever-present water in the fibre manufacturing and sizing process [1] offers at least a part of the explanation, as the chemical bonding of the silanols in the presence of water will likely find an equilibrium of covalent and hydrogen-bonded structures [6]. This is supported by the reported results that hygrothermal ageing is a two-step process with only a long exposure or very harsh conditions leading to interfacial damage due to moisture absorption [13, 14]. Too much CA can even be detrimental for interfacial performance [6, 7], as the CA forms thicker weakly bonded multilayer structures with increasing concentration. Further studies of optimal sizing formulations highlight the importance of another important component to maximising interfacial properties – the film former.

This film former is a small molecular weight polymer or prepolymer – similar to the intended matrix – and compatible with both the CA and the resin. The original purpose of the film former was likely mainly the protection and improved handling of the fibres during transportation, and subsequent dissolving into the matrix and its importance to interfacial properties was only discovered through further studies on the topic [2, 15]. Proper formulation of the sizing, including the amount and the chemical nature of the film former, are crucial to the final interfacial properties of the composite, for both glass and carbon fibres [16]. The film former – as discussed earlier – can also plasticise the interphase, which is beneficial in moderation, but too much film former will reduce the overall performance [17].

The selected components – and the exact composition – of a sizing are closely guarded trade secrets of the fibre manufacturers. Certain chemicals have, however, been established as common or at least representative components in the scientific discussion on the subject [15]. Some of the most prominent have been collected here for reference. Table 3.1 presents the names and structures, along with their use cases, for silane CAs. Table 3.2 presents the similar information for film formers.

While the mechanism of bonding to the glass fibre surface requires the presence of

Table 3.1 Prominent CAs used in glass fibre sizing formulations.

Name	Structure	Notes
Amino silane		Most common is APTES†
Epoxy silane		Excess amine generally preferable

†Aminopropyl tri*ethoxy* silane, i.e. $R = CH_2 - CH_3$
‡$R_1 = Me/CH_2 - CH_3$, $R_2 = Me/O - Me/CH_2 - CH_3$
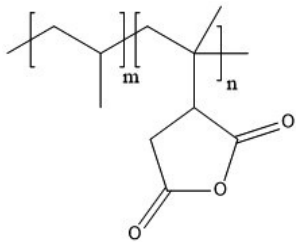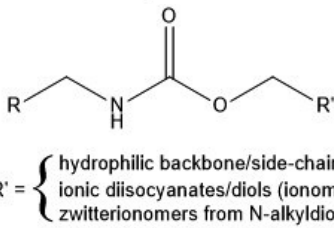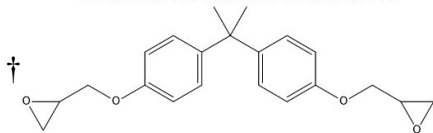
silanol groups, organosilanes (as presented in Table 3.1) are used instead. The oxygen bridges to the small organic side groups are easily hydrolysed to achieve the required structure, but the storage stability is greatly improved. Both methoxy and ethoxy groups are frequently used. The small change in reactivity is likely a balancing act between storage stability and easier hydrolysis in the use case – i.e. methoxy groups are more stable and ethoxy groups easier to hydrolyse. The most common of these examples – at least in scientific literature – is aminopropyl triethoxy silane (APTES).

The hydrolysis step needs to be taken into account in the process of creating the sizing solution. For this reason, the pH of the sizing solution is often reduced with the addition of weak acids to help hydrolyse the oxygen bridges. This can be a separate step in the sizing preparation process, as the solution pH should be restored to neutral before its use with the fibres: the acidic pH hinders the formation of the siloxane bridges with the glass surface.

In the literature available on sizing components, APTES and other epoxy compatible CAs dominate the discussion as they often show comparable – if not better – performance than CAs selected based on matrix compatibility [2]. This result indicates that the most crucial compatibilities at the interphase are: 1) between the CA and the film former and 2) between the film former and the resin. This also hints at a possible structure for the interphase, which constitutes one of the core hypotheses of this dissertation.

Table 3.2 Common film former polymers and "pre-polymers" used in glass fibre sizing formulations.

Name	Structure	Notes
Maleated polypropene (m-PP)		Anhydride content generally $\leqslant 1$ w-% [18, 19]
Polyurethane (PU)	R/R' = { hydrophilic backbone/side-chains, ionic diisocyanates/diols (ionomers), zwitterionomers from N-alkyldiols	Ionic and non-ionic dispersions [20]
Epoxy	†	DGEBA‡ a common example.

†Oligomer content possible but not presented in Figure. ‡Diglycidylether of Bisphenol-A.

3.1.3 The interphase hypothesis

The current understanding of the formation of the interphase, which accounts for the importance of both major components, is thus that the silane does indeed bond with the glass surface. However, the simplified assumption of a monolayer with organic side-chains pointing out of the surface is indeed just that – a simplification. Based on extraction studies done on effective sizing formulations, the CA likely forms a silane moleculee layer of several Ångstroms, bonded with a mix of covalent and non-covalent bonds [7]. The assumption of covalent bonding with the resin is far less likely than covalent bonding with the film former, when applicable, which would lead to a structure more similar to an interpenetrating network (IPN) of partly crosslinked sizing and partly crosslinked matrix with significant non-covalent interactions between the two.

The current hypothesis of the interphase structure is therefore a gradient shift in composition from CA-dominated to film former and finally matrix-dominated re-

gions each comprising interpenetrating networks of the different components. This type of interphase can be expected to be more ductile than stiff and brittle – as explained by the covalently bonded hypothesis – owing to the large contribution that different non-covalent bonds make to the overall structure. This would therefore also explain the reported results of higher IFSS – or some other measured interfacial property – not corresponding with a better composite. Stress transfer capability is the key, and it is not difficult to understand how a structure capable of withstanding deformation without breaking can endure longer than a strong but easily damaged or brittle structure. Low-stress cyclic loads are among the key failure types of any material – with composites being no exception [21, 22] – and fatigue life is considered a significant design limitation in many application fields [21, 23].

The structure of a glass fibre - polymer interphase in a properly designed composite structure is a composition gradient of the CA, the film former and the polymer matrix. The first network is mainly formed by the CA and the film former, while the second is formed by the polymer matrix. A schematic representation of this structural hypothesis is presented in Figure 3.1.
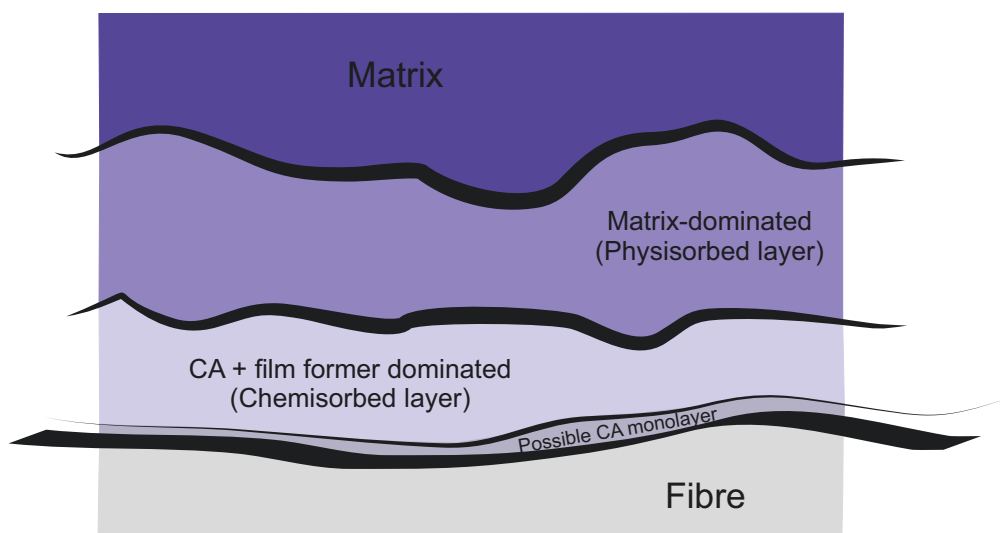
Figure 3.1   Schematic representation of the proposed interphase structure.

A similar structure is also expected from CF composites with the obvious exception of no CA in the structure. The film former bonds directly with the fibre surface. This bonding is mainly non-covalent in nature, but some covalent bonding is certainly possible if suitable functional groups are available [24]. Similar non-

covalent bonding between the fibre surface and film former can also exist in glass fibres, but the more similar chemical nature of the CA should in theory make it the more preferred option.

Despite being hinted at in previous literature [1, 2, 7], this potential structure for the interphase is rarely discussed. The foundational studies are based on silane CAs deposited and analysed on glass plates. Thomason [1] points out that, while valuable, this approach disregards major components of the sizing and the interphase in the film former and the processing aids that make up the bulk of the sizing formulation. Dey et al. [2] describe that this is because the film former and processing aids are assumed to dissolve into the resin, but they also highlight that this assumption is likely false. The film formers used in glass fibre sizings are actually mostly epoxies and have the potential to react with the CA and the resin [2]. The assumption of the dissolution of film former originates from fibre sizings used outside the composite industry. The combination of these two theories – the "dissolving" of the film former into the resin and the bonding of the film former onto the CA – results in the logical conclusion of the formation of an IPN between the sizing and the resin components. There is also a good probability of some of the unreacted film former functionality reacting with the resin mixture. This can lead to a dual outcome of some covalent bonding between all components of the interphase and local deviation from stoichiometry in available functional groups – assuming the film former comprises only epoxy or amine.

Scholtens and Brackman [25] explored the role of film formers with thermoplastic matrices. They found that the film former does not diffuse into the matrix and is instead the primary interacting component, with the matrix resulting in a larger contribution to interfacial performance than the CA. This is actually in line with the aforementioned interphase hypothesis, if one considers the significantly lesser molecular mobility of thermoplastic materials compared to unreacted thermoset resin components.

Gorowara et al. [15] analysed the compositions of deposited and extracted sizings deposited on glass fibres. Their study revealed a significant difference in film former retention in relation to film former reactivity. Their work also highlighted the importance of overall sizing reactivity to the creation of a reactive and stable interphase and the resulting composite performance in interlaminar shear stress (ILSS) and ageing durability [15]. The study concluded that thermodynamic equilibrium rather

than diffusivity was the more probable limiting mechanism to the interphase formation – at least with the vinyl ester resin used in the study. This leads to the conclusion that, while some interdiffusion of interphase components is definitely possible or even likely, the concentration of sizing components near the glass surface is high regardless of the various components of the interphase being compatible, reactive or non-reactive with each other.

Dey et al. [2] tested different film formers and CAs with high-performance S-glass. They concluded that the best performance by far was achieved with a CA-film former combination that enables both chemical crosslinking as well as physical adsorption. The highest performing example was an aminosilane (APTES) with a silylated polyazamide film former [2]. The latter is a rare example of a silane functional film former – with a very high amine content – giving it a very high potential for reactivity and high polarity. While an extreme example, it highlights some interesting tailorability options for the interphase. The more conservative but still highly performing interphase was achieved in the study by combining both epoxide and amine functional silanes with a Michelman Hydrosize polyurethane film former [2]. The reactive functional groups in the film former were identified as primary amine and hydroxyl end groups, which explains the performance difference between the sizing with epoxy functional silanes and only aminosilanes – the amine and epoxide groups are very reactive, whereas there is almost no potential for covalent bonding with the aminosilane.

In her dissertation, Petersen [26] cites many of the same or similar literary references and proposes a largely similar hypothesis for the interphase structure. The dissertation also presents a comprehensive collection of experiments on sizing extraction and multiscale interfacial testing. Petersen provides some insight into the chemical structure of commercial sizings outside the film former and coupling agent based on their analysis of extracted sizing components. Unfortunately, the microbond testing included in the work suffers from many of the common shortcomings, and the analysis remains somewhat inconclusive outside of the contributions from varying the mixing ratio of epoxy and amine also reported elsewhere [27].

So far, no study has provided a definitive answer to the structure and formation of the interphase region. But the hints are there, and together the aforementioned studies paint a fairly comprehensive picture of the interphase as a complex layer of covalently and physically bonded molecules that retains a lot of its chemical func-

tionality and therefore its potential for reforming both covalent and non-covalent bonds based on the prevalent equilibrium conditions. This would also mean a potential to retain or reattain some of its stress transfer capability between the matrix and the fibre even after the initial equilibrium conditions are altered by mechanical loading or environmental factors. In this dissertation, this hypothetical interphase structure is considered 'optimal,' and most discussion on experimental data concerning the interphase includes reflection on whether it supports this hypothesis.

3.2 Microscale testing methods in interphase studies

Microcomposite tests have been steadily growing in popularity for characterising the interphase instead of the more standardised larger length scale testing schemes such as the interlaminar shear strength (ILSS) test or fibre bundle tests. The advantages of observing the behaviour at a scale more representative of the interphase region are fairly evident. The decades of development with these methods are, however, also filled with problems and critique, not to mention almost straight up contradictory reports on results and phenomena. Trying to measure something that cannot exist on its own leads to no end of problems.

Despite the problems, the improvements have been constant, and slowly but surely the microcomposite tests have established themselves as the go-to methods for interphasial characterisation. Three major sub-groups of microcomposite tests are widely used for this purpose: the fibre pull-out test, the fibre push-out test and the microdroplet or microbond test. Schematic presentations of the core principle of each are presented in Figure 3.2.

The first of these measures the force required to pull a short length of fibre reinforcement out of a drop or well of resin that is attached to a surface. Since the only gripping required takes place at the end of the fibre, this method can generally measure even fairly short fibre samples. Due to the possibility of still having a fairly large resin well, the curing process of a thermoplastic sample resembles that of a bulk sample, which helps mitigate some of the possible length scale related issues in curing [28, 29, 30]. Analytical theories for analysing the results have been developed alongside those for the microbond test and follow the same basic principles. The biggest issues of the method relate to difficulties in specifying the embedded length, placing the fibre accurately to the middle of the resin well and extremely arduous
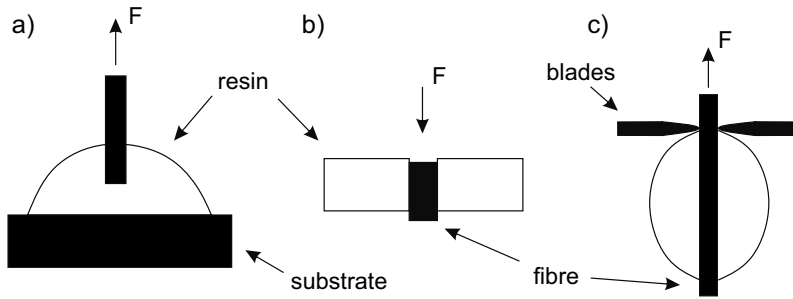
Figure 3.2 Fibre pull-out test a), fibre push-out test b) and microbond test c).

sample preparation and testing.

The fibre push-out test tends to be extremely varied in its application, but the best success has been experienced with nanoindenter-type setups [24]. The methodology is fairly straightforward, often involving thin composite parts from which the embedded fibre is pushed out and the required force is measured. The only obvious drawback of the methodology is the difficulty in preparing thin, high-quality samples for testing and uncertainty in how this sample preparation affects the the material, especially at the interphase region. However, similar levels of uncertainty exist in various parts in all comparable state-of-the-art methods as previously highlighted for the fibre pull-out method.

The last of the three, i.e. the microbond test, was studied extensively in this work. Originally developed by Miller et al. [31], the microbond test comprises a resin droplet deposited on the surface of a single reinforcement fibre and sheared along the fibre via microvice blades to cause a debonding of the resin droplet from the fibre. Due to the need to grip the fibre from one or both ends and still have sufficient space to manoeuvre the microvice blades in between, the minimum fibre length is generally longer than for the pull-out test, and the droplets need to be suitably small to control the embedded length and avoid fibre failure. Problems and inconsistencies compared to larger length scale samples have been noted in the curing of such small volumes of thermoset resins, causing some uncertainty in analysing the results, as the resin properties are unknown [28, 29, 30, 32, 33].

The basic requirements and concepts for accurate measurement for microbond were already discussed by Miller et al. [34]. After that the implementations have fol-

lowed mostly similar concepts and development has focused on the micromechanics of the test – i.e. the analysis. Notable contributions to the analysis have been made by Scheer and Nairn [35], and this concept has been expanded upon by Zhandarov and Mäder [36, 37, 38]. For the purposes of these analytical methods there is very little distinction between the microbond and pull-out tests, and Zhandarov et al. famously discuss the methods interchangeably in the analysis.

What the different research groups studying the topic mostly agree on is the fact that the apparent interfacial shear strength (IFSS) [31] is a poor measure for the interphase and more advanced analysis is always required. The current state-of-the-art utilises either FEA or analytical models to better understand the test system, and the results in terms of actual material behaviour. The apparent IFSS (often also denoted as τ_{app}) fails to account for important factors such as thermal residual stresses in the overall load during the test. An example of a more thorough analysis is the stress-based analysis as presented by Zhandarov [39].

The analysis starts with determination of the Nayfeh shear lag parameter β_N, presented as

$$\beta_N^2 = \frac{2}{r_f^2 E_f E_m} \left[\frac{E_f V_f + E_m V_m}{\frac{V_m}{4G_f} + \frac{1}{2G_m} \left(\frac{1}{V_m} ln(1/V_f) - 1 - \frac{V_f}{2} \right)} \right] \tag{3.1}$$

where E_f, E_m, G_f and G_m are the tensile and shear modulus of the fibre and the matrix, respectively. V_f and V_m are the volume fractions of the two components and r_f is the fibre radius. Estimation of the fibre volume fraction requires an estimation of the droplet shape, for which implementations range from simple cylindrical approximations [35] to very accurate surface property based models such as Carroll's method [40] and its further developments [41, 42].

The aforementioned formulation for the shear lag parameter can result in nonsensical β_N^2 values when the fibre volume fraction is higher than a certain material-dependent critical value [39]. The Cox shear lag parameter β_C is more robust and generally well-behaved for higher fibre volume fractions [35, 39, 43] but significantly less accurate for drop-on-fibre cases.

$$\beta_C^2 = \frac{2G_m}{E_f ln\left(\frac{1}{V_f}\right)} \tag{3.2}$$

The shear lag parameter can be used to estimate the thermal residual stresses (τ_T) at the interphase with

$$\tau_T = \frac{\beta r_f E_f}{2}(\alpha_f - \alpha_m)\Delta T \tag{3.3}$$

where α_f and α_m are the fibre and resin thermal expansion coefficients and ΔT is the temperature difference from stress-free temperature and testing conditions.

In the model, the debonding events are separated into two cases: catastrophic crack propagation through the whole embedded length and stable crack propagation. The main difference is that sliding friction is ignored in the catastrophic debonding case. The case for each droplet is determined based on the shear lag parameter β (Nayfeh or Cox) and embedded length (l_{emb}) according to the conditions given in Table 3.3. The u parameter is defined as,

$$u = \frac{\sqrt{\tau_T^2 + 4\tau_{\text{fric}}(\tau_d - \tau_{\text{fric}})} - \tau_T}{2\tau_{\text{fric}}} \tag{3.4}$$

where τ_{fric} and τ_d are the interfacial friction and interfacial shear strengths, respectively. As seen from Equation 3.4, the u parameter relates to the relative contributions of the stresses and is therefore used to determine the stability of the damage propagation according to Table 3.3.

Table 3.3 Distribution of the result to the two primary analysis cases.

Case	Explanation of the case [39]
1: $\beta l_{emb} < \ln(u + \sqrt{(u^2 + 1)})$	Catastrophic debonding
2: $\beta l_{emb} \geq \ln(u + \sqrt{(u^2 + 1)})$	Stable propagation

Depending on the case, the model can be used to connect the maximum load to the interfacial stress parameters (τ_d, τ_T and τ_{fric}) and embedded length (l_{emb}) as

follows [39]:

$$
F_{max}(l_{emb}) =
\begin{cases}
\dfrac{2\pi r_f}{\beta}\Big[\tau_d\tanh(\beta l_{emb}) \\[1em]
\quad - \tau_T\tanh(\beta l_{emb})\tanh(\dfrac{\beta l_{emb}}{2})\Big], & \text{for case 1} \\[1em]
\dfrac{2\pi r_f}{\beta}\Big[\tau_d\dfrac{u}{\sqrt{(u^2+1)}} - \tau_T\left(1-\dfrac{1}{\sqrt{(u^2+1)}}\right) \\[1em]
\quad + \tau_{\text{fric}}\Big[\beta l_{emb} - \ln(u+\sqrt{(u^2+1)})\Big]\Big], & \text{for case 2}
\end{cases}
\tag{3.5}
$$

The β can be either Nayfeh (β_N) or Cox (β_C) shear lag parameter, but as previously mentioned, β_N should be favoured for all $\beta_N^2 > 0$. The effects of the the various parameters – and the general behaviour of the model – are presented in Figure 3.3.
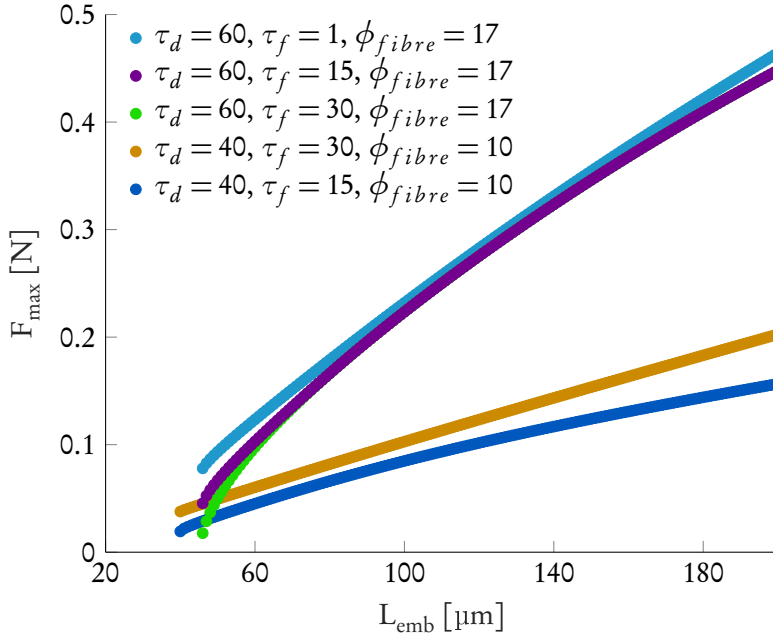
Figure 3.3 F_{max} based on Equation 3.5 in the embedded lengths up to 200 μm. Embedded lengths lower than plotted in the Figure result in negative β^2 even with the β_N indicating the critical fibre volume fraction. For input values not presented in the Figure, refer to Publication I.

This formulation is among the best analytical models currently available for analysing microbond or fibre pull-out results. The model shows excellent agreement with both testing methods and correctly predicts their respective changes in behaviour with

changing droplet size. Zhandarov et al. have worked almost exclusively on fibre pull-out, but the agreement of the model with high-quality microbond results was verified as a part of this dissertation using a large experimental dataset of microbond results (see Publication I).

The multivariate fitting required for the use of Zhandarov's model (without readily available τ_d values) is quite arduous mathematically, and an easier approach would be preferable for efficient experimental work. The apparent IFSS calculation presented by Miller [31] is not sufficient for any type of in-depth analysis, as it is too dependent on sample geometry and droplet preparation related effects. A much more effective, but still computationally trivial, approach is to use the slope of the force - area curve as a more appropriate – if still approximate – measure of the interfacial strength. This slope-based analysis is denoted as the apparent interfacial shear stress (IFSS) in this dissertation. The arguments for the validity of this analysis approach are strongly tied to the topic of this work and will be discussed thoroughly in Section 5.1.

Finite element analysis (FEA) is another commonly employed tool for solving the interfacial parameters based on experimental setups. While the topic is mostly outside of this work, FEA results will be presented when available based on the work of colleagues as either an active part of this work or parallel to it.

In this work, an effort is made to also utilise the microbond loading scheme for fatigue testing. As actually gripping the droplet would significantly alter the loading state, this cyclic loading is done exclusively with R ratio = 0, i.e. only positive loading amplitudes are utilised. As very few examples of microcomposite fatigue testing exist [44, 45, 46], no in-depth analytical models – such as those presented above for the quasi-static case – exist as of yet. The analysis of the experimental work focuses on qualitative interpretation of the sample behaviour based on apparent stress versus fatigue life (number of cycles until failure, N) and well-established statistical methods for fatigue analysis, such as Weibull distributions.

As is also evident from Zhandarov's formulation above, friction can and often will contribute significantly to the force measured during a microbond type test. Frictions of two different origins are considered relevant in this study: Friction at regions not fully debonded – which will be denoted as adhesional friction – and sliding friction at debonded regions. Out of these two, the first tends to fall slightly outside the general basic concepts of friction and is very complex to observe or mea-

sure, but it is also very relevant to the overall discussion. For the sliding friction, a definitive value of the friction coefficient (μ) can generally be determined from the values of the sliding force in the experiment (i.e. when the droplet slides on the fibre after debonding, denoted F_{fric}). This method for determination of friction is cited as the 'alternative' approach by Zhandarov et al. [37, 38]. In the adopted methodology for sample preparation, a very thin residual film is formed at the droplet exit point during droplet preparation, which increases the experimental F_{fric}. This in turn leads to overestimating the values of μ and poses a challenge in estimating it. The role of the thin resin film in the results is explored in a future publication by Dsouza et al. [47]. The primary goal of determining friction remains the estimation of τ_d from F_{max} in the stress-based approach or critical energy release rate G_{ic} in the energy-based approach [38]. In this work the analytical model is used as a means of validation for the slope-based analysis of τ_d. As such, the various approaches for experimental frictional stress determination and the energy-based approach, while important to the overall discussion on microcomposite testing, are not discussed in detail. Methods for acquiring the necessary outputs from the employed experimental setup are discussed in Section 5.1.

4 EXPERIMENTAL

4.1 Materials

The following sections provide a collected overview of the materials tested and used in the course of this work. The main focus is – as previously mentioned – in glass fibre reinforcements and epoxy resins. In addition to these, various chemicals are used in the surface treatments, or sizings, of the fibres, and these have also been collected here.

4.1.1 Polymer resins

This work focuses mainly on two types of epoxy resins. The first is Araldite LY 5052 hardened with Aradur 5052 amine hardener by Huntsman (Huntsman Advanced Materials Inc., USA). This cold curing resin system has excellent mechanical properties and is frequently used e.g. in the aerospace sector and other similar high-performance applications. It represents the current high-end of epoxy properties and is also very reliable as a material for microdroplet preparation – i.e. cured droplets exhibit consistent properties – and is therefore used as the default resin for the microcomposite methodology-focused studies. This resin system will be denoted as Araldite for the remainder of this dissertation.

The second resin system in use is the reference material for most of the computational work. Diglycidyl ether of Bisphenol-A (DGEBA) is a common base material for many epoxy resins, and a pure grade is available with the trade name EPON 828. The epoxy is combined with a small molecular weight polyether amine (poly(oxypropylene diamine), PEA) available with the trade name Jeffamine D-230 from Huntsman (Huntsman Corporation, USA). Macroscopic samples prepared with varying curing cycles from this resin are denoted as Bulk samples, with the rest of the sample

name signifying the used curing cycle as described in Publication IV. The simplic-
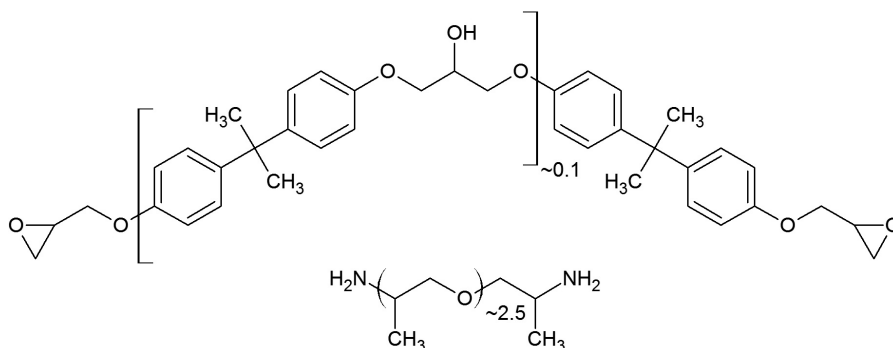
Figure 4.1   Structures of the DGEBA and polyether amine molecules in resin 828. [Publication IV]

ity of the mixture, i.e. the only one type of molecule or prepolymer structure per component, each with a specific range of molecular weight, is another reason for its selection. This makes the resin system easy to model in atomistic simulations. The resin system also represents the epoxy systems with frequent problems in microdroplet preparation unless specific steps are taken to mitigate them. This resin system will be denoted as 828 for the remainder of this dissertation. The stoichiometric mixing ratios of the two resins in parts by weight are presented in Table 4.1.

Table 4.1   Mixing ratios of resin and hardener (parts by weight) for the two epoxy systems.

Resin	Epoxide	Hardener	Ref
Araldite	100	38	[48]
828	100	32	[49, 50]

4.1.2   Fibre reinforcements

All glass fibre grades used in this study are various chemical-resistant E-glass fibres (ECR). ECR glass is a boron-free formulation of E-glass which allows for increased chemical resistance in corrosive environments. The mechanism of this resistance is identified as the exclusion of boron from the glass structure, disallowing the depletion of various non-silica components of the glass from penetrating further than a specific equilibrium depth, i.e. a creation of a protective "gel" layer on the fibre

surface [51, 52, 53]. This does, however, result in the formation of a slightly porous layer on the surface of the glass, comprising only silica. The reader is advised to keep this concept in mind when considering the interphase structure and any possible discussion on ageing durability of composites. It is all too common in the composites industry to assume glass fibres as inert components when, in fact, they are far from it.

The specific grades used in this work are Jushi E6-CR17 (China Jushi Co., Ltd., China) and HiPer-tex® W2020 (3B-fibreglass, Belgium), both originally sized with an "epoxy compatible" sizing. Nothing else is known of the specific sizing formulation originally on the fibre surface – except the storage time of the fibre. The nominal diameter of both fibres was reported by the manufacturer as 17 µm.

The E6-CR17 glass fibres are from a batch well past its recommended storage life, and the fibres are used mainly for parts of the study in which a simplified model sizing is applied on cleaned fibres to create a sizing with known chemical components. These components and the preparation of the sizing are described in more detail in the following Section (4.1.3). The HiPer-tex® W2020 fibres were used as an industry reference sample and used exclusively from fresh samples with ample shelf-life remaining. Similarly to Araldite as the resin in this work, the fibres were thus in use for cases where the methodology and the device were the focus, or as a point of comparison.

4.1.3   Interphase components - sizing

As detailed previously, the primary components of a fibre sizing, at least insofar as they relate to increasing the interfacial performance of the composite, are the CA and the film former. The model epoxy sizing used in this work comprised an aminosilane (APTES) and an epoxy film former, commercially available from Michelman with the trade name Hydrosize® EP871EU. This film former is a 30 w-% solid content aqueous dispersion of DGEBA epoxy. The total concentration of these components in the sizing solution was 1 w-% to prevent the deposition of excess sizing on the fibre surface. The CA/film former ratio was approximately 10%/90% in weight. These concentrations were selected based on a parallel study on resizing of recycled glass and carbon fibres [17].

Before any sizing of fibres, the residues of the original sizing were removed by

"washing" the fibres in Piranha solution. The solution is a mixture of two-thirds (2/3) concentrated sulphuric acid and one third (1/3) of 33% (volumetric) aqueous solution of hydrogen peroxide. Mixing fractions were determined by weight. Piranha solution is commonly used for cleaning glass surfaces from organic residues, as the mixture aggressively and almost instantly dissolves any organic compounds it comes into contact with (hence the name). Thus a very short immersion in the solution – too short to noticeably damage the fibres themselves – was enough to remove the organic sizing layer.

To prepare the sizing solution, the CA, roughly half of the water and acetic acid (reagent grade ⩾ 99% purity) equal to half of the weight of the CA – to reduce the solution pH – were mixed for one hour to hydrolyse the siloxane bridges connecting the small side groups of the organosilane CA. The film former and remaining water were then added and the resulting solution was mixed for another hour. Finally, the pH of the solution was checked to be within the 6-7 range and, if necessary, adjusted with small additions of the acetic acid or 1 M KOH solution. The temperature of the solution was controlled at 30 °C, with steady constant mixing throughout this process to ensure a completely homogeneous mixture.

The sizing of the fibres themselves was carried out as a batch process. The fibre tows were separated to ensure efficient wetting during the immersion, and a manageable bundle of fibres was dipped in the sizing solution for roughly three seconds. Immediately after this, the fibres were dipped in deionised water to remove the excess sizing solution kept in the fibre bundle by capillary forces. The fibres were then allowed to dry, suspended, in a well-ventilated space at room temperature for 24 hours.

4.2 The microbond test

The basic methodology and the scientific background of the microbond test are already described in Section 3.2. This section will therefore focus more on the specific application of this methodology in the form of the FIBROdrop and FIBRObond devices of Fibrobotics Oy, which were used – and partly developed further – during this work.

4.2.1 Devices

The basic functionalities of the device are specified in Publication I, the purpose of which was the identification and minimisation of common error sources in microbond testing. The information on specific components of the experimental setup and their characterisation are presented in detail in Publication I. It is, however, important to raise some key issues for discussion. The sample preparation with the FIBROdrop device follows the European Patent EP3635361, using a fibre pulled through a well of resin to coat the fibre with the resin, which leads to a formation of droplets due to Plateau-Rayleigh instability. The size of the deposited droplets is controlled via altering the parameters of the fibre movement through the resin well. This method enables deposition of a wide range of controlled droplet sizes and, as the fibres are fully wetted by the resin, the deposited droplets are very symmetric and follow the expected behaviour of drop-on-fibre systems [54].

Microbond – and microcomposite testing in general – is done at a very challenging length scale compared to widespread macroscale mechanical tests. The first challenge is fairly obvious, but surprisingly often overlooked: the device needs to be designed for accurate operation at that length scale. A part of the problem of unreliability of microbond testing stems from the widespread utilisation of universal testing systems as the basis of the experimental setups. Before this changes, the methodology will continue to be held back and sometimes disregarded due to the bad reputation caused by unreliable, poorly correlating experimental data.

Still, not all of the scatter in the results is due to experimental errors. In Publication I, a well-designed experiment enables separating the many sources of experimental variation to those related to the experimentation and those from the sample itself. The former are shown to be dependent either on the accuracy of the device itself – e.g. suitable load cells and actuator operation accurate at the nanometer scale – or accuracy in operating the device – e.g. consistency in determination of the embedded length. The sample-related variation is, in turn, always observed as the properties of different individual fibres, and even droplets can vary. By measuring a statistically relevant sampling of droplets from each individual fibre, the fibre surface related variation can be quantified. Droplet-dependent scatter in results arises from differences in curing and the resulting difference in resin and, possibly, interphase properties. The optimal droplet size range and preparation parameters for

repeatable results need to be identified for each fibre - resin combination. The appropriate droplet size range is – based on our current experience – 60–200 µm and 50–150 µm in embedded length for glass and carbon fibres, respectively. The difference between the two fibre types is a result of their generally different diameters and the aforementioned ranges for droplet size, assuming approximate diameters of 15–22 µm for glass fibres and 7–15 µm for carbon fibres. The lower limit is determined by the critical fibre volume fraction and the fact that excessively small droplets are cohesively sheared by the blades. The upper limit is dependent mainly on fibre tensile strength. A weaker interface will enable measurement of larger droplets, but very large droplets will deviate from the approximately linear behaviour discussed in Section 3.2.

The micro-fatigue test, presented in Publication II, utilises the same microbond setup with primarily software-related modifications for controlled oscillatory motion of the microvice blades. The only hardware modification from the experimental setup described in Publication I was a replacement of the DC motor with a magnetic drive as the primary linear actuator. This change enabled the accurate high-frequency oscillating displacement necessary for the micro-fatigue test. The greatest challenge in the design of a successful microcomposite fatigue test was maintaining a constant load and displacement amplitude during the test. Unlike dynamic mechanical analysis (DMA), which also employs cyclic loading, fatigue testing is intended to characterise sample failure due to repeated leading cycles. The small sample scale exacerbates the issue as e.g. the meniscus region of a microdroplet always deforms during the first couple loading cycles. Therefore, the test was designed to compensate for any plastic deformation with sub-micron adjustments to the displacement cycle starting position – controlled by a monitoring loop in the software – to maintain a constant peak force level in the test. For detailed discussion on the experimental parameters of the micro-fatigue test, refer to Publication II.

4.2.2 Analytical methods

The most prominent analytical model utilised in this study is the stress-based analysis for microbond results, already detailed in Section 3.2. The analysis is mainly used in Publication I as a part of the validation of the experimental procedure and the simplified slope-based analysis. To achieve this, the fitting is done using the measured

maximum force (F_{max}) and embedded length (l_{emb}) values, while also simplifying the fitting by using the slope-based IFSS as τ_d. The whole analysis and fitting was done in MATLAB with custom scripts written as a part of this work.

The Weibull analysis of the micro-fatigue test results was done using the two-parameter Weibull distribution, fitted by using the maximum likelihood method. The data was split into stress-level groups to incorporate the role of stress into the analysis. A division to three groups was selected as most fitting based on the number of available datapoints, with the groups formed from: 1) mean stress group from $mean \pm stdev/2$ of the stress values in the dataset, 2) low outliers of 1) and 3) high outliers of 1). The complete micro-fatigue analysis was also implemented in MAT-LAB through custom scripts created during the course of this work.

4.2.3 Numerical methods

Publication II features finite element analysis as the primary method of validation for the experimental approach. The main concerns comprised the role of friction, the strain rate dependency of the results and the heating of the sample from the high strain rate cyclic deformations during the micro-fatigue test. This section will not provide a comprehensive overview of the simulation steps, but rather presents the primary concepts needed to understand the adopted approach. More details are available in Publication II and the other literature referenced here.

A 3D finite element model (FE) of the test was developed using Abaqus Standard-/Explicit 2020 (Dassault Systèmes, France). The droplet ($\phi_{droplet} = 0.036$ mm and $A_{emb} = 0.102$ mm) was chosen from the test of a sized filament ($\phi_{fibre} = 0.0178$ mm) located 6 mm from the fixed position of the fibre. The mesh of the experimental setup used in the FEA is presented in Figure 4.2.

Force and fibre strain data from the experiments were used to validate the interfacial constants such as critical stress (τ_c) and critical energy of debonding (G_c) using force-strain derivative data [55]. It was assumed that the mode I component of critical energy of debonding (G_c) and critical stress at the interface (τ_c) behaved in the same way as the mode II and mode III components. In all cases, the epoxy droplet was treated as elastic-plastic with isotropic hardening conditions. Details of the boundary conditions and numerical values of the mechanical constants can be found in literature featuring the simulation approach [55, 56]. The shrinkage of the
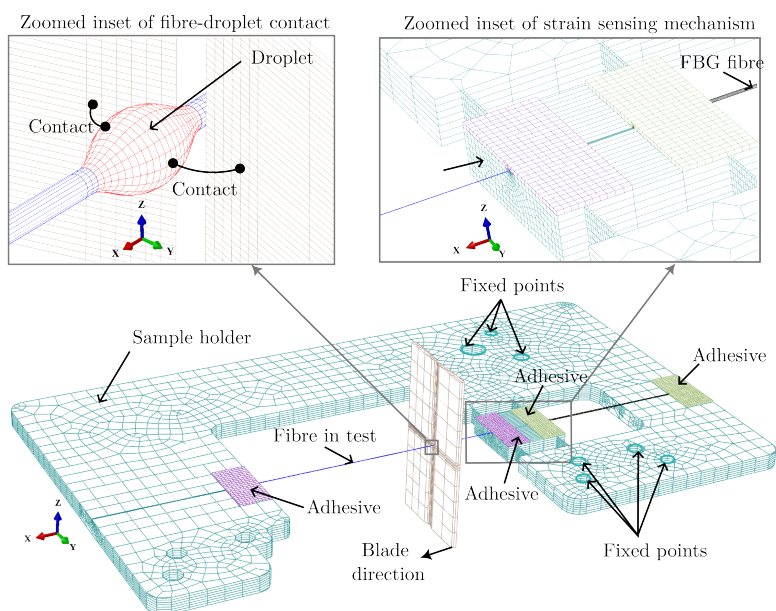
Figure 4.2 Full setup of the FE model along with the zoomed insets. The filament (fibre in test), Fiber Bragg grating (FBG) sensor, sample holder and adhesive were modelled as linear elastic materials and the loading blades as rigid bodies. [Publication II]

droplet due to cooling from the curing temperature of 80 °C to room temperature was simulated by including a temperature difference of -56 °C as a loading step in the analysis.

4.3 Other experimental methods

4.3.1 Thermal analysis

Publication IV incorporates thermal analysis to explore the curing behaviour of the EPON 828 - Jeffamine D-230 resin system. The relatively simple chemistry of this epoxy system makes it well suited for computational chemistry methods, which are described in more detail in the Section 4.4.

Thermogravimetric analysis (TGA) utilised a Netzsch TG 209F3 *Tarsus* coupled to a Bruker Tensor 27 FTIR for chemical analysis of the gaseous residues exiting the TGA oven (TGA-FTIR). TGA measurements were conducted for an unreacted resin mixture of the EPON 828 - Jeffamine D-230 system and the components sep-

arately. The coupled TGA-FTIR analysis is used to identify whether the diamine curing agent, DGEBA or a combination of the two is primarily evaporated from the resin mixture during the cure cycle. A dynamic heating step was used in the test from -20 to 350 °C with a heating rate of 10 K/min in a protective nitrogen gas atmosphere.

Differential scanning calorimetry (DSC) was, in turn, used to analyse the degree of cure of the bulk resin samples featured in Publication IV. Dynamic heating steps from -20 °C to 300 °C were used to determine the resulting T_g for the initial curing cycle and to determine the residual curing enthalpy. The samples were then cooled to -20 °C, followed by another dynamic heating step from -20 to 300 °C to ensure no residual reactive potential and that the glass transition matched the fully cured state. Total curing enthalpy was determined by using the same heating steps for an uncured resin mixture. Comparing the residual enthalpy to the total enthalpy of the uncured systems enables the determination of degree of cure relative to the practical maximum, which is rarely equal to the theoretical maximum determined by the stoichiometric amount of functional groups due to very restricted molecular mobility at the later stages of curing [57].

4.3.2 Nanoindentation

Nanointendation tests were carried out with an Alemnis in-situ nanoindenter (Alemnis AG, Switzerland) integrated inside a Scanning Electron Microscope (SEM, Zeiss LEO 1450, Germany). A cube corner pyramidal tip was used for all the indentations. The indents comprised loading, peak hold and unloading segments. Except for the peak hold segment, which was load-controlled, all other segments were in displacement-controlled mode. Loading and unloading segments were performed in constant indentation strain rate of 0.6 s^{-1}. Indentation depth was set to 1.2 µm after contact load of 0.5 mN, which rests in total indentation depths of 1.4 µm. After attaining peak displacement during loading segment, the load was held constant for 3 s to allow the material to creep at peak hold segment. This was followed by constant strain rate unloading from the sample surface. At least 10 indents were performed on each Bulk sample and 3 indents were performed on each microdroplet. The whole loading/unloading cycles were done in less than 30 s.

The indentation sites were selected from the thickest parts of the microdroplet to

avoid any elastic influence from the fibre and to have the indenter tip oriented as close to the normal of the droplet surface as possible. The load-displacement data from each indentation was analysed with the Oliver-Pharr method [58] to estimate resin modulus and hardness, and a minimum of three indents was done to each droplet to ensure consistency. The imaging during indentation used a LaB6 filament with 3.0 kV accelerating voltage. The accelerating voltage was kept low to avoid charging or other interaction with the sample.

4.4 Computational methods

The computational chemistry in this work is all performed with the Schrödinger Materials Science Suite software. The density functional theory (DFT) part of the work was focused on studying the crosslinking reactions of epoxy amine systems and the role of non-covalent bonding as both a catalyst and hindrance to the reactivity. The insights into non-covalent bonding of epoxy structures are also applicable to understanding the behaviour of the resin components at larger length scales – helping to tie in the study to the rest of the work. The simulation work was expanded through simulations of crosslinked epoxy networks mainly by utilising various structure builder workflows and molecular dynamics (MD) simulation workflows available in the Materials Science Suite. As these simulations directly contribute to, with most of them also utilising, MD stages, the whole epoxy network simulation work is described in Section 4.4.2, titled Molecular Dynamics.

4.4.1 Density functional theory

The DFT computations were performed using the Schrödinger Materials Science Suite (Schrödinger Inc., New York, USA) software package (version 2020-4) – most prominently the Jaguar (version 11.0) DFT program [59]. Long-range corrected hybrid non-local B3LYP-D3 theory level was used for all DFT computations. The functional has been shown to give a good combination of accuracy and computational efficiency with many types of chemical structures and non-covalent bonding cases [60, 61]. However, it was deemed necessary to explore other options to help validate the selection. To accomplish this, M06-2X and ωB97X-D functionals along with B3LYP-D3 with Becke-Johnson damping [62] were tested in single point en-

ergy (SPE) computations for some of the larger conformer groups to ensure that at least the relative energy levels of different conformers were similar.

Changing the functional resulted in, at most, around 20% change in the relative energy levels between conformers, with no change in the relative trends between them. The biggest differences were in computation times. With the M06-2X funtional, the average computation time for a set of moderately complex structures (A4,E1 in Publication III) was approximately 89,700 CPU seconds per structure vs. approximately 47,500 CPU seconds with B3LYP-D3. The B3LYP-D3(BJ) slightly out-performed B3LYP-D3 with an average computation time of approximately 40,500 CPU seconds. With the ωB97x-D functional these computations failed to converge. Successful computations with the ωB97x-D functional include SPE for the hydroxyl-catalysed A4,E4 conformers, for which the computation times were approximately 230,000 CPU seconds per structure vs. approximately 47,000 with B3LYP-D3.

The role of the structural cut-offs was explored using reaction workflows in the Schrödinger Materials Science Suite. The reaction workflow – currently renamed more descriptively as the Reaction Energetics Enumeration workflow – uses a predetermined prototype reaction to explore the changes by swapping fragments outside the reactive core. The transition state search using the quadratic synchronous transit (QST) search method was used to first define the prototype reactions. Ethylamine was selected as the representative simplified amine structure – instead of the even simpler methylamine – to reduce the contribution of the α-effect for the reactive core. Ethylamine was also used as the catalysing amine for all relevant simulations. Similarly, isopropyl alcohol was used as the source of the catalysing hydroxyl group.

In order to find the most probable reactive paths, a conformational search – using the MacroModel program with the OPLS3e force field [63] for Monte Carlo Multiple Minimum (MCMM) searches – was added to each transition state search and reaction workflow. The MCMM conformational search generates trial conformers based on random changes to torsion angles to sample the conformational space for local minima [64]. For the transition state searches, only the lowest energy conformers were available as outputs. In the reaction workflow, the ten lowest energy conformers were requested from separate conformational search runs of the same starting structure. For more details on the specific computation steps, see Publication III.

The basis set was varied for different computational tasks. The 6-31G** basis set was used for the transition state searches and initial structural optimisations. The reaction workflow utilised the LACVP** basis set, which – as the workflow default – resulted in significantly less convergence issues for the structural optimisation stage of the workflow than the 6-31G** basis set. The cc-pVTZ(-F) triple zeta basis set was used for all final SPE computations.

4.4.2   Molecular dynamics

The molecular network of the 828 epoxy was modelled in the Maestro graphical interface of the Schrödinger Materials Suite. The molecular dynamics (MD) calculations used established workflows with Desmond/GPU, capable of utilising the high level of parallelisation offered by modern graphical processing units [65]. The current version of the OPLS force field, OPLS4 [63, 66, 67, 68], was used in all simulations.

To match the epoxy and amine hydrogen equivalent weights provided by the material manufacturer's technical data sheets, a mixture of two structures for both the epoxy and amine component was selected. Five parallel simulation boxes were created through random snapped-to-grid placement of these molecules near the centre of the simulation box (steric packing) with a van der Waals radii scaling factor of 0.5 to avoid overlaps. After placing the atoms, the simulation box is finalised with 3D orthorhombic periodic boundary conditions. The input molecules and the amounts input into the simulation boxes are presented in Table 4.2.

The simulation boxes were relaxed through a relaxation workflow comprising a total of eight simulation stages ending with a final 10 ns NPT stage at 300 K and 1.01325 bar with 2 fs timestep – from which the relaxation is assessed by monitoring the density convergence of the simulation box. The first 7 stages of the relaxation protocol were: Energy minimisation for 0.1 ns with an NVT ensemble at 10 K and 1 fs timestep followed by 7 consecutive MD simulations, 24 ps NVT ensemble at 300 K with 1 fs timestep, 0.2 ns NVT ensemble at 700 K with 1 fs timestep, <0.1 ns NPT ensemble at 300 K and 1.01325 bar with 1 fs timestep, 0.2 ns NPT ensemble at 300 K and 1.01325 bar with 2 fs timestep, 10 ns NPT ensemble at 300 K and 1013.25 bar with 2 fs timestep, 10 ns NPT ensemble at 300 K and 1.01325 bar with 2 fs timestep The sizes of the initial and relaxed simulation boxes are presented in

Table 4.2 Inputs for the Disordered system builder for the epoxy resin simulations, the value n signifies repeating unit count for each structure (see Figure 4.1). The equivalent weight (Eq. weight) column refers to the epoxy equivalent weight and amine hydrogen equivalent weights for the mixtures of the DGEBA and PEA structures, respectively. The data sheet value used for reference is given in parentheses ([49, 50]). [Publication IV]

Component	MW [g/mol]	input molecules	Eq. weight [g/mol]
DGEBA, n=0	340.4	112	187.8 (185-192)
DGEBA, n=1	624.8	16	
PEA, n=2	190.3	14	59.1 (60)
PEA, n=3	248.4	50	

Table 4.3 Initial and relaxed simulation boxes before the crosslinking simulations. The initial sizes are from the Disordered system builder after only steric packing, the relaxed dimensions are after the eight-stage relaxation protocol. The densities for the relaxed simulation boxes are averages and standard deviations of the model system density during the last 20% of the final 10 ns MD simulation trajectory.

Box [Å]	x/y/z initial [Å]	x/y/z relaxed [g/cm^3]	density
1	69.7/74.6/76.3	43.1/46.2/47.3	1.096 ± 0.004
2	73.5/76.7/74.8	44.7/46.6/45.5	1.094 ± 0.004
3	77.4/72.1/72.5	47.7/44.4/44.6	1.094 ± 0.004
4	73.2/72.8/72.9	45.6/45.4/45.4	1.097 ± 0.004
5	70.7/71.8/69.5	45.5/46.3/44.8	1.097 ± 0.004

Table 4.3 along with the equilibrated densities of the relaxed simulation boxes.

To create crosslinked networks, the simulation boxes were input to a Crosslink Polymers workflow, which forms crosslinks based on the following input criteria: maximum number of crosslinks per iteration, reaction threshold distance and the temperature-dependent relative probabilities of the defined reactions. The reaction thresholds were cut-off distances in Ångstrom outside of which a complementary reactive site does not qualify for the reaction. The reaction probabilities were computed by the software based on primary and secondary amine reaction activation energies with the assumption that there are no other energy states in the system

than the reactions defined in the simulation input.

After forming a set of crosslinks based on the aforementioned criteria, the simulation box is equilibrated with MD for 50 ns, an NPT ensemble at 1.01325 bar. The thermostat target temperature is dependent on the simulation run and iteration. All temperature ramps were simulated starting from 300 K with the same "heating rate," up to a maximum temperature and back to 300 K, to create simulation boxes with different degrees of conversion by varying the maximum temperature (300 K, 400 K, 500 K, 600 K or 700 K). If the temperature ramp ends before the simulation end-criteria are met, the iterations continue at 300 K. The primary purpose of the workflow was the creation of reasonably representative crosslinked structures for inputs to the stress-strain calculations. It also provided some qualitative insight into the molecular mobility dependent kinetics at later stages of the crosslinking process.

Mechanical properties are estimated from cyclic stress-strain simulations. This simulation workflow incrementally deforms the simulation box and uses Desmond/GPU to examine the system response to this strain from 1.5 ns NVT ensemble simulations. Stress is calculated from the last 20% of the trajectory. Strain rate is determined from the strain step size (-0.0015) and simulation time resulting in a strain rate of 10^6 s^{-1} with total strain kept under 20%. For detailed description of the stress-strain simulation, refer to Publication IV.

5 RESULTS

5.1 Interfacial shear strength as a measure of the interphase

In Publication I, the IFSS of the HiPer-tex W2020 glass fibre – Araldite microcomposites was determined by measuring the load required to debond a total of 1,527 microdroplets with varying embedded lengths. This sampling represents the glass fibre roving from a length of approximately 1.3 m.

Droplets deposited into close proximity of each other are noted to exhibit very similar interfacial properties. Together with tightly controlled experimental parameters, measuring such sets of droplets enables the measurement of sets of data with very low experimental scatter. The complete dataset along with the corresponding analytical model fits are presented in Figure 5.1

The experimental scatter of results in Figure 5.1 a) appears significant, but as stated earlier, the combination of sample preparation and robust experimentation can be used to distinguish between the scatter from the experiment and the variation of results related to the materials. The scatter seen in the results presented in Figure 5.1 a) comprises almost fully the latter. Examples of individually plotted single-fibre datasets highlighting this are presented in Publication I.

The analytical model fitting presented in Figure 5.1 b) is shown to match the experimental data well. The fitting could be improved further by better experimental determination of the frictional component of the total stress, τ_f. This can be achieved in the system by also measuring the fibre strain to find the initial debond force level as suggested by Dsouza et al. [55]. Including the fibre strain enables accurate detection of the debonding force (F_d) similarly to the 'kink' often detected in the pull-out method [36, 37, 38]. While unnecessary for the stress-based analysis employed here, determination of F_d and consequently F_{fric} is an important component of a more de-
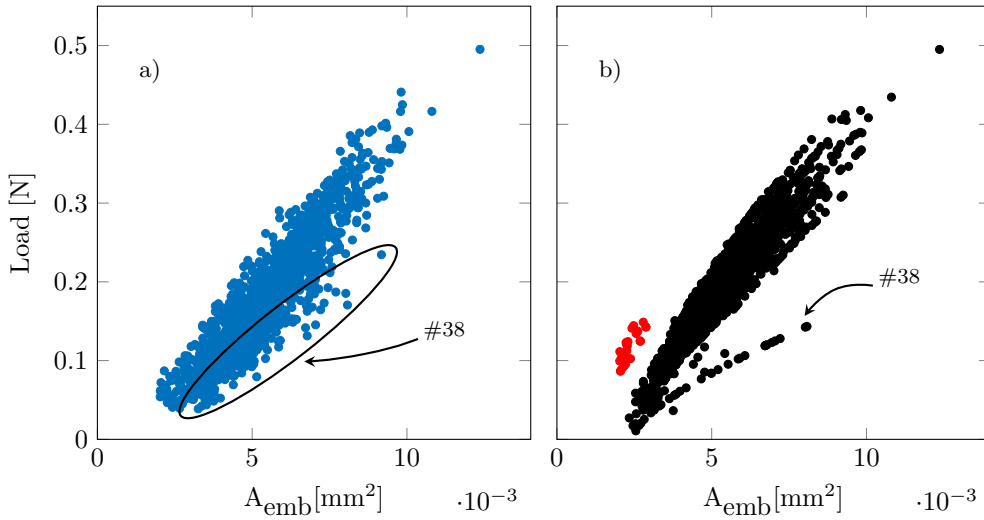
Figure 5.1 Load vs. embedded area for all measured droplets, a) Measured data, b) Data based on the analytical model presented in Section 3.2. Data points analysed with the Cox shear lag parameter (due to complex ($\beta_N^2 < 0$) Nayfeh parameters) are indicated in red. Filament # 38 deviated significantly from the rest of the data and is highlighted in the plot. [Modified from Publication I]

tailed analysis approach and absolutely necessary for the energy-based approach for experimental analysis of the critical energy release rate, G_{ic}. The fitting was done by solving for maximum load from equation 3.5 using the slope of the linear fit of individual datasets as τ_d. For a more detailed description, refer to Publication I. The fitting shows excellent agreement due to the large number of tested samples and the low scatter of the individual datasets, as shown in Figure 5.1.

These results highlight that reliable and repeatable interfacial parameters can be determined based on microbond results. Strict requirements for device specifications and material behaviour are, however, present and universality can only be achieved with further understanding of the complex interplay of resin properties (which have been shown to differ from bulk), curing behaviour and the fibre surface treatments (e.g. sizing). The fibre - resin combination utilised in the study is a particularly well-behaving system and was selected for that specific reason for the method valida-tion study. Naturally, the ultimate goal is universal applicability of the experimen-tal methodology to all fibre-matrix combinations, which is hard to reach and even harder to verify.

Table 5.1 Common error sources in microbond testing. Replicated from Publication I.

Error source	Possible negative outcomes	Ref.
Load measurement	Over-/underestimation of the measured load	[34]
Device optics	Inaccurate embedded length and/or fibre diameter	[34, 69]
Microvise control	Variation of droplet loading state, high experimental scatter in final results	[70, 71, 73]
Embedded area range	Changes in test behaviour, fibre breakage	[35, 69, 74]
Fibre surface	Variation of the results, always present	[31, 34]
Resin curing	Inconsistent results, increased scatter in results, resin failure	[28, 75]

5.1.1 Sources of error

The sources of error in microbond testing have been identified in several scientific works. The most comprehensive is the review article by Sockalingam [69]. In the device, critical aspects to minimise the experimental scatter include high sampling rate of load measurement and accurate determination of fibre and droplet dimensions in addition to microvise blade control [34]. The microvise blade placement is one of the most important of these error sources, because it is considered a major contributor to the high variation of results [70, 71, 72, 73]. An overview of the key error sources as presented in Publication I is listed in Table 5.1. Some of these error sources represent the frequent shortcomings of microbond experimental setups that result in the aforementioned "bad data." Others are unavoidable, however, and need to be understood in order to mitigate their role during the experiments or analysis of the results.

5.1.2 Unresolved issues - validity and uncertainty

A few notable questions remain outside those explored in this study. The employed droplet preparation method resolves many common problems of microcomposite preparation, such as low throughput and unsymmetric droplets, and minimises the

required handling of the fibres – i.e. the region of the fibre surface being measured has been changed as little as possible by the sample preparation. However, wetting the whole filament from the measured region can lead to new issues not exhibited by other methods.

First is the formation of a very thin polymer film on the surface of the whole wetted region. Based on the experimental work thus far, the contribution of this film to the maximum force based microbond measurement result is negligible. Considering the problems in curing the resin in the droplets, this result is unsurprising. The correct placement of the microtome blades on the fibre surface separates a significant portion of this film, which also has very poor mechanical properties, and the meniscus separates from the film without practically any force required. This film, however, presents a problem for the determination of the frictional component τ_f as it cannot be approximated from the sliding friction of the debonded droplet. This issue is exacerbated if poorly selected sample preparation parameters cause the formation of droplets to be too close to those intended for measurement.

Another related aspect of uncertainty is the repeated loading of the filament. While this is unavoidable – as repeated measurements from the same filament are needed to quantify the variation between filaments of a fibre type – it is unclear whether the repeated loading and varying span length has an effect on the results. In the micro-fatigue test it is shown to increase the chance of fibre breakage. For commercial glass fibres, no clearly discernible effect was detected from measuring 30 to 50 droplets from a span of 10 - 15 mm. The result for one fibre resin combination is, however, hardly conclusive for every fibre matrix combination – especially considering more challenging combinations such as natural fibres or thermoplastic matrices.

On a larger scale, another issue – as is common in material testing at varying length scales – is how representative the sampling is expected to be. In Publication I it was noted that the slope-based average IFSS from 10 filaments changes along the length of a roving for as much as 7.6 MPa. While this variation was similar in scale to the variation in these sets of 10 filaments, the behaviour also showed hints of a periodic trend along the roving. This is visualised in Figure 5.2. In addition to being on a scale to the rest of the experimental variation, this effect needs to be verified further due to uncertainty of the resin degree of cure. The fibres were measured in order, meaning the time from sample preparation to actual measurement also in-

creases with the roving length section. And as the degree of cure is one of the major uncertainties, some of this trend could simply be from post-curing or other sample ageing related effect.

5.2 Interphasial fatigue testing

In Publication II, the interphase of E6-CR17 glass fibres and 828 epoxy was characterised with microbond-based micro-fatigue test. The manuscript presents 108 succesful micro-fatigue experiments featuring two different interphase types: fully unsized interfacial contact between glass and epoxy, and sized glass fibres creating an interphase based on the cooperation of CA and film former as discussed in Section 3.1. The preparation of these interphase types was described in Section 4.1.3. The stress - number of cycles (SN) plots for the two interphase types are plotted in Figure 5.3. These results indicate a significant contribution to fatigue lifetime from the sizing. The droplets deposited on sized fibres exhibit better interphase durability under cyclic loading conditions, which is shown both by the SN and the Weibull
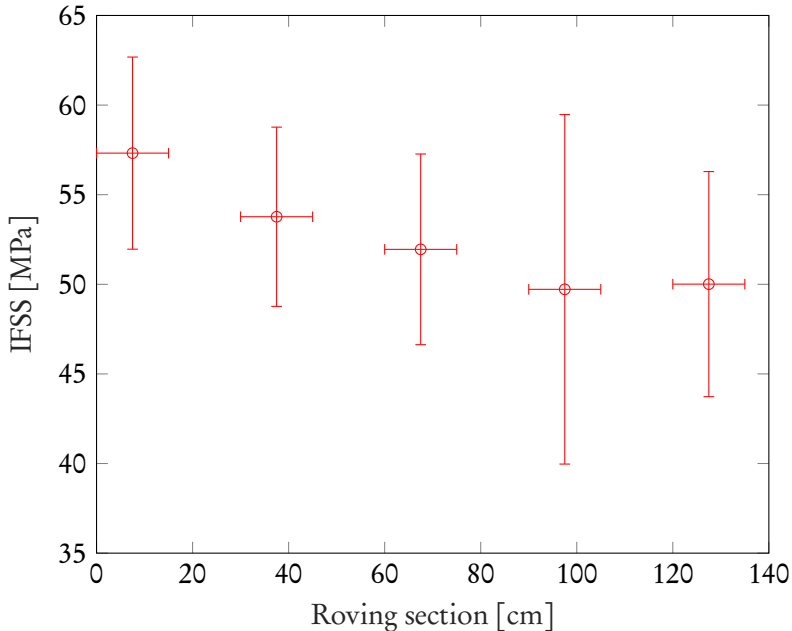
Figure 5.2 Variation of IFSS along the HiPer-tex W2020 roving. Horizontal error bars represent the 15 cm section of the roving from which the ten (10) parallel filaments were randomly selected.

69
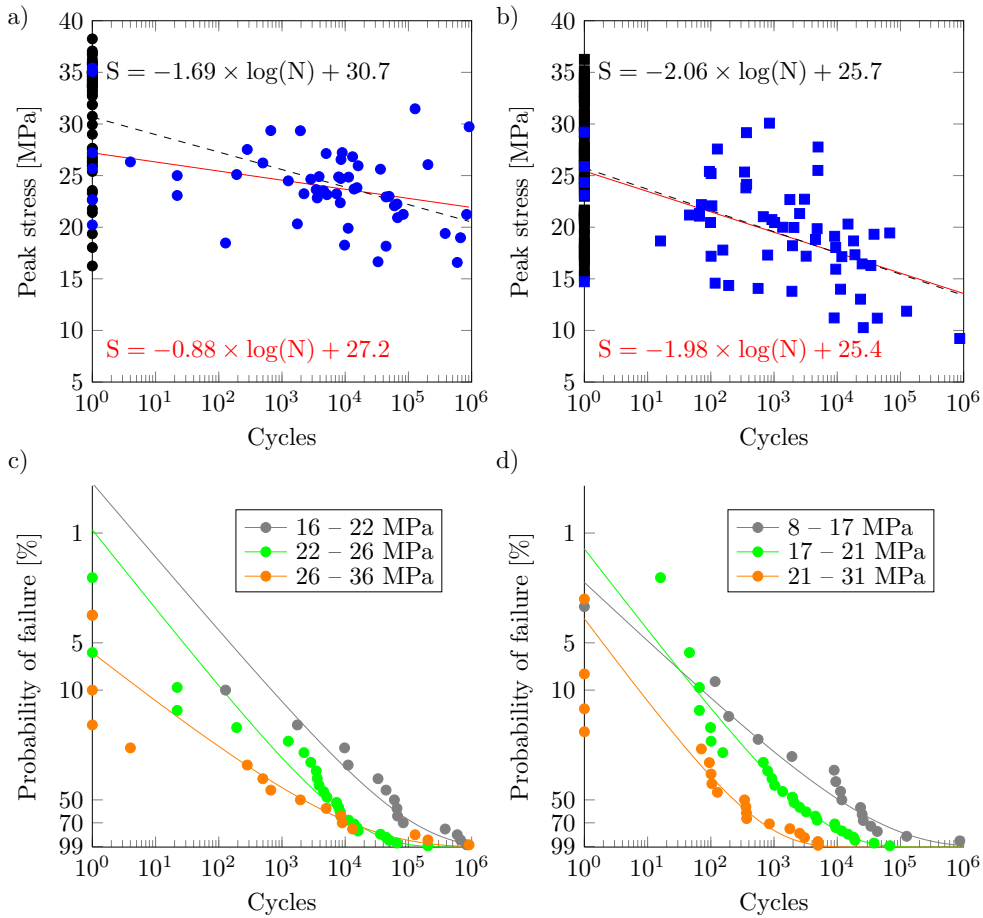
Figure 5.3 Results of the fatigue testing, SN plot of a) sized and b) unsized fibres at R = 0. Displacement rate: 2.0 mm/s (blue) 0.008 mm/s (black). The two fits signify data with (black, dashed) or without (red) the quasi-static results. Weibull probability plots for sized c) and unsized d) fibres, with data split into three stress level groups. [Publication II]

plots in Figure 5.3. This is especially notable at lower stress levels, where significantly longer fatigue lives can be predicted e.g., via the Weibull analysis. Under quasi-static conditions (displacement rate 0.008 mm/s), the sized fibres also out-perform the unsized interface – as depicted by the black datapoints in Figure 5.3.

The origin of the significant change to the slope of the sized SN plot from the inclusion of the quasi-static results is unverified and warrants further investigation. It is possible – if unlikely – that it is a probability-based phenomenon and that more lower performing samples were measured. However, a possible physical explanation exists based on strain-rate dependency. One of the frequently cited possible advan-

tages of the interphase is the capability of relaxing stresses and more or less repairing itself due to the significant role of non-covalent bonding to the overall structure. This would enable higher performance under low strain rate conditions where the reorienting and reforming of non-covalent bonds has time to contribute. It is therefore reasonable to expect a higher strain rate dependency from the sized interphase.

While the micro-fatigue test method proved very promising for qualitative analysis of interphase performance and provides valuable input for understanding the long-term durability of the interphase, correlation and variance analysis of the measured data revealed some anomalous behaviours, the origin of which is not readily apparent. Most probable contributions are the same as for the quasi-static test (Table 5.1), but the relative importance of the different factors needs to be investigated further. A high data volume investigation and further development are needed to reach a level of reliability suitable for quantitative results from the methodology.

5.3   Interfacial characterisation

While micro-mechanical tests are at the forefront of the utilised experimental methods for interphase characterisation, various other approaches were attempted to support and further understand the phenomena observed in micro-mechanical tests.

5.3.1   Key aspects of resin chemistry

Resin chemistry has a very significant role in the overall formation of the interphase. The interplay of resin and film former – already discussed in Section 3.1 – is one of these. There is uncertainty over whether the film former acts as an unreactive, protective coating of the fibres later dissolved by the matrix, thus affecting the interphase mainly through stoichiometry and chemical purity, or if it provides a major structural contribution via bonding with the CA and/or the fibre surface.

Non-covalent interactions between the different structural constituents at the interphase are also a critical part of the overall performance and structure of the interphase, as they are known to affect many chain morphology related aspects of polymers: glass transition, orientation, and free volume among the most significant for thermoset materials. Various non-covalent interactions of epoxy molecules were studied via DFT as a part of Publication III – mainly in terms of reaction energetics

and stable conformations. Even so, some limited generalisations can be drawn based on the types of interactions seen in the computations. The most significant of these are presented in Figure 5.4
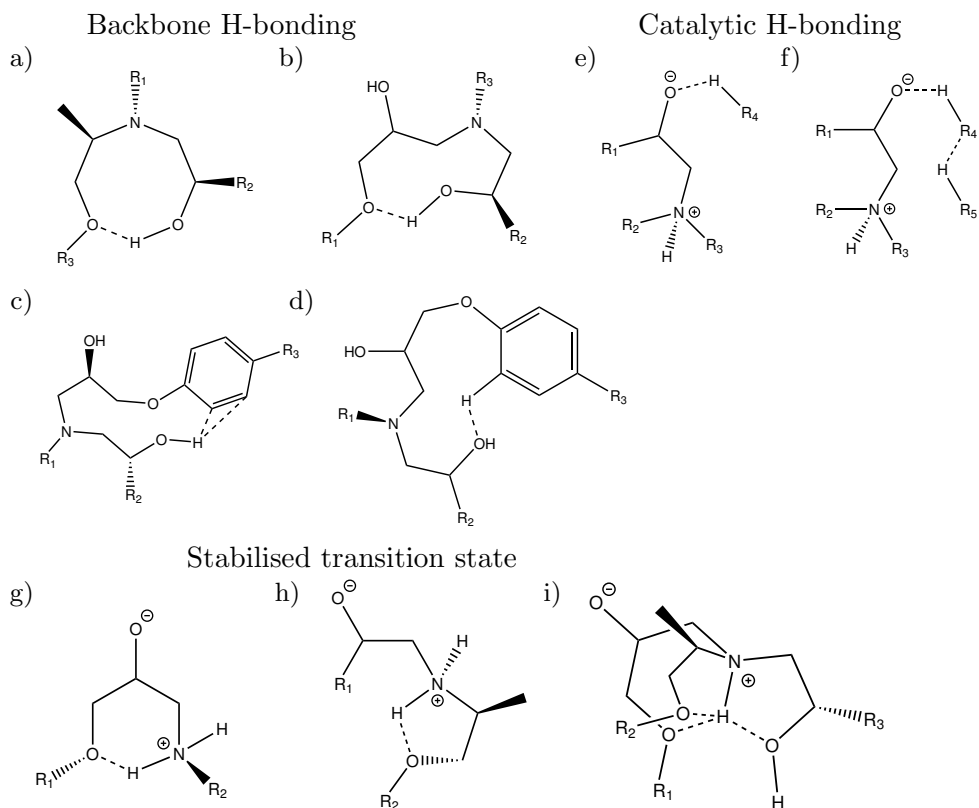
Figure 5.4 Major non-covalent interactions of epoxy - amine resins based on DFT computations in Publication III. Structures are grouped as stable reacted structures with interactions between elements of the polymer backbone (a-d), transition states formed by catalytic hydrogen bonding from a neighbouring hydroxyl or amine group (e-f) and transition state complexes stabilised by amine hydrogen interactions.

While the interactions are centred around the reactive core, the transition states highlight the various forms of hydrogen bond type interactions common to epoxy-amine systems. These include simple hydrogen bonding (Figure 5.3 a) and b)), aromatic hydrogen bonding [76] (Figure 5.3 c) and d)) and complex hydrogen bonded networks (Figure 5.3 g) - i)). Some – such as the complex in Figure 5.3 i) – are unique to the transition state. But the hydrogen bond type interaction with the aromatic ring (Figure 5.4 c)) in particular is both possible and rarely discussed for larger epoxy

structures and could even contribute as a potential interaction mechanism with glass surfaces [77].

Additionally, the non-covalent interactions in Figure 5.3 can notably affect the reactive path of the curing reaction and – considering e.g. the water and other hydrogen bonding capable moieties present in the sizing – contribute heavily to the overall process of interphase formation. As such, they should be investigated further by modelling the atomistic detail on a suitably large system size. Such studies are already quite frequent for carbon surfaces and carbon nanotubes [4, 78, 79] due to the more favourable length scale and often simpler interphase composition of carbon-based reinforcements. It is also worth noting that model systems incorporating thousands of atoms are currently only suited for empirical force field based simulations, which can only predict interactions that have been included in the force field unlike QM methods such as DFT.

Stoichiometry represents another important aspect of final resin and interphase properties. Several phenomena have been noted to affect the local stoichiometry of even a relatively perfect resin mixture. At the interphase, it is mainly affected by the functionalities of the CA and the film former as discussed earlier.

The possible resin-gas interphase related phenomena are especially important for the case of microcomposite testing. Depending on the molecular weight, various epoxy constituents – the epoxide molecules themselves or hardener molecules – can have suitably high vapour pressures to be considered volatile. This is exacerbated by the surface-to-volume ratio of the picolitre-scale microdroplets, which overall can result in significant changes to the stoichiometry. And while for a macroscale sample this would be considered a small localised change e.g. at an open mould surface, for a microdroplet this evaporation can have a noticeable effect on the overall properties of the resin droplet – and in extreme cases even prevent sufficient curing altogether. Figure 5.4 presents coupled TGA-FTIR measurement for 828 resin mixture. In Figure 5.4 most of the signals are detected after the onset of degradation of the resin around 300 °C. It is, however, notable that well before that – at around 80-100 °C – there is a small but clear signal that shares the detectable vibrations prominent in the IR spectrum of the pure hardener in a similar measurement (Publication IV). Even more surprising is the relatively early onset of small amounts of the DGEBA component evaporating. Overall, the whole resin mixture shows some volatile behaviour even at temperatures sometimes used in curing, and any related issues are definitely
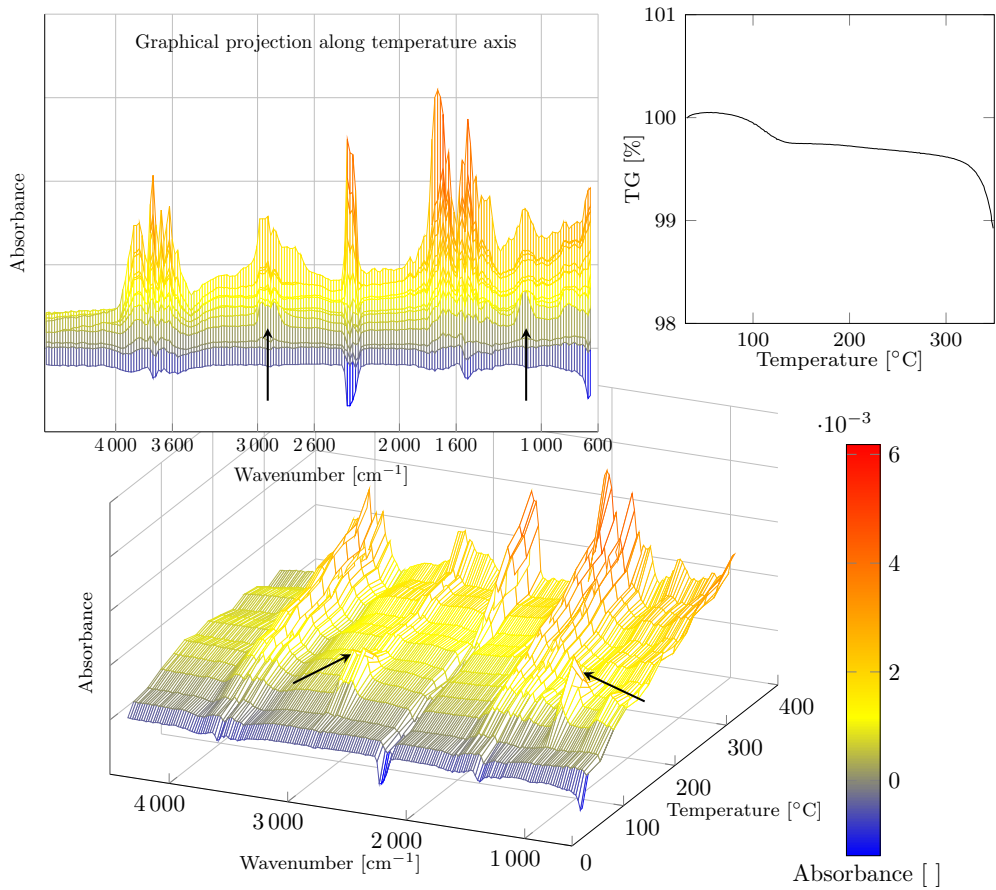
Figure 5.5 Results of a coupled TGA-FTIR measurement for 828 resin (DGEBA epoxide with poly(oxypropylene)diamine hardener). The corresponding TGA curve is included for reference. Arrows in the Figure indicate FTIR signals of evaporated hardener starting at approximately 85 °C. [Publication IV]

exacerbated in the droplet scale.

5.3.2   Degree of cure

The issue of conversion of the unreacted prepolymers to crosslinked resin, here discussed as degree of cure, was the major topic of Publication IV. The problem with microcomposite sample curing has been identified in literature [28, 29, 30] and very early also in the course of this work [33]. One of the key factors in this is the evaporation discussed in the previous section (5.3.1). However, the evaporation cannot

explain all of the difference – at least for the epoxy system 828. As a part of the study for Publication IV, factors such as sample length scale related changes to the morphology of the epoxy network were noted and are discussed here.

In Publication IV the primary method of investigation was *in-situ* nanoindentation mounted in an SEM. The method was selected due to being one of the only existing experimental methods that can directly test the resin in microdroplets. The mechanical response of microdroplets was compared to macroscopic samples in nanoindentation to quantify the difference in mechanical performance between the droplets – with unknown degree of cure – and the macroscopic Bulk samples. Table 5.2 shows a collected overview of the degree of cure and mechanical response of these Bulk samples, with comparison to different curing cycles simulated with MD for a model version of the same 828 resin system. For information on how these values were determined, refer to Publication IV. Despite quite notable differences in the modulus

Table 5.2 Overview of the nanoindentation results from cross-sectional cut and polished internal surfaces of Bulk samples and MD simulations for the 828 resin. The names of the Bulk samples indicate the employed curing cycle: RT signifies an initial 24 hours at room temperature and numeric values a (post-)curing treatment for eight (8) hours at the specified temperature (°C).

Sample	Modulus [GPa]	Conversion [%]	T_g [°C]	Hardness/Modulus [GPa/GPa]
Bulk RT	4.37±0.12	91.8	57.1	0.064±0.002
Bulk 50	4.36±0.20	93.2	61.9	0.062±0.002
Bulk RT-50	4.40±0.09	97.4	53.6	0.063±0.002
Bulk 80	3.95±0.07	99.3	83.5	0.069±0.003

T_{max} [K]	Modulus [GPa]	Conversion [%]	Residual Strain [%]
300	2.42 ± 0.30	81.7 ± 1.7	9.5 ± 0.5
400	4.22 ± 0.76	84.6 ± 2.4	10.1 ± 0.6
500	3.26 ± 0.44	88.8 ± 0.8	10.1 ± 1.3
600	3.18 ± 1.11	94.8 ± 1.1	9.5 ± 0.9
700	2.83 ± 1.19	98.1 ± 1.0	9.2 ± 1.2

values, the two methods show similar trends in terms of properties versus curing cycle. Both methods predict lower than expected mechanical properties for the most rapid curing cycle, which is expected to result from either early vitrification [57, 80] or the formation of nanoscale morphology that averages into lower mechanical

propertieson a larger scale [81, 82, 83]. While early vitrification limiting the conversion seems an intuitive explanation, the experimental glass transition temperatures and high conversions present a strong argument for the nanostructrural differences as the origin.

Sample surface related changes in nanoindentation hardness and modulus values have been reported in literature [84] and could partially explain the significant difference in hardness values between the micro- and macroscale samples. Interestingly, in nanoindentation studies the result is consistently higher hardness due to dynamic interphase formation at the indentation site [85] and the effect is likely stronger with increased molecular mobility, i.e. lower degree of cure [84]. A better comparison value is therefore provided by the hardness/modulus ratio [84], the values of which for the macroscale samples are provided in Table 5.2. The corresponding values for microdroplets are 0.056 ± 0.007 for samples indented shortly after preparation and 0.071 ± 0.004 after a 5-6 month storage in a vacuum sample storage cabinet. This indicates both a low degree of cure ($\leqslant$90%) for fresh samples and significant post-curing during storage.

The curing behaviour of the resin was further analysed by monitoring the crosslinking simulations described in Section 4.4.2. As the simulation was phenomenological and did not include an actual kinetics model, it could not be used to draw any definitive insights into the curing of the epoxy system. The early stages of the simulations were determined by the maximum amount of crosslinks permitted for each iteration. After the gel point of the resin, the kinetics become diffusion-controlled [57], and some interesting qualitative observations could be made based on the simulations. The iterative crosslinking of the polymer network is presented in Figure 5.6. Gelation occurs in 30-40 iterations (62-70% conversion) and corresponds with the point in the Figure where the primary amine reactions start to 'saturate' and the secondary amine reactions differentiate significantly. After this point the simulation is able to capture some of the diffusion-related kinetics in the network formation. If the thermal energy of the system is low, very few reactions occur. Outliers can occur as evidenced by the T_{max}=400 K simulations, but the conversion propagates slowly. The variance between the five parallel simulations is also quite high for the low thermal energy simulations, which also indicates that the systems are not fully vitrified. For the simulations to temperatures higher than 500 K, the behavioural trend of the simulations becomes more predictable. The extra crosslinks created at
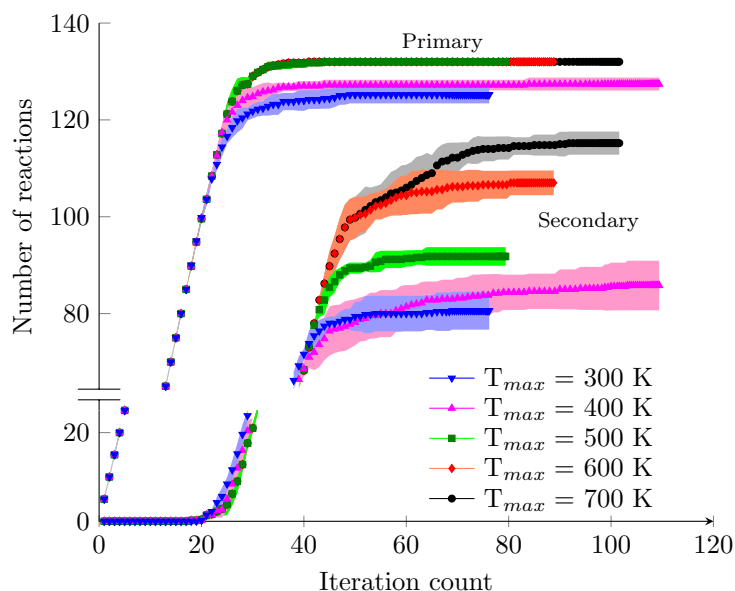
Figure 5.6 Primary and secondary amine reactions during crosslinking simulations. Heating cycle simulations 300 K to T_{max}. The scatter plot represents the average and the shaded area the standard deviation of five (5) parallel simulations. [Publication IV]

higher temperature cause vitrification to occur once the system is cooled down.

The stress-strain behaviour of the crosslinked resin was noted to correlate significantly with hydrogen bonding within the molecular network. The estimated number of hydrogen bonds within the network versus simulation time and corresponding stress levels is presented for several cyclic stress-strain simulations in Figure 5.7. For many of the simulations, changes in the stress strain behaviour correlate with the predicted hydrogen bonding. Some simulations, however, show less changes in hydrogen bonding – such as Figure 5.7 d) – and often also exhibit much lower stress levels during the deformation. System size and other practical simulation aspects contribute to the result, and further work is needed to explore the behaviour. The variation of the results hints at significantly different morphologies between the five parallel simulations, and a larger simulation box with significantly more input molecules could provide results that are easier to interpret.

To explore the relation of hydrogen bonding and morphology, $T_{max} = 600$ K simulation box 2 – for which the stress-strain data is presented in Figure 5.7 c) – was visualised at specific frames of the trajectory corresponding to changes observable in Figure 5.7. These frames are presented in Figure 5.8 and comprise: the start of
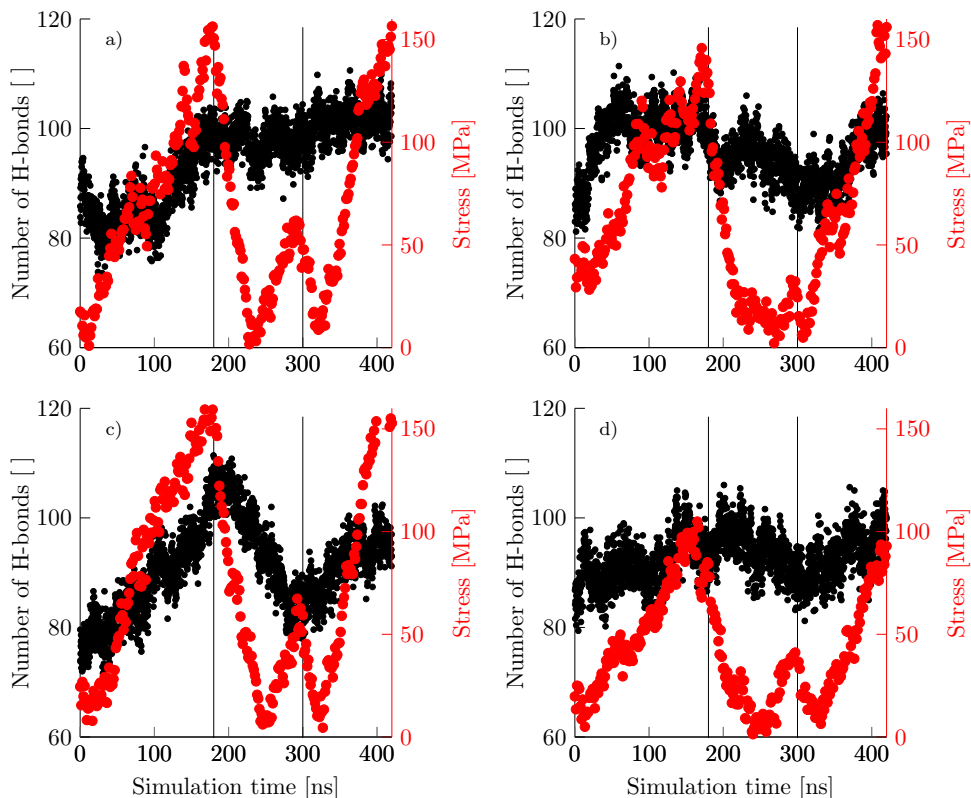
Figure 5.7 Potential hydrogen bond interactions during the cyclic compressive stress-strain simulations of epoxy resin from selected simulation runs. Stresses are plotted in red for comparison. Vertical lines indicate different stages in the cyclic loading (compression-unloading-compression). a) $T_{max} = 400$ K, b) $T_{max} = 500$ K, c) $T_{max} = 600$ K and d) $T_{max} = 700$ K. (see Table 5.2) [Publication IV]

the simulation (Frame 1), first notable peak in hydrogen bonding at around 105 ns (Frame 10478), peak load at around 181 ns (Frame 18116) and the minimum load during the unloading stage (Frame 24901).

The complex hydrogen bonded networks appear concentrated to specific regions of the simulation box. These sites could represent regions where the hydrogen bonding coordinates crosslinking sites in close proximity, creating exactly the type of nanoscale regions of high crosslinking (and hydrogen bond) density described in literature [81, 83]. Aromatic hydrogen bonds – in this case limited to ones with an aromatic donor – contribute significantly to these regions.
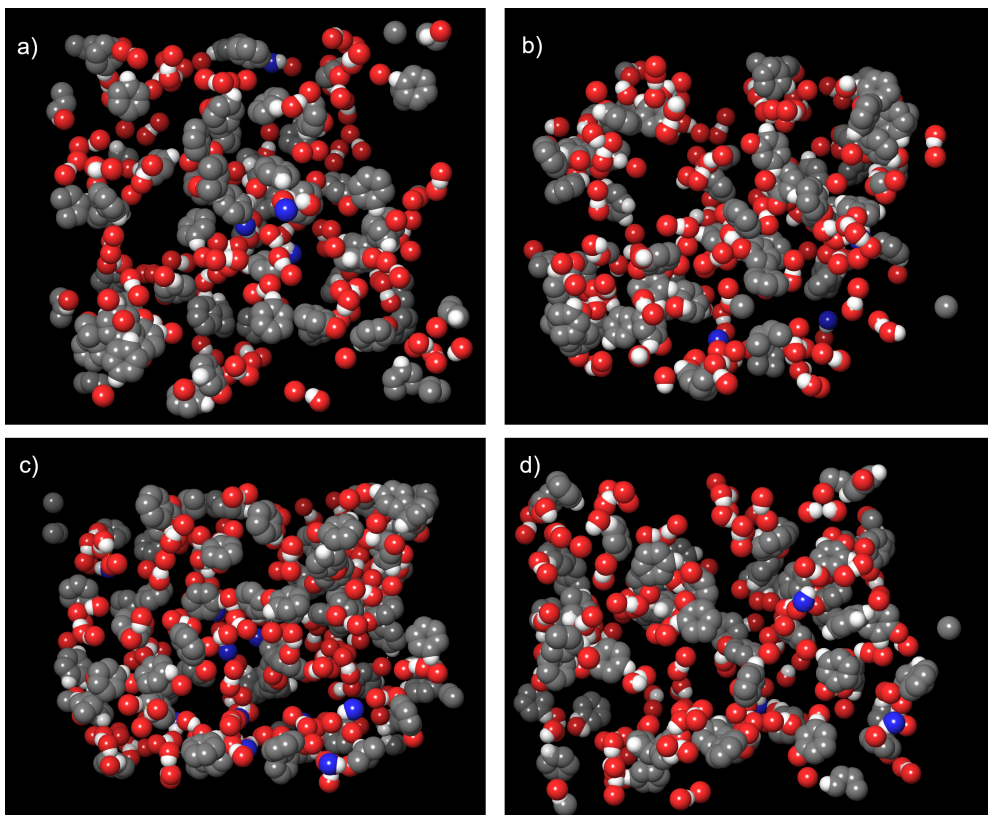
Figure 5.8 Alternative visualisation for Figure 6 in Publication IV. Simulation box orientation is identical for all four trajectory frames. Hydrogen-bonded moieties are visualised in space-filling representation, while the rest of the polymer network is hidden, i.e. voids correspond to regions without hydrogen bonding. a) frame 1 (0 ns), b) frame 10478 (105 ns), c) frame 18116 (181 ns) and d) frame 24901 (249 ns).

6 DISCUSSION

6.1 Experimental validation of microcomposite testing

During this work, a significant effort is afforded to transparent and thorough examination of the strengths and development needs of the adopted microcomposite testing methodology. The motivation is to push against the sometimes dismissive or ambivalent attitude these methods have faced in recent years. Hopefully, some of the developments presented as a part of this work will serve as a model or a blueprint for best practices and the next generation of experimental setups for this type of testing. This section aims to summarise and discuss these strengths, in terms of both throughput and reliability and the supporting information for their validation. As a part of this, any unresolved questions, problems and development needs are discussed where relevant.

6.1.1 Statistical reliability

In Publication I the FIBRObond testing setup is used to measure a test series of approximately 1,500 droplets from a total of 50 individual glass fibres. Firstly, this clearly highlights the strengths of the device as a high-throughput method compared to most approaches presented in literature. This data volume also allows for clear distinction of sources of experimental scatter arising from the method from those inherent to the sample itself. Measuring upwards of 30 droplets from each filament from a span of 10–15 mm is clearly shown to result in very linear datasets with very little scatter in the results. Instead, the total variation observed in the results arises from differences between the individual filaments.

Another source of scatter in reported results discussed in Publication I is the determination of embedded length of the droplet. One of the key strengths of the

microbond method over single fibre pull-out is the ease of determining embedded length from microscopic imaging. The meniscus region of the droplet, however, comprises a good portion of the total embedded length, and depending on the available imaging equipment and operator preferences and/or biases the same droplet can result in somewhat inconsistent values. A possible solution is presented in the form of a computer vision algorithm working with the device's microscopic optics to enable more consistent embedded length results by removing the dependency on operator bias. This helps improve the consistency of the methodology within research labs or even throughout the field should the practice be adopted widely with clear standardisation on the procedure.

For the micro-fatigue test, the number of tested samples was likewise unprecedented but unfortunately not sufficient for an equally comprehensive picture on the behaviour. The Weibull analysis used in the study benefited from separation of the data into three fairly distinctive groups that, especially for the mean stress group, behaved quite well form a statistical viewpoint. However, the ANOVA clearly indicated that some filament datasets were experiencing quite high scatter in the results. The origin of this variation is yet to be determined, but likely originates from the experimentation. Blade contact and the degree of cure of the droplets – already discussed in the theoretical part and in the results – are among the most likely culprits. Future steps for the method should include a similar study as conducted for the quasi-static test in Publication I: measuring a massive dataset from a single preferably commercial fibre-matrix combination. This would allow a more thorough analysis of the error sources, and help mitigate the previously experienced problems of fibre breakage and uncertain quality of fibre surface treatments. The higher variance in actual sample properties from non-commercial surface treatment is clearly seen in the quasi-static tests done for comparison in Publication II.

Thus, based on this work it can be stated that with careful and properly designed experimentation the high experimental scatter commonly sited for microbond and other microcomposite tests can be significantly mitigated. The better established quasi-static approach can provide consistent and statistically reliable data, which is reproducible independent of the operator (RQ1).

6.1.2 Agreement with existing theory

As discussed above, the microbond tests in this study follow almost exclusively a very reliable linear behaviour – especially in terms of datasets measured from the same filament. Using the slope of a maximum force versus embedded length/area fit is a well-established analysis method for IFSS, but needs to be approached carefully. The fit can only be considered really reliable for a single filament dataset, possibly extending to the whole set if each individual filament exhibits good quality results. Samples of vastly different properties are possible even in commercial samples that have undergone quality control to mitigate variance, as shown by filament #38 (see Figure 5.1). This clearly differentiates if the filaments are analysed individually (Figure 5.1 b)), but could easily distort a significantly smaller set of data with only a few droplets – or just one – measured per filament.

This linear behaviour can also be a little misleading, as it is an approximation. Engineers are usually quite familiar and even eager to use such approximations, but the underlying scientific theory should be kept in mind even when doing so. Figure 5.1 b) shows the microbond results fitted into the analytical model presented originally by Zhandarov (see Section 3.2), and outside of the few droplets with fibre volume fractions over the critical limit for the Nayfeh shear lag parameter the data shows quite excellent agreement with the model. Not only is this a very promising result for the applicability and validity of the experimentation, it also largely validates the use of the much less arduous linear approximation, provided the range of embedded lengths is suitable and statistical reliability of the data can be established.

As no similar analytical models for fatigue testing of interfaces and interphases exist, the theoretical validation of the micro-fatigue test is limited to its agreement with the conventions of fatigue testing [86]. Zero-cycle (N=1) results are not usually considered as a part of fatigue studies as, like the name suggests, the sample is not actually subjected to even a single full loading cycle. The significant number of N=1 data therefore cannot reasonably contribute to the discussion.

The employed methodology is thus also consistent with established theories, though a clearly defined analytical approach for microscale fatigue testing has currently not been established (RQ1). This presents an interesting avenue for future work on the topic.

6.1.3 Finite element analysis

The experimental microbond testing setups have been quite exhaustively simulated in FEA in work performed parallel to this [55, 56]. The FEA can provide complementary information and extend the applicability of the microcomposite testing results towards larger length scales by acquiring applicable interfacial constants such as critical stress τ_c and critical energy of debonding G_c.

Primary concerns in terms of experimental validity to which the FEA could provide insights include: 1) the strain rate dependency of results, 2) the role of adhesional and sliding friction especially with the contribution of the submicron-scale resin film, 3) the heating of the sample due to rapid cyclic loading, 4) compliance of the measuring system and corresponding disappearance of the debonding force kink [38] and 5) the free fibre length from the attachment point on the sample holder to the droplet being measured. Out of these five, three have been studied with direct ties to this work in Publication II – points 1)-3).

The strain rate dependency of the resin properties directly translates into the microcomposite test, and care should be taken to remain below a certain critical displacement rate dependent on the device and sample. For the FIBRObond setup utilised in this study, this critical displacement rate was determined as 0.5 mm/s. Above that the kinetic energy exceeds the internal energy of the system and the measurement should be considered dynamic. Important parameters directly affected by the dynamic nature include the energy dissipated due to plastic deformation, which could lead to heating of the sample.

Heating of the sample is also affected by the friction, exacerbating any heat generation due to plastic deformation. The primary role of friction in the test was the stabilisation of the damage propagation. While this was primarily studied for the micro-fatigue test, where it significantly increased the predicted fatigue life it should also apply directly to the quasi-static test. This phenomenon is likely also at least a partial explanation for the occasional observations during quasi-static measurements, where the propagating damaged region can be observed "travelling" at the interphase even while the measured force continues to increase. In the micro-fatigue test, similarities were noted between the change in damage propagation in fibres with different surface treatments and simulated micro-fatigue tests with different interfacial friction coefficients. This implies that the sizing contributes to the adhesional

friction at the interphase and thus promotes a more ductile, tough behaviour. (RQ2) The results appear promising, but much work remains in characterising the role of friction in the microcomposite tests.

Heating of the sample could cause changes in material properties and therefore distort any results. The micro-fatigue tests were performed in the dynamic range of the test where strain rate dependency of plastic deformation energy can cause additional heating. Though the role of friction was not considered, this heating was minimal ($< 0.4\,°C$). Interfacial friction increases the maximum heating gradient predicted by the simulation to $\approx 3\,°C$, which is still insufficient to alter material performance in any significant manner. Care should be taken when performing dynamic microcomposite testing, and further work is likely required to determine the exact operating ranges suitable for measurements.

6.2 Structure of the interphase

During this work, both commercial and laboratory-made glass fibre sizings and their resulting interfacial performance were tested. This, combined with the fairly in-depth exploration of the chemistry of the different components, can provide further insights into the chemical structure of the interphase, which to this day remains elusive due to its small scale and existence solely at the internal interface of two solid materials.

The components of the glass fibre - epoxy interphase comprise, at the very least, the surface silanol groups of the glass surface, water, silane CAs, film former (generally epoxy prepolymers) and the resin components. For the model system featured in Publication II, this composition should represent the whole system, but the commercial Araldite resin system is nevertheless fairly complicated.

Publication I features the HiPer-tex W2020 commercial glass fibres, for which the exact sizing composition is unknown and likely includes additional components such as emulsifiers and processing aids, in addition to which the exact nature of the CA and film former are unknown. The sizing is, however, reported as epoxy-compatible, which could translate to an aminosilane - epoxy film former combination. The interfacial performance with the Araldite resin for the two sizings – the laboratory-made model sizing and the commercial – is also very similar. A full dataset linear approximation of IFSS results in 44.52 MPa for the model sizing and

45.78 with the W2020 fibres. This is within experimental variation, considering the significantly smaller dataset for the laboratory sized fibres. It is therefore not unreasonable to try to draw together some conclusions based on all methods, as long as the uncertainties are acknowledged. The following sections represent an effort to summarise and find commonalities between the different aspects of the overarching work, with the goal of finding signs of specific chemical structures in the interphase.

6.2.1 Key properties of the interphase

Several key properties are commonly cited for functional composite interphase, mostly around the topic of facilitating and maintaining the capability of stress transfer between the fibres and the resin and therefore maximising the reinforcing effect of the fibres. As previously discussed, on a purely chemical level the functional groups required for interaction for many fibre resin combinations are already present. Surface functionalisation via sizing can improve the maximum stress that this interface can withstand, but in some – arguably rare – cases this is shown to not be necessary [3]. Instead, the primary purpose of the sizing should be stated as facilitating and *maintaining* the stress transfer capability throughout the lifetime of the composite material rather than simply improving it. This is, of course, in addition to the fibre processing and handling related roles it needs to also fulfil. Slightly shifting the focus in this sense is an important step to understanding the role of the different components and the resulting structure of the interphase. Table 6.1 summarises the key components of the interphase of a glass fibre epoxy composite and the roles suggested for the specific components during the formation of the interphase and in maintaining the stress transfer capability of the interphase.

The effects of sizing to mechanical properties

The microcomposite testing presented in this dissertation shows the critical importance of sizing for glass fibre FRCs. The comparison between glass fibres without an organic surface sizing and sized glass fibres (Publication II) clearly shows that, for the glass fibre epoxy FRCs, the sizing contributes positively to the "ultimate" strength of the interphase, i.e. the result of a quasi-static mechanical test. However, the more significant role seems to be the improved fatigue tolerance of the interphase, which is a much less studied phenomenon – at least with microcompos-

Table 6.1 Components and their suggested roles at the glass fibre epoxy interphase.

Component	Role in the interphase	References
Glass fibre	Covalent and non-covalent bonding with CA	[2, 6, 11, 77, 87]
	Non-covalent bonding with resin	
CA	Covalent bonds between fibre and matrix.	[2, 6, 7, 8, 12, 15]
	Covalent bonds between fibre and film former	
	Multilayer structure with various bonding states	
Film former	Dissolved and removed by the resin	[2, 20, 24]
	Mixing with, and plasticising the resin	
	Bonding with the CA and resin	
Resin (matrix)	Covalent bonding to CA	[2, 6, 7, 8, 15, 24]
	IPN formation with film former	
	Modified curing due to different chemical environment	
	Non-stoichiometric functional groups	

ite methods. The underlying phenomenon appears to be increased adhesional and sliding friction stabilising the damage propagation leading to a significantly reduced probability of a catastrophic debonding failure. On a structural level this could be explained through significant contributions of non-covalent bonding to the overall structure, which can contribute to stress transfer even after significant deformation as long as suitable bonding sites are present (adhesional friction). Sliding friction is also likely "improved" through the sizing plasticising the resin at the interphase region. (RQ2,RQ3)

Maximising strength versus a tough interphase

An important discussion related to the previous themes concerns the measured value of IFSS, more accurately whether it needs to be maximised or optimised. During these years working with the microbond method with numerous colleagues, a large variety of sample types has been explored. In addition to the expected carbon, glass and aramid fibres with thermoset resins (epoxies and vinyl- and polyersters) these studies have explored natural fibre composites [88], thermoplastic matrices and even elastomer matrix composites [89]. Alongside this variety of materials, a comparably broad range of behaviours and performance levels has been noted and analysed. As

an overarching conclusion of interfacial behaviour from these studies, many hints about the importance of ductility opposed to strength can be drawn. For an inherently incompatible matrix, such as polypropylene [90], stiff behaviour generally means a poor interphase and increased IFSS generally means a better interphase. More ductile behaviour is seen once the strength of the interphase approaches the scale of matrix properties.

For glass and carbon fibre - thermoset FRCs, results with supposedly high performance components resulting in either poor interphase performance or "too good" bonding have been noted. Both result in very stiff droplet behaviour and sudden catastrophic debonding stemming from different parts of the microcomposite. For the first – poor interphase – loading the droplet shears the droplet from the fibre surface with very low force, likely due to improper interphase formation and thus poor stress transfer capability solely through sliding friction. The latter case usually relates to non-commercial highly modified fibre surfaces intended to induce effective covalent bonding and/or mechanical interlocking with the matrix [5], and resulting in very high IFSS values approaching, achieving or even surpassing resin properties. While these results are definitely indicative of strong interfacial adhesion though covalent bonds and/or mechanical interlocking, two worrying concepts arise when considering such results. The first is related to the applicability of the microcomposite methodology, as such results frequently show that a significant portion of the failure is actually cohesive failure of the matrix – in extreme cases almost fully. A combined failure mode of crack propagation "random jumps" through the interphase shows excellent performance and the overall failure energy is significant. This should translate to excellent composite performance, but where can the line be drawn? If the failure mode is fully shearing through the resin, is the method actually measuring what we expect it to? This is an argument frequently given by those raising concerns over the validity of the microcomposite methods.

A second concern over such results relates to the previous discussion of fatigue tolerant interphase and the role of non-covalent bonding at the interphase. These results could be used to argue that most commercially employed sizings aim at creating this type of ductile, fatigue tolerant interphase instead of maximising the "ultimate" IFSS. An important open question remains whether this is by design – i.e. maximising the interfacial strength through extensive covalent bonds can be a hindrance in terms of fatigue behaviour, damage tolerance or environmental durability – or

whether these high performance interphases are truly the next generation of high end composites. (RQ2)

Role of the sizing in composite curing

While the primary goal of studying the epoxy curing was to troubleshoot and solve the issues related to microcomposite curing, the data on the changes in resin cure at various states and environments is also important for considering the structure of the interphase. Based on the available data and literature, mixing of the matrix resin with at least the film former portion of the fibre sizing is expected, with some interaction and/or mixing with other constituents – such as the CA – being very likely. Overall, the conclusions can be drawn that the curing environment of the resin at the interphase differs significantly from bulk and that the matrix resin is the most abundant component of the whole interphase region. Hence, understanding the resin behaviour in the interphase formation is a crucial component of understanding the overall interphase.

In Publication III the role of surrounding functional groups on the reactivity of epoxy amine systems is explored. Hydrogen bonding is shown to significantly reduce the initial barrier energy of the reaction, while also possibly altering the mechanism of the reaction by stabilising the intermediate product of the reaction into a local minimum. This can result in one of three changes to the curing reaction: 1) The altered mechanism is superseded by the overall reduction in barrier energy and the reaction is accelerated, 2) the reaction needs to surpass a secondary barrier energy to advance to the fully formed amino alcohol structure, reducing the reaction rate despite the lower barrier energy and 3) as before but the stabilised intermediate structure promotes nearby oxirane ring-opening and locally catalyses nearby reactions promoting the formation of highly crosslinked regions. Depending on the sizing formulation the interphase region can have much more hydrogen bonding capable moieties than bulk resin. These can include silane – unreacted silanol, amines, epoxides – and film former functional groups, water and possibly other components or modifications. Most significant of these are the silanols and water. The components with functionality directly associated with the epoxy curing also have an effect, but one that is more related to the other change in resin curing at the interphase – the stoichiometry. (RQ3,RQ4)

The role of proper stoichiometric ratios to the curing of epoxies has been stud-

ied extensively, and a wealth of data is already available in literature (e.g. [27, 91, 92, 93]). Many sizing formulations, however, disrupt the resin stoichiometry at the interphase, which should result in changes to the overall curing state. These studies generally conclude that, for epoxy-amine systems, an amine-rich stoichiometry is generally better than amine-depleted stoichiometry, while having some potential advantages compared to on-point stoichiometry. If nothing else, this at least explains the prevalence of aminosilanes in sizing component discussions. Further studies on the sizing effect on overall stoichiometry and the resulting properties could provide valuable insights into the topic.

6.2.2   Formation of the interphase - the big question

Several – sometimes contradictory – hints about the formation of the interphase structure have been suggested (Table 6.1). The previous discussions about the observable behaviour of the interphase can be used to draw further conclusions about the overall formation and structure of the interphase region. Unfortunately, the timeframe and scope of the study was not large enough for a detailed study on the formation of the interphase with e.g. MD – discussed further in Section 6.4. However, based on the microcomposite tests on commercial and laboratory-made sizings, focus at least on current state-of-the-art commercial fibres seems to be the formation of a durable, ductile and damage-resistant interphase instead of maximising the IFSS. Based on the information available on the chemistry of components, this interphase would be quite well in line with the hypothesis presented in Section 3.1.

The interphase close to the fibre surface comprises mainly of CA, film former and water deposited on the surface during the fibre manufacturing. The principle of like-attracts-like should drive the structure towards a silane-rich layer directly on the fibre surface with a composition gradient of film former rich outer surface, but unless the CA is initially deposited as a separate processing step the formation of a pure silane monolayer is quite unlikely. A somewhat crosslinked silane network stabilised by non-covalent bonds is far more likely. As an aminosilane - epoxy film former combination is considered to be the most common example in this work, some crosslinking likely extends to the more film former rich region of the sizing. Water can bond to the various components via hydrogen bonds to keep the structure ductile and expanded, likely also facilitating the interdiffusion of the sizing and

the resin components during composite manufacture. Nature offers a very familiar example of such behaviour in skin and leather. This also explains the limited storage time of sized fibres. During storage, especially improper storage, the sizing loses some of this water, causing the sizing to contract, becoming harder for the resin to penetrate and mix with. As the mixing with the existing crosslinked network is reduced, the interfacial properties of the composite become less dependent on the intended interphase and are instead determined by the interface between the sizing layer and the resin. The better these two mix, the greater the potential for both covalent and non-covalent bonding between the sizing layer and the resin, not to mention any potential entanglements between the two polymer networks (IPN). As this would be a diffusion-controlled process, the film former rich portions of the interphase would mix most with the resin, leading to an epoxy-rich local stoichiometry limiting the achievable degree of cure, with the excess epoxy plasticising the resin in the interphase region. (RQ4)

While this is hardly conclusive, the suggested interphase structure would explain many – if not all – of the observations made during this study on the behaviour of the interphase. Emerging technologies on interphase modification often fall outside the proposed structure, and their implications outside of the available preliminary results are difficult to predict. This ductile interphase is shown to be quite fatigue-tolerant and, if indicative of the real commercial applications as the data suggests, also quite resistant to environmental factors. Further improvements on these aspects would benefit significantly from definitive understanding of the strengths and weaknesses of the current state-of-the-art, to which hopefully the work in this dissertation contributes. Further studies on the interfacial fatigue of commercial composites along with modelling and visualisation of the interphase with methods such as MD or quantum mechanics/molecular mechanics (QM/MM) hybrid simulations [94] would likely provide the best avenues of expanding upon this work in the future.

6.3 Microcomposite curing

While the great potential of microcomposite testing has clearly been highlighted, the uncertainties related to resin cure are still somewhat unresolved and will likely remain so for the foreseeable future. Careful sample preparation can mitigate the is-

sue by providing similar, sufficiently cured microcomposite samples for comparative studies. The significant post-curing of droplets detected as a part of Publication IV also warrants further investigation, and consistent procedures in the time between droplet preparation and microbond measurements should be employed to ensure comparable results. The selection of epoxies for such studies also has a large role in determining how or if suitably cured droplets can be prepared [32]. Careful analysis of the data and checking against existing theory can help validate any high-quality work, and thus FEA remains one of the most important supporting tools for microcomposite testing. However, care should be taken when selecting the correct material properties for the model.

Unfortunately, the evaporation of resin components due to the surface-to-volume ratio cannot fully explain the scale-related effects in microcomposite curing. The effects of volatile component evaporation can be reduced with various methods such as pre-gelling and rapid curing of the resin, or in more extreme cases even counteracting the increased vapour pressure via external pressure or atmosphere. Rapid curing is, however, shown to affect the formation of the polymer network and thus the resulting mechanical behaviour of the resin. While evidence of nanoscale morphology in epoxy resins has been discussed for decades, more detailed studies have only been possible through advances in atomic-level microscopy and atomistic-scale modelling [83, 95]. Combining results from different scales – as well as combining experimental and simulated results – always presents significant challenges and opportunities with this topic being no different. Nevertheless, it is clear that the atomistic-scale aspects of the crosslinked network formation have significant implications on many related fields of study, from microscale testing to further options in tailoring resin properties [96, 97], and need to be studied further. (RQ4)

6.4 Future work

The topic of the interphase is a vast one and, despite several decades of previous studies, far beyond anything a single doctoral dissertation can encompass. This section highlights some ideas on pathways to continue working on the topic. The motivation during this work to explore the capabilities of computational chemistry methods was in large part to find a potential avenue for simulation and visualisation of the chemistry of the interphase region. The importance of understanding

the crosslinked epoxy network on an atomic level was only fully realised during the work, and it is a happy accident that these two topics are somewhat complementary – at least in simulation methodology. Originally this dissertation was intended to focus on the ageing of the interphase, only for the realisation to arise that too many unknowns persist in the nature of the interphase itself to enable a comprehensive study on its ageing that would provide significant novelty compared to existing literature on the topic. While some of these questions persist, the improved testing methods – along with the potential shown by the simulations – should allow studies of interfacial ageing on an unprecedented level of detail.

6.4.1 Interfacial modelling

In Section 5.3.2 and Publication IV, the various simulation workflows utilising MD and other atomistic simulations are shown to be powerful tools for exploring the structure property relations of crosslinked networks in significantly more detail than just in terms of functional groups and average composition. These methods have succesfully been employed in literature to study various interfacial regions with epoxy, such as carbon nanotube [78] (CNT) and carbon fibres [4]. Likewise, outside the field of composites similar approaches are used to study the interactions of silica [77, 87, 98, 99, 100] and other metal oxide surfaces [101] with various polymer compounds. Therefore, it is reasonable to conclude that the method could be effectively utilised for exploring and visualising the performance of various glass-epoxy interface compositions and helping understand the optimal interphase composition. Once successful, this should help optimise the complex combination of chemical durability, strength and toughness required for long-term durability of the interphase region (RQ3) and possibly also provide more options for tailoring for specific applications.

6.4.2 Ageing, long-term durability

As can also be observed from the scientific background in Chapter 3, a significant portion of the earliest information regarding the structure of the glass fibre - matrix interphase is from studies on ageing and environmental degradation of the interface. This also relates to the fact that a significant driver for the development of glass fi-

bre sizings has been improving the hydro- and hygrothermal ageing performance of composites. Despite the long history of the topic, the ageing of composites – frequently cited as being heavily interphase-dependent – remains a field of significant active study. Fully understanding the complex behaviour of the interphase region requires a comprehensive understanding of all the components, from the leaching of the glass surface structure, the contributions of covalent bonding and the formation of the silane layer to how the sizing alters the resin composition and correspondingly the curing state, structure of the crosslinked network, etc. None of these questions have been exhaustively answered. Hopefully, this thesis can provide a solid foundation for a new level of detail for studies on the chemistry of the ageing of glass fibre composite interphases in particular.

7 CONCLUSION

The main focus of this study was on the fundamentals of the glass fibre FRC interphase: how it can be measured, what it comprises, and how and if these two can be connected. This is arguably an important topic in the field of composite materials, as many of the questions posited throughout the text remain unanswered. Considering the complexity of the interphase, even based on the amount of components alone, this is hardly surprising. Such is the nature of research. Answering a few questions just leads to a new set of questions, and little by little progress is made.

The measuring methodology itself is frequently scrutinised in scientific discourse for bad reproducibility and high scatter of the results. This work shows that, while aspects such as the resin curing state or the quality of the fibre surface treatment can cause significant differences in – at least nominally – the same material combination, the method itself can provide reliable and reproducible data with properly designed experimentation. The remaining issues are not so much related to the methodology as they are to an underlying issue: That aspects of composite materials remain to this day unknown despite decades of experience and study on their properties and constituents. Sensitivity to fibre surface quality is very much the purpose of the method. The versatility of the microbond approach is further highlighted through a cyclic loading study exploring the fatigue life of the interphase and the applicability of the method to such experiments with very promising results. (RQ1)

With sufficient in-depth analysis, either through existing theory or FEA, micro-composite testing can help understand the interphase better. In this work, a combination of quasi-static and cyclic loading of microcomposite specimens indicated that state-of-the art interphases are intended to provide a good mix of ductility, strength and fatigue tolerance instead of maximising the quasi-static stress at failure. This behaviour is much more indicative of the contributions of non-covalent bonding and a plasticised structure than a rigid phase dominated by covalent bonding. This is in line with the proposed structure for the interphase of glass fibre reinforced compos-

ites. (RQ2)

The remaining issue of resin degree of cure was unfortunately not fully solved. A combination of computational and experimental work was utilised to understand the complex interplay between the resin batch scale, the curing environment and the chemistry of the resin components themselves. While changes in the resin due to mixing with the fibre sizing and the evaporation of resin components were part of the original hypothesis, the full importance of the morphological aspects in the network formation were only realised as the work progressed. (RQ4) Likewise, non-covalent bonding was factored in as a contributor to the formation of the resin network and the interphase, but the results indicate a much larger role to the overall morphology than expected. (RQ3) In a manner befitting a study more on fundamentals than application, what was learned was mostly how little is still known. Further studies on the performance and morphology of microscale epoxy samples would provide crucial input to understanding the properties of the resin part of microcomposite samples and how they relate to the resin in bulk or as a part of a composite. Based on the results and literature shown here, it is likely that all three are different. (RQ4)

REFERENCES

[1] J. Thomason. The interface region in glass fibre-reinforced epoxy resin composites: 3. Characterization of fibre surface coatings and the interphase. *Composites* 26.7 (1995), 487–498. ISSN: 0010-4361. DOI: `10.1016/0010-4361(95)96806-H`.

[2] M. Dey, J. Deitzel, J. Gillespie and S. Schweiger. Influence of sizing formulations on glass/epoxy interphase properties. *Composites Part A: Applied Science and Manufacturing* 63 (2014), 59–67. ISSN: 1359-835X. DOI: `10.1016/j.compositesa.2014.04.006`.

[3] S. Palola, P. Laurikainen, S. García-Arrieta, E. Goikuria Astorkia and E. Sarlin. Towards Sustainable Composite Manufacturing with Recycled Carbon Fiber Reinforced Thermoplastic Composites. *Polymers* 14.6 (2022). ISSN: 2073-4360. DOI: `10.3390/polym14061098`.

[4] D. J. Eyckens, B. Demir, J. D. Randall, T. R. Gengenbach, L. Servinis, T. R. Walsh and L. C. Henderson. Using molecular entanglement as a strategy to enhance carbon fiber-epoxy composite interfaces. *Composites Science and Technology* 196 (2020), 108225. ISSN: 0266-3538. DOI: `https://doi.org/10.1016/j.compscitech.2020.108225`.

[5] J. D. Randall, D. J. Eyckens, E. Sarlin, S. Palola, G. G. Andersson, Y. Yin, F. Stojcevski and L. C. Henderson. Mixed Surface Chemistry on Carbon Fibers to Promote Adhesion in Epoxy and PMMA Polymers. *Industrial & Engineering Chemistry Research* 61.4 (2022), 1615–1623. DOI: `10.1021/acs.iecr.1c04409`.

[6] J. Comyn. *Adhesion Science (2nd Edition)*. Royal Society of Chemistry (RSC), (2021). Chap. 3.2.1 Chemistry. ISBN: 978-1-78801-888-3.

[7] C. L. Schutte. Environmental durability of glass-fiber composites. *Materials Science and Engineering: R: Reports* 13.7 (1994), 265–323. ISSN: 0927-796X. DOI: `10.1016/0927-796X(94)90002-7`.

[8] O. Johannson, F. Stark, G. Vogel and R. Fleischmann. Evidence for Chemical Bond Formation at Silane Coupling Agent Interfaces. *Journal of Composite Materials* 1.3 (1967), 278–292. DOI: `10.1177/002199836700100304`.

[9] L. T. Drzal, M. J. Rich and M. F. Koenig. Adhesion of Graphite Fibers to Epoxy Matrices. III. The Effect of Hygrothermal Exposure. *The Journal of Adhesion* 18.1 (1985), 49–72. DOI: `10.1080/00218468508074936`.

[10] U. Gaur and B. Miller. Effects of environmental exposure on fiber/epoxy interfacial shear strength. *Polymer Composites* 11.4 (1990), 217–222. DOI: `10.1002/pc.750110404`.

[11] P. Laurikainen. Characterisation of the ageing of glass fibre-reinforced polymers. MSc thesis. Tampere University of Technology, (2017).

[12] H. Ishida. A review of recent progress in the studies of molecular and microstructure of coupling agents and their functions in composites, coatings and adhesive joints. *Polymer Composites* 5.2 (1984), 101–123. DOI: `10.1002/pc.750050202`.

[13] A. Chateauminois, L. Vincent, B. Chabert and J. Soulier. Study of the interfacial degradation of a glass-epoxy composite during hygrothermal ageing using water diffusion measurements and dynamic mechanical thermal analysis. *Polymer* 35.22 (1994), 4766–4774. ISSN: 0032-3861. DOI: `https://doi.org/10.1016/0032-3861(94)90730-7`.

[14] J. Mercier, A. Bunsell, P. Castaing and J. Renard. Characterisation and modelling of aging of composites. *Composites Part A: Applied Science and Manufacturing* 39.2 (2008), 428–438. ISSN: 1359-835X. DOI: `10.1016/j.compositesa.2007.08.015`.

[15] R. Gorowara, W. Kosik, S. McKnight and R. McCullough. Molecular characterization of glass fiber surface coatings for thermosetting polymer matrix/glass fiber composites. *Composites Part A: Applied Science and Manufacturing* 32.3 (2001), 323–329. ISSN: 1359-835X. DOI: `10.1016/S1359-835X(00)00112-3`.

[16]   F. Gnädinger, P. Middendorf and B. Fox. Interfacial shear strength studies of experimental carbon fibres, novel thermosetting polyurethane and epoxy matrices and bespoke sizing agents. *Composites Science and Technology* 133 (2016), 104–110. ISSN: 0266-3538. DOI: `10.1016/j.compscitech.2016.07.029`.

[17]   V. Matrenichev, M. C. Lessa Belone, S. Palola, P. Laurikainen and E. Sarlin. Resizing Approach to Increase the Viability of Recycled Fibre-Reinforced Composites. *Materials* 13.24 (2020). ISSN: 1996-1944. DOI: `10.3390/ma13245773`.

[18]   The Dow Chemical Company. *BYNEL™50E739*. 914-074-01-0221 DOW. Technical data sheet. 2021.

[19]   The Dow Chemical Company. *FUSABOND™P613*. 914-093-01-0221 DOW. Technical data sheet. 2021.

[20]   H. Honarkar. Waterborne polyurethanes: A review. *Journal of Dispersion Science and Technology* 39.4 (2018), 507–516. DOI: `10.1080/01932691.2017.1327818`.

[21]   A. P. Vassilopoulos. The history of fiber-reinforced polymer composite laminate fatigue. *International Journal of Fatigue* 134 (2020), 105512. ISSN: 0142-1123. DOI: `10.1016/j.ijfatigue.2020.105512`.

[22]   R. Talreja. Damage and fatigue in composites – A personal account. *Composites Science and Technology* 68.13 (2008). Directions in Damage and Durability of Composite Materials, with regular papers, 2585–2591. ISSN: 0266-3538. DOI: `10.1016/j.compscitech.2008.04.042`.

[23]   C. E. Demers. Fatigue strength degradation of E-glass FRP composites and carbon FRP composites. *Construction and Building Materials* 12.5 (1998), 311–318. ISSN: 0950-0618. DOI: `10.1016/S0950-0618(98)00012-9`.

[24]   E. Laukmanis, M. Janowski, S. Horn and J. Moosburger-Will. Effect of the interplay between fiber surface chemistry and sizing reactivity on fiber matrix interaction in carbon fiber reinforced epoxy resin. *Composite Interfaces* 29.12 (2022), 1325–1355. DOI: `10.1080/09276440.2022.2068249`.

[25]   B. J. R. Scholtens and J. C. Brackman. Influence of the Film Former on Fibre-Matrix Adhesion and Mechanical Properties of Glass-Fibre Reinforced Thermoplastics. *The Journal of Adhesion* 52.1-4 (1995), 115–129. DOI: `10.1080/0021846950815189`.

[26]   H. N. Petersen. Investigation of sizing - from glass fibre surface to composite interface. PhD thesis. DTU Nanotech, (2017).

[27]   R. F. Minty, L. Yang and J. L. Thomason. The influence of hardener-to-epoxy ratio on the interfacial strength in glass fibre reinforced epoxy composites. *Composites Part A: Applied Science and Manufacturing* 112 (2018), 64–70. ISSN: 1359-835X. DOI: `10.1016/j.compositesa.2018.05.033`.

[28]   P. Zinck, H. Wagner, L. Salmon and J. Gerard. Are microcomposites realistic models of the fibre/matrix interface? II. Physico-chemical approach. *Polymer* 42.15 (2001), 6641–6650. ISSN: 0032-3861. DOI: `10.1016/S0032-3861(00)00871-5`.

[29]   D. Bryce, J. Thomason and L. Yang. Micromechanical and spectroscopic characterisation of the curing performance of epoxy resins in the microbond test. *IOP Conference Series: Materials Science and Engineering* 942.1 (2020), 012019. DOI: `10.1088/1757-899x/942/1/012019`.

[30]   J. Thomason. An overview of some scaling issues in the sample preparation and data interpretation of the microbond test for fibre-matrix interface characterisation. *Polymer Testing* 111 (2022), 107591. ISSN: 0142-9418. DOI: `10.1016/j.polymertesting.2022.107591`.

[31]   B. Miller, P. Muri and L. Rebenfeld. A microbond method for determination of the shear strength of a fiber/resin interface. *Composites Science and Technology* 28.1 (1987), 17–32. ISSN: 0266-3538. DOI: `10.1016/0266-3538(87)90059-5`.

[32]   V. Rao and L. T. Drzal. Loss of Curing Agent During Thin Film (Droplet) Curing of Thermoset Material. *The Journal of Adhesion* 35.4 (1991), 245–249. DOI: `10.1080/00218469108041011`.

[33]   P. Laurikainen, S. Pötz, J. Jokinen, M. von Essen, M. Lindgren, P. Kallio, M. Kanerva, G. Oreski and E. Sarlin. High-throughput mechanical micro-scale characterization of composites and the utilization of the results in finite element analysis. *Proceedings of the 18th European Conference on Composite Materials*. Athens, Greece: European Society of Composite Materials, (2018). ISBN: 9781510896932.

[34] B. Miller, U. Gaur and D. E. Hirt. Measurement and mechanical aspects of the microbond pull-out technique for obtaining fiber/resin interfacial shear strength. *Composites Science and Technology* 42.1 (1991). Special Issue Interfaces in Composites, 207–219. ISSN: 0266-3538. DOI: `10.1016/0266-3538(91) 90018-K`.

[35] R. J. Scheer and J. A. Nairn. A Comparison of Several Fracture Mechanics Methods for Measuring Interfacial Toughness with Microbond Tests. *The Journal of Adhesion* 53.1-2 (1995), 45–68. DOI: `10.1080/00218469508014371`.

[36] S. Zhandarov, Y. Gorbatkina and E. Mäder. Adhesional pressure as a criterion for interfacial failure in fibrous microcomposites and its determination using a microbond test. *Composites Science and Technology* 66.15 (2006), 2610–2628. ISSN: 0266-3538. DOI: `10.1016/j.compscitech.2006.03.023`.

[37] S. Zhandarov and E. Mäder. An alternative method of determining the local interfacial shear strength from force–displacement curves in the pull-out and microbond tests. *International Journal of Adhesion and Adhesives* 55 (2014), 37–42. ISSN: 0143-7496. DOI: `10.1016/j.ijadhadh.2014.07.006`.

[38] S. Zhandarov and E. Mäder. Determining the interfacial toughness from force–displacement curves in the pull-out and microbond tests using the alternative method. *International Journal of Adhesion and Adhesives* 65 (2016), 11–18. ISSN: 0143-7496. DOI: `10.1016/j.ijadhadh.2015.10.020`.

[39] S. Zhandarov and E. Mäder. Peak force as function of the embedded length in pull-out and microbond tests: effect of specimen geometry. *Journal of Adhesion Science and Technology* 19.10 (2005), 817–855. DOI: `10.1163/1568561054929937`.

[40] B. Carroll. The accurate measurement of contact angle, phase contact areas, drop volume, and Laplace excess pressure in drop-on-fiber systems. *Journal of Colloid and Interface Science* 57.3 (1976), 488–495. ISSN: 0021-9797. DOI: `https://doi.org/10.1016/0021-9797(76)90227-7`.

[41] B. Song, A. Bismarck, R. Tahhan and J. Springer. A Generalized Drop Length–Height Method for Determination of Contact Angle in Drop-on-Fiber Systems. *Journal of Colloid and Interface Science* 197.1 (1998), 68–77. ISSN: 0021-9797. DOI: `10.1006/jcis.1997.5218`.

[42]   S. Rebouillat, B. Letellier and B. Steffenino. Wettability of single fibres – beyond the contact angle approach. *International Journal of Adhesion and Adhesives* 19.4 (1999), 303–314. ISSN: 0143-7496. DOI: `10.1016/S0143-7496(99)00006-8`.

[43]   J. A. Nairn. On the use of shear-lag methods for analysis of stress transfer in unidirectional composites. *Mechanics of Materials* 26.2 (1997), 63–80. ISSN: 0167-6636. DOI: `10.1016/S0167-6636(97)00023-9`.

[44]   E. Mäder, S.-L. Gao and R. Plonka. Static and dynamic properties of single and multi-fiber/epoxy composites modified by sizings. *Composites Science and Technology* 67.6 (2007), 1105–1115. ISSN: 0266-3538. DOI: `10.1016/j.compscitech.2006.05.020`.

[45]   H. M. Brodowsky, W. Jenschke and E. Mäder. Characterization of interphase properties: Microfatigue of single fibre model composites. *Composites Part A: Applied Science and Manufacturing* 41.11 (2010), 1579–1586. ISSN: 1359-835X. DOI: `10.1016/j.compositesa.2010.07.006`.

[46]   P.-S. Shin, J.-H. Kim, Y.-M. Baek, H.-S. Park and J.-M. Park. Epoxy Matrix with Adding Dopamine for Improving Mechanical Property and Interfacial Adhesion with Glass Fiber. *Composites Research* 32.2 (2019), 96–101.

[47]   R. Dsouza, M. Kakkonen, A. Prapavesis, E. Sarlin, P. Antunes, A. W. Van Vuure, P. Kallio and M. Kanerva. Does a polymer film due to Rayleigh-instability affect interfacial properties measured by microbond test? Unpublished manuscript.

[48]   Huntsman Corporation. *Araldite® LY 5052 / Aradur® 5052*. Technical data sheet. (2007).

[49]   HEXION Specialty Chemicals. *EPON Resin 828*. RP:3075. Technical data sheet. (2005).

[50]   Huntsman Corporation. *JEFFAMINE D-230 Polyetheramine*. 5191-0711. Technical data sheet. (2007).

[51]   F. Angeli, M. Gaillard, P. Jollivet and T. Charpentier. Influence of glass composition and alteration solution on leached silicate glass structure: A solid-state NMR investigation. *Geochimica et Cosmochimica Acta* 70.10 (2006), 2577–2590. ISSN: 0016-7037. DOI: `10.1016/j.gca.2006.02.023`.

[52]   C. Jégou, S. Gin and F. Larché. Alteration kinetics of a simplified nuclear glass in an aqueous medium: effects of solution chemistry and of protective gel properties on diminishing the alteration rate. *Journal of Nuclear Materials* 280.2 (2000), 216–229. ISSN: 0022-3115. DOI: `10.1016/S0022-3115(00)00039-8`.

[53]   A. Ledieu, F. Devreux, P. Barboux, L. Sicard and O. Spalla. Leaching of borosilicate glasses. I. Experiments. *Journal of Non-Crystalline Solids* 343.1 (2004), 3–12. ISSN: 0022-3093. DOI: `10.1016/j.jnoncrysol.2004.06.006`.

[54]   D. Seveno. Dynamic wetting of fibres. PhD thesis. Polytech. Mons, FPMS, (2004).

[55]   R. Dsouza, P. Antunes, M. Kakkonen, J. Jokinen, E. Sarlin, P. Kallio and M. Kanerva. 3D interfacial debonding during microbond testing: Advantages of local strain recording. *Composites Science and Technology* 195 (2020), 108163. ISSN: 0266-3538. DOI: `10.1016/j.compscitech.2020.108163`.

[56]   R. Dsouza, P. Antunes, M. Kakkonen, O. Tanhuanpää, P. Laurikainen, F. Javanshour, P. Kallio and M. Kanerva. Microscale sensor solution for data collection from fibre-matrix interfaces. *Scientific Reports* 11.1 (2021), 8346. ISSN: 2045-2322. DOI: `10.1038/s41598-021-87723-9`.

[57]   N. Sbirrazzuoli, S. Vyazovkin, A. Mititelu, C. Sladic and L. Vincent. A Study of Epoxy-Amine Cure Kinetics by Combining Isoconversional Analysis with Temperature Modulated DSC and Dynamic Rheometry. *Macromolecular Chemistry and Physics* 204.15 (2003), 1815–1821. DOI: `10.1002/macp.200350051`.

[58]   W. Oliver and G. Pharr. Measurement of hardness and elastic modulus by instrumented indentation: Advances in understanding and refinements to methodology. *Journal of Materials Research* 19.1 (2004), 3–20. DOI: `10.1557/jmr.2004.19.1.3`.

[59]   A. D. Bochevarov, E. Harder, T. F. Hughes, J. R. Greenwood, D. A. Braden, D. M. Philipp, D. Rinaldo, M. D. Halls, J. Zhang and R. A. Friesner. Jaguar: A high-performance quantum chemistry software program with strengths in life and materials sciences. *International Journal of Quantum Chemistry* 113.18 (2013), 2110–2142. DOI: `10.1002/qua.24481`.

[60] M. Alipour. Gauging the performance of some density functionals including dispersion and nonlocal corrections for relative energies of water 20-mers. *Journal of Molecular Graphics and Modelling* 75 (2017), 132–136. ISSN: 1093-3263. DOI: `10.1016/j.jmgm.2017.05.006`.

[61] D. Zheng and F. Wang. Performing Molecular Dynamics Simulations and Computing Hydration Free Energies on the B3LYP-D3(BJ) Potential Energy Surface with Adaptive Force Matching: A Benchmark Study with Seven Alcohols and One Amine. *ACS Physical Chemistry Au* 1.1 (2021), 14–24. DOI: `10.1021/acsphyschemau.1c00006`.

[62] S. Grimme, S. Ehrlich and L. Goerigk. Effect of the damping function in dispersion corrected density functional theory. *Journal of Computational Chemistry* 32.7 (2011), 1456–1465. DOI: `10.1002/jcc.21759`.

[63] K. Roos, C. Wu, W. Damm, M. Reboul, J. M. Stevenson, C. Lu, M. K. Dahlgren, S. Mondal, W. Chen, L. Wang, R. Abel, R. A. Friesner and E. D. Harder. OPLS3e: Extending Force Field Coverage for Drug-Like Small Molecules. *Journal of Chemical Theory and Computation* 15.3 (2019). PMID: 30768902, 1863–1874. DOI: `10.1021/acs.jctc.8b01026`.

[64] G. Chang, W. C. Still and W. C. Guida. An internal coordinate Monte Carlo method for searching conformational space. *Journal of the American Chemical Society; (USA)* 111.12 (1989). ISSN: 0002-7863. DOI: `10.1021/ja00194a035`.

[65] M. Bergdorf, S. Baxter, C. A. Rendlman and D. Shaw. *Desmond/GPU Performance as of November 2016.* Tech. rep. D. E. Shaw Research, (2016).

[66] *Schrödinger, Inc.* New York, NY, (2021).

[67] C. Lu, C. Wu, D. Ghoreishi, W. Chen, L. Wang, W. Damm, G. A. Ross, M. K. Dahlgren, E. Russell, C. D. Von Bargen, R. Abel, R. A. Friesner and E. D. Harder. OPLS4: Improving Force Field Accuracy on Challenging Regimes of Chemical Space. *Journal of Chemical Theory and Computation* 17.7 (2021). PMID: 34096718, 4291–4300. DOI: `10.1021/acs.jctc.1c00302`.

[68] K. H. DuBay, M. L. Hall, T. F. Hughes, C. Wu, D. R. Reichman and R. A. Friesner. Accurate Force Field Development for Modeling Conjugated Polymers. *Journal of Chemical Theory and Computation* 8.11 (2012). PMID: 26605615, 4556–4569. DOI: `10.1021/ct300175w`.

[69] S. Sockalingam and G. Nilakantan. Fiber-Matrix Interface Characterization through the Microbond Test. *International Journal of Aeronautical and Space Sciences* 13.3 (2012), 282–295. DOI: `10.5139/IJASS.2012.13.3.282`.

[70] C. Chou, U. Gaur and B. Miller. The effect of microvise gap width on microbond pull-out test results. *Composites Science and Technology* 51.1 (1994), 111–116. ISSN: 0266-3538. DOI: `10.1016/0266-3538(94)90161-9`.

[71] H. Heilhecker, W. Cross, R. Pentland, C. Griswold, J. J. Kellar and L. Kjerengtroen. The vice angle in the microbond test. *Journal of Materials Science Letters* 19.23 (2000), 2145–2147. ISSN: 1573-4811. DOI: `10.1023/A:1026787012473`.

[72] J. Ash, W. Cross, D. Svalstad, J. Kellar and L. Kjerengtroen. Finite element evaluation of the microbond test: meniscus effect, interphase region, and vise angle. *Composites Science and Technology* 63.5 (2003), 641–651. ISSN: 0266-3538. DOI: `10.1016/S0266-3538(02)00256-7`.

[73] M. Nishikawa, T. Okabe, K. Hemmi and N. Takeda. Micromechanical modeling of the microbond test to quantify the interfacial properties of fiber-reinforced composites. *International Journal of Solids and Structures* 45.14 (2008), 4098–4113. ISSN: 0020-7683. DOI: `10.1016/j.ijsolstr.2008.02.021`.

[74] P. Zinck, H. Wagner, L. Salmon and J. Gerard. Are microcomposites realistic models of the fibre/matrix interface? I. Micromechanical modelling. *Polymer* 42.12 (2001), 5401–5413. ISSN: 0032-3861. DOI: `10.1016/S0032-3861(00)00870-3`.

[75] D. A. Biro, P. McLean and Y. Deslandes. Application of the microbond technique: Characterization of carbon fiber-epoxy interfaces. *Polymer Engineering & Science* 31.17 (1991), 1250–1256. DOI: `10.1002/pen.760311704`.

[76] R. L. Brinkley and R. B. Gupta. Hydrogen bonding with aromatic rings. *AIChE Journal* 47.4 (2001), 948–953. DOI: `10.1002/aic.690470417`.

[77] S. Nakamura, Y. Tsuji and K. Yoshizawa. Role of Hydrogen-Bonding and OH-π Interactions in the Adhesion of Epoxy Resin on Hydrophilic Surfaces. *ACS Omega* 5.40 (2020), 26211–26219. DOI: `10.1021/acsomega.0c03798`.

[78] Y. Zhang, X. Zhuang, J. Muthu, T. Mabrouki, M. Fontaine, Y. Gong and T. Rabczuk. Load transfer of graphene/carbon nanotube/polyethylene hybrid nanocomposite by molecular dynamics simulation. *Composites Part B: Engi-*

neering 63 (2014), 27–33. ISSN: 1359-8368. DOI: `10.1016/j.compositesb.2014.03.009`.

[79]   S. Faragi, A. Hamedani, G. Alahyarizadeh, A. Minuchehr, M. Aghaie and B. Arab. Mechanical properties of carbon nanotube- and graphene-reinforced Araldite LY/Aradur HY 5052 resin epoxy composites: a molecular dynamics study. *Journal of Molecular Modeling* 25.7 (2019). ISSN: 0948-5023. DOI: `10.1007/s00894-019-4085-5`.

[80]   R. Hardis, J. L. Jessop, F. E. Peters and M. R. Kessler. Cure kinetics characterization and monitoring of an epoxy resin using DSC, Raman spectroscopy, and DEA. *Composites Part A: Applied Science and Manufacturing* 49 (2013), 100–108. ISSN: 1359-835X. DOI: `10.1016/j.compositesa.2013.01.021`.

[81]   F. Meyer, G. Sanz, A. Eceiza, I. Mondragon and J. Mijović. The effect of stoichiometry and thermal history during cure on structure and properties of epoxy networks. *Polymer* 36.7 (1995), 1407–1414. ISSN: 0032-3861. DOI: `10.1016/0032-3861(95)95918-Q`.

[82]   P. V. Komarov, C. Yu-Tsung, C. Shih-Ming, P. G. Khalatur and P. Reineker. Highly Cross-Linked Epoxy Resins: An Atomistic Molecular Dynamics Simulation Combined with a Mapping/Reverse Mapping Procedure. *Macromolecules* 40.22 (2007), 8104–8113. DOI: `10.1021/ma070702+`.

[83]   C. M. Sahagun, K. M. Knauer and S. E. Morgan. Molecular network development and evolution of nanoscale morphology in an epoxy-amine thermoset polymer. *Journal of Applied Polymer Science* 126.4 (2012), 1394–1405. DOI: `10.1002/app.36763`.

[84]   S. Ligot, E. Bousser, D. Cossement, J. Klemberg-Sapieha, P. Viville, P. Dubois and R. Snyders. Correlation Between Mechanical Properties and Cross-Linking Degree of Ethyl Lactate Plasma Polymer Films. *Plasma Processes and Polymers* 12.6 (2015), 508–518. DOI: `10.1002/ppap.201400162`.

[85]   C. A. Tweedie, G. Constantinides, K. E. Lehman, D. J. Brill, G. S. Blackman and K. J. Van Vliet. Enhanced Stiffness of Amorphous Polymer Surfaces under Confinement of Localized Contact Loads. *Advanced Materials* 19.18 (2007), 2540–2546. DOI: `10.1002/adma.200602846`.

[86] Y.-L. Lee, J. Pan, R. B. Hathaway and M. E. Barkey. *Fatigue Testing and Analysis - Theory and Practice*. Elsevier, (2005). Chap. 4.2 The Stress-Life (S-N) and Fatigue Limit Testing. ISBN: 978-0-7506-7719-6.

[87] S. C. Chowdhury and J. W. Gillespie. Silica–silane coupling agent interphase properties using molecular dynamics simulations. *Journal of Materials Science* 52.22 (2017), 12981–12998. ISSN: 1573-4803. DOI: `10.1007/s10853-017-1412-z`.

[88] F. Javanshour, K. Ramakrishnan, R. Layek, P. Laurikainen, A. Prapavesis, M. Kanerva, P. Kallio, A. Van Vuure and E. Sarlin. Effect of graphene oxide surface treatment on the interfacial adhesion and the tensile performance of flax epoxy composites. *Composites Part A: Applied Science and Manufacturing* 142 (2021), 106270. ISSN: 1359-835X. DOI: `10.1016/j.compositesa.2020.106270`.

[89] J. Beter, B. Schrittesser, B. Maroh, E. Sarlin, P. F. Fuchs and G. Pinter. Comparison and Impact of Different Fiber Debond Techniques on Fiber Reinforced Flexible Composites. *Polymers* 12.2 (2020). ISSN: 2073-4360. DOI: `10.3390/polym12020472`.

[90] S. Palola, F. Javanshour, S. Kolahgar Azari, V. Koutsos and E. Sarlin. One Surface Treatment, Multiple Possibilities: Broadening the Use-Potential of Para-Aramid Fibers with Mechanical Adhesion. *Polymers* 13.18 (2021). ISSN: 2073-4360. DOI: `10.3390/polym13183114`.

[91] M. R. Gude, S. G. Prolongo and A. Ureña. Effect of the epoxy/amine stoichiometry on the properties of carbon nanotube/epoxy composites. *Journal of Thermal Analysis and Calorimetry* 108.2 (2012), 717–723. ISSN: 1572-8943. DOI: `10.1007/s10973-011-2056-x`.

[92] Y. F. Li, M. Z. Xiao, Z. Wu, K. Peng, C. M. Han, W. Xiang and J. Y. Dai. Effects of epoxy/hardener stoichiometry on structures and properties of a diethanolamine-cured epoxy encapsulant. *IOP Conference Series: Materials Science and Engineering* 137.1 (2016), 012012. DOI: `10.1088/1757-899X/137/1/012012`.

[93] C. Bannister, A. Guy, R. Mihaylova, J. Orgill, S. L. Burg, A. Parnell and R. L. Thompson. The influence of ambient cure chemistry and stoichiometry on

epoxy coating surfaces. *RSC Adv.* 12.44 (2022), 28746–28754. DOI: 10.1039/D2RA05067F.

[94]   G. Groenhof. *Biomolecular Simulations: Methods and Protocols.* Totowa, NJ: Humana Press, (2013). Chap. Introduction to QM/MM Simulations, 43–66. ISBN: 978-1-62703-017-5. DOI: 10.1007/978-1-62703-017-5_3.

[95]   P.-H. Lin and R. Khare. Local Chain Dynamics and Dynamic Heterogeneity in Cross-Linked Epoxy in the Vicinity of Glass Transition. *Macromolecules* 43.15 (2010), 6505–6510. DOI: 10.1021/ma100752c.

[96]   S. Morsch, Y. Liu, P. Greensmith, S. B. Lyon and S. R. Gibbon. Molecularly controlled epoxy network nanostructures. *Polymer* 108 (2017), 146–153. ISSN: 0032-3861. DOI: 10.1016/j.polymer.2016.11.050.

[97]   T.-Y. Juang, J.-K. Liu, C.-C. Chang, S.-M. Shau, M.-H. Tsai, S. A. Dai, W.-C. Su, C.-H. Lin and R.-J. Jeng. A reactive modifier that enhances the thermal mechanical properties of epoxy resin through the formation of multiple hydrogen-bonded network. *Journal of Polymer Research* 18.5 (2011), 1169–1176. ISSN: 1572-8935. DOI: 10.1007/s10965-010-9520-3.

[98]   Y. Zhao, X. Qi, J. Ma, L. Song, Y. Yang and Q. Yang. Interface of polyimide–silica grafted with different silane coupling agents: Molecular dynamic simulation. *Journal of Applied Polymer Science* 135.4 (2018), 45725. DOI: 10.1002/app.45725.

[99]   S. A. Mian, L. C. Saha, J. Jang, L. Wang, X. Gao and S. Nagase. Density Functional Theory Study of Catechol Adhesion on Silica Surfaces. *The Journal of Physical Chemistry C* 114.48 (2010), 20793–20800. DOI: 10.1021/jp1070538.

[100]   R. Dongol, L. Wang, A. Cormack and S. Sundaram. Molecular dynamics simulation of sodium aluminosilicate glass structures and glass surface-water reactions using the reactive force field (ReaxFF). *Applied Surface Science* 439 (2018), 1103–1110. ISSN: 0169-4332. DOI: 10.1016/j.apsusc.2017.12.180.

[101]   P. A. Olsson and E. Bergvall. Atomistic investigation of functionalized polyethylene-alumina interfacial strength and tensile behaviour. *Computational Materials Science* 187 (2021), 110075. ISSN: 0927-0256. DOI: 10.1016/j.commatsci.2020.110075.

Ending quote in the dedication from Final Fantasy XIV: Endwalker.

PUBLICATIONS

PUBLICATION

I

**Identification and compensation of error sources in the microbond test
utilising a reliable high-throughput device**
P. Laurikainen, M. Kakkonen, M. von Essen, O. Tanhuanpää, P. Kallio and
E. Sarlin

Identification and compensation of error sources in the microbond test utilising a reliable high-throughput device

P. Laurikainen[a,*], M. Kakkonen[b,**], M. von Essen[b], O. Tanhuanpää[b], P. Kallio[c], E. Sarlin[a]

[a] Tampere University, Faculty of Engineering and Natural Sciences, PO Box 589, FI-33014 Tampere University, Finland
[b] Fibrobotics Oy, Finland
[c] Tampere University, Faculty of Medicine and Health Technology, PO Box 692, FI-33014 Tampere University, Finland

ARTICLE INFO

ABSTRACT

This paper addresses the issue of high scatter in microbond test results. Implementation of the test is discussed and the reliability of a state-of-the-art test system is analysed through characterisation of the critical components of the device. In total 50 filaments and around 30 droplets from each filament are measured. The results verify that much of the commonly observed scattering originates from real variation between the filaments and heterogeneous interfacial properties, while the error from the experimentation is comparably small. A stress based analytical model was noted to agree well with the experimental results.

1. Introduction

Fibre reinforced composites are known as some of the best materials for high performance applications that require excellent strength-weight characteristics. To achieve adequate properties on the product level, the interfacial properties of the fibre-resin system must be optimised. This entails proper wetting of the fibres and adequate stress transfer between the fibres and the resin, both of which are mostly controlled by the sizing applied on the fibre surface [1,2]. Development of the sizing and fibre-resin systems in general requires testing the resulting interfacial properties. A common measure for the stress transfer capabilities of the interface is the interfacial shear strength (IFSS). The IFSS is measured with single fibre methods, such as the microbond test [3] and the single fibre pull-out test [4]. However, results tend to vary significantly between different testing methods and different studies [5]. This study aims to provide further insight to the causes of the variation and to explore methods for minimizing the role of implementation related error in the total scatter.

In the microbond test, single fibre microcomposite samples are tested in a modified scheme of the pull-out method. Resin droplets are deposited and cured on single filaments and after curing loaded with microvise blades until the droplet detaches from the fibre surface. The load required for the debonding is compared with the surface area of the fibre covered by the droplet to calculate the apparent IFSS. An overview of the microbond test is presented in Fig. 1.

Several possible error sources have been identified in the microbond test. The review by Sockalingam and Nilakantan [6] lists many of the error sources discussed in literature, from limitations in the experimental setup, behaviour of the materials both during sample preparation and testing to the limitations of the data analysis methods. In the device, critical aspects to minimise the scatter include high sampling rate of load measurement, accurate determination of fibre and droplet dimensions in addition to microvise blade control [7]. The microvise blade placement is one of the most important of these error sources because it is considered a major contributor to the high scatter of results [8–11]. The sample preparation should be as reproducible as possible and ensure a reasonable range of embedded lengths, for example, to avoid fibre breakage [6]. The curing of thermoset resins or the crystallisation of thermoplastic materials must be controlled to reduce variation of the results [12,13]. Miller et al. [3,7] have also pointed out an important source of variation that is commonly overlooked: the variation of the fibre surface itself. This variation, especially between filaments, has been noted in our previous work [14] and is based on tests where multiple droplets are deposited on a single filament close to each other. This possibility was discussed in the study presenting the microbond test by Miller et al. [3], but has not been validated due to limitations in the implementation. An overview of the current understanding of microbond error sources is collected in Table 1.

Reproducible and accurate control of the microvise is crucial to control the stress distribution during the microbond test and to avoid,
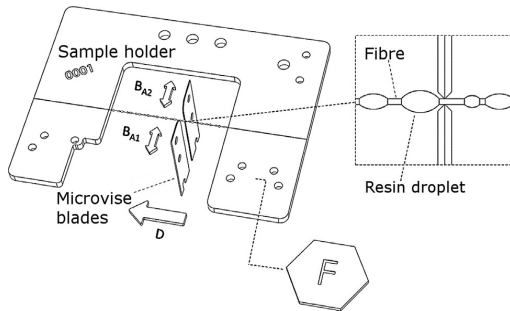

Fig. 1. An overview of the microbond test.

Table 1

Common error sources in microbond testing.

Error source	Possible negative outcomes	Ref.
Load measurement	Over-/underestimation of the measured load	[7]
Device optics	Inaccurate embedded length and/or fibre diameter	[6,7]
Microvise control	Variation of droplet loading state, high scatter in final results	[8,9,11]
Embedded area range	Changes in test behaviour, fibre breakage	[15,16,6]
Fibre surface	Variation of the results, always present	[3,7]
Resin curing	Inconsistent results, increased scatter, resin failure	[12,13]

for example, overestimating the IFSS because of compressive loads [8]. Chou et al. [8], Heilhecker et al. [9] and Nishikawa et al. [11] have explored the role of the microvise placement experimentally. Chou et al. [8] proposed an analysis to divide the force into shearing and compressive components to alleviate the issue. They also made a general observation that the gap width should be kept as small as possible. Heilhecker et al. [9] presented results from similar tests and complemented the results with finite element analysis (FEA). The FEA revealed significant difference between the maximum shear stress theory of failure and IFSS calculated from a maximum load during the test. However, no significant conclusions could be drawn due to very high scatter of the experimental results. Nishikawa et al. [11] stated that in order to analyse the true interfacial properties from microbond tests, one has to use FEA to determine the overall damage process in the test. Their FEA analysis of the microvise placement concludes that to avoid matrix cracking one should place the microvise blades as far apart as possible. However, their analysis did not include consideration for the possible increased compressive component presented by Chou et al. [8] or the tensile dominated mode of initial crack formation at the droplet meniscus [17,18]. Ash et al. [10] used FEA to observe the role of blade contact point and the stiffness of the interphase to the results of the microbond test and noted the importance of the microvise blade placement in relation to the droplet shape. Their model also predicted significant tensile stress components at the interface and an increase in debonding load, if the vise angle is increased as reported earlier by Chou et al. [8]. Given the attention it has received as an error source in microbond testing, accurate and reproducible control of the microvise placement is crucial in producing reliable microbond test data.

No standardised methodology exists for microbond testing, which has led to different research groups utilising very different equipment for the test. A common approach, also utilized by Miller et al. [3] in the study presenting the method, is to use universal testing systems with small load cells [3,19,20,12]. Reliable measurement of microscopic properties requires, however, equipment designed for the appropriate scale [6,7].

In this study, we aim to estimate the importance of the various error

sources often regarded as major limitations in the utilisation of the microbond method and to seek ways to mitigate their role in the testing. By controlled deposition and measurement of 30 to 50 droplets of variable sizes on 50 single filaments we demonstrate the variation in the properties of sized glass fibre surfaces. This will include demonstrating the importance of measuring large number of individual droplets, possible only with a high throughput device, to ensure that the measured data reliably presents the natural variation of the IFSS. We will also compare our data to an existing analytical model to further understand the behaviour of the material during the test.

2. Experimental

2.1. Device overview

The main sources of device related errors in microbond measurements are the load measurement, determination of embedded length, displacement actuator movement and the placement of the microvise blades. The FIBRObond device (Figure S1), presented here, is designed to reduce the impact of these error sources.

In the device, load is measured with a Futek (US) jr. S-beam 1 N cell. The cell is connected to a linear slide, which is connected to an absolute linear encoder manufactured by Numerik Jena (Germany). The load measurement method differs from the typical setup presented in microdroplet test publications. The main differences are the horizontal loading direction and the linear slide, connecting the sample to the load cell, intended to reduce load components that are not aligned to the horizontal axis direction. The encoder connected to the slide is used for determining elastic deformation of the load cell during loading. The components of the load measurement are presented in Fig. 2. National instruments (US) NI-6003 data acquisition (DAQ) device is used to record the signal with a 1 kHz frequency. During the measurement, the droplet is displaced using R35 microtome blades manufactured by Feather (Japan). Both blades can be moved separately to adjust the blade placement and the blade gap using piezo actuators manufactured by SmarAct (Germany). The fine resolution (5 nm) of the actuators, with the accurate imaging through the device optics enables placing the blades in contact with fibre without damaging the fibre itself. This enables reproducible control of the blade gap. Alignment of the blades is controlled using shimmers and can be monitored via the device optics. During the assembly, the alignment of the blade centre lines is controlled with 2 μm tolerance and checked regularly. This is crucial to minimize error caused by blades in the measurements as even very small misalignment causes bending of the fibre and uneven loading of the droplet during a test. The movement along the fibre is controlled with a M-111.1DG1 DC motor (see Fig. 3) operated with a C-863 controller manufactured by Physik Instrumente (Germany). During the testing the, speed is 0.008 mm/s.

The optics of the device comprise a tube microscope with a 20x long working distance objective and a 2x extender tube manufactured by Qioptiq (United Kingdom). The view is captured with an IDS (Germany) UI-3370SE monochromatic camera. The field of view was calibrated using a microscope micrometer manufactured by Helmut Hund (Germany) with a 1 mm measuring line with 100 divisions. Scale factor for this optic setup is 0.137 μm/px (280.576 μm × 280.576 μm field of view).

To analyse the embedded length of a droplet from the captured view, a computer vision algorithm was developed. Snapshots of the algorithm steps are presented in Figure S2. The algorithm utilises threshold conversion of the image to binary, filling of enclosed white contours and cropping black pixels from pixel columns that have less black pixels than a pre-set threshold defined by a user. A smallest confining rectangle is fitted over each droplet and the length of the box is measured. This automated, algorithm-based method is hypothesized to give more consistent measurements than human operation.
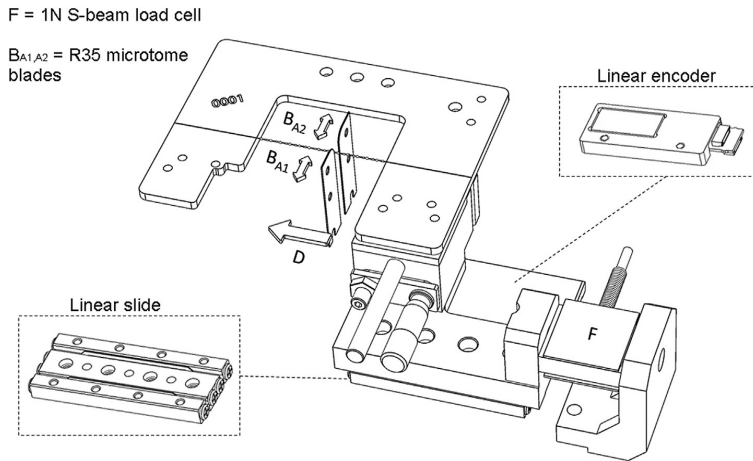
F = 1N S-beam load cell

$B_{A1,A2}$ = R35 microtome blades

Linear encoder

Linear slide

Fig. 2. The critical components of the load measurement implementation in the device.

F_{ref}

Stiff bar
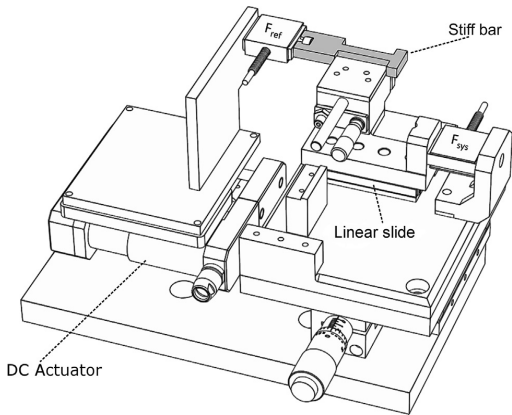
F_{sys}

Linear slide

DC Actuator

Fig. 3. Setup for calibrating the force measurement.

2.2. Validation of the system

The performance of the critical components of the device – the load measurement, total displacement and the device optics – were tested to analyse the total error from the measurement system and validate the accuracy of the device in microscale testing. The load cell calibration provided by the manufacturer was validated using free weights. In order to calibrate the force measurement in the system, a special setup for the calibration was developed. The calibration setup comprises the system load cell (F_{sys}) connected to a reference cell (F_{ref}) via a stiff bar shown in Fig. 3. The reference cell is the same model and from the same manufacturer as the system load cell. Calibration was conducted with five force levels, repeating five times for each loading level. The average of these five measurements was calculated for both force cells

and the ratio between the averages were used to determine a calibration factor for the force. The total displacement during a test results from the actuator movement and the elastic deformations of the load cell, the sample holder and the filament. The procedure and outcomes of the determination of displacement accuracy are included in the supplementary data.

Accuracy of the computer vision algorithm compared to human operators was studied with a group of five operators. This group contained both researchers familiar with microbond testing and researchers outside of the field. The operators measured dimensions of a predetermined series of droplets with a high-end optical microscope and with the vision system of the FIBRObond device. The images from the FIBRObond device were analysed both manually, using image analysis software and with the computer vision algorithm. Parameters of the microscope and illumination were kept constant for all operators. The affecting factors should therefore be the operator, their opinion on how the droplet size should be determined and the capabilities of the method itself.

2.3. Materials

An average of 40 droplets were deposited over a length span of 10–12 mm on a 15 cm long filament. These filaments were selected from a roving of HiPer-tex W 2020 glass fibre, kindly provided by Ahlstrom-Munksjö Glassfibre Oy. The filaments were taken in batches of 10 from controlled length regions of the roving, approximately 150 mm apart. The fibres were measured within the intended storage lifetime, to ensure the viability of the sizing on the fibres. Table 2 shows the properties of the W 2020 fibre along with the average diameter of the filaments used in this study.

Araldite LY 5052 epoxy resin was used for the droplets. The resin was selected due to its high stiffness and predictable curing allowing us to reduce the role of resin variation in the results. The time window for droplet deposition was selected from 15 min to 45 min after mixing. The selection was based on the pot life given in the resin datasheet and

Table 2
Material properties.

Material	E_A/E_m [GPa]	CTE (α) [$\times 10^{-6}$ 1/K]	Fibre $\varnothing$ [µm]	Poisson's ratio
HiPer-tex W 2020 [21]	86	4.1	18.6 ± 1.3	0.17 [22]
Araldite LY 5052 [23]	3.35	71.0	–	0.35

observations made during the sample preparation. In the selected time-frame, the behaviour of the resin batch did not change noticeably. The cure cycle for the deposited droplets was also selected based on the datasheet: one day at room temperature followed by eight hours at 80 °C. Bulk resin, cured with this cure cycle would have a glass transition temperature around 120 °C. The cure cycle is therefore assumed to result in a reasonably high degree of cure even for a microscale resin batch. The resin properties needed for analysis are also collected to Table 2.

A total of 50 filaments were measured, adding up to approximately 1500 individual droplet measurements. The large dataset enables a thorough analysis of the variation of the fibre surface and other possible sources of deviation. It also demonstrates the high-throughput capabilities of the equipment in use. The droplets were prepared with embedded lengths ranging approximately from 50 to 180 µm to observe the embedded area dependency of the debonding load.

3. Results

3.1. Device validation

The operation of the load cell was validated both as standalone and in the system to ensure the accuracy of the load measurement during the microbond tests. Outside of the system the voltage to load conversion of the cell follows the coefficient of 0.09815 N/V. In the measurement system, the force cell also measures some minor frictional components causing a slight difference between the loads F_{ref} and F_{sys} in the calibration setup. The coefficient is therefore slightly lower, 0.09758 N/V. The results of the calibration measurements are presented in Fig. 4. The in-system coefficient was used for voltage-load conversion and the standard error of regression for the coefficient was included into the error analysis. As the load cell operates with a high sampling rate and very low forces, it is unsurprising that the load measurement has notable noise in the data. During the analysis, this noise was filtered with a 50 point moving average, which was enough to remove the noise almost completely. However, this also causes some level of uncertainty to the measured debonding load. This uncertainty is, however, several orders of magnitude smaller than the error of the voltage to load conversion and deemed negligible to the total error.

The accuracy and reproducibility of the embedded length measurement are critical factors in microbond testing. The three methods explained in Section 2.2 for determining the embedded lengths were compared for five operators. The standard deviations (σ) were calculated for each droplet based on the results from each operator. The

Table 3
Statistical comparison of the embedded lengths measured by 5 operators with 3 different methods.

Method	# of droplets	max. σ [µm]	min. σ [µm]	ave. σ [µm]	$\sigma_{\bar{x}}$ [µm]
Computer vision	64	5.38	0.85	1.75	0.219
Image analysis	76	4.11	0.85	1.84	0.211
Microscope	77	5.37	0.53	2.16	0.246

standard error ($\sigma_{\bar{x}}$) of each method is estimated from the average standard deviation for the method and the number of analysed droplets. An overview of the results is provided in Table 3. Overall, the accuracies of the three methods are similar and the variation between operators small. However, for extremely small droplets, e.g. 30–40 µm or with occasional errors in manual operation, the variation can be significantly higher than the average. The largest contributor to the deviation was the operators' interpretation of the two ends of the droplet.

3.2. Microbond measurements

The IFSS of the HiPer-tex W 2020 glass fibre – Araldite LY 5052 microcomposites was determined by measuring the load required to debond a total of 1527 microdroplets with varying embedded lengths. This sampling represents the glass fibre roving from a length of approximately 1.3 m. Droplets deposited into close proximity of each other on the same filaments exhibit very similar interfacial properties. The strain rate in each test is also similar and has no significant effect on the results. Together these factors – coupled with accurate control of the microvise blade gap to the fibre surface – enable the measurement of data with very low scatter within a single data series. Results for filaments numbered # 4, # 22 and # 37 are presented Fig. 5 as examples. These results were selected to show the quality of the data and represent their respective roving spans (i.e. 0 to 15 cm for filament # 4). As can be observed from Fig. 5, the results for droplets deposited on a single filament exhibit a linear behaviour. Significantly more scatter emerges when the variation between different filaments is included. This is already seen in Fig. 5, but is even more clear when all the measured data is plotted together (see Fig. 7). Calculating the apparent IFSS for individual droplets of the full dataset results in IFSS of 31.71 ± 6.70 MPa. Using linear regression to determine the IFSS from the slope of the force vs. embedded area from the full dataset as done by Cai et al. [24], results in an average IFSS of 45.77 ± 0.50 MPa. Note that
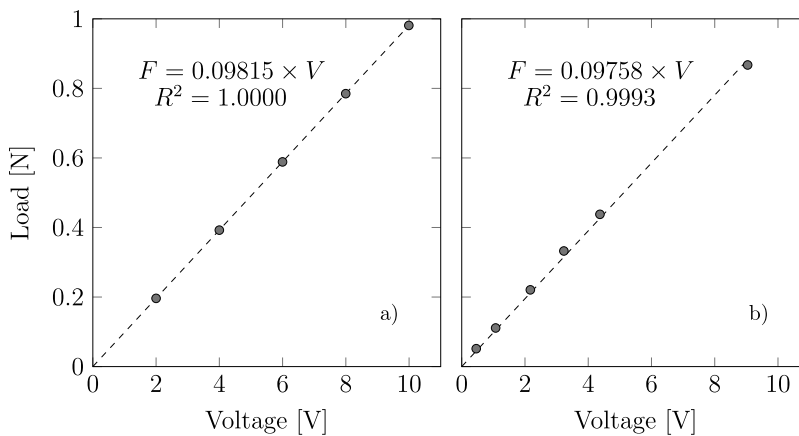

Fig. 4. Voltage to load conversion calibration, a) standalone, b) in system.
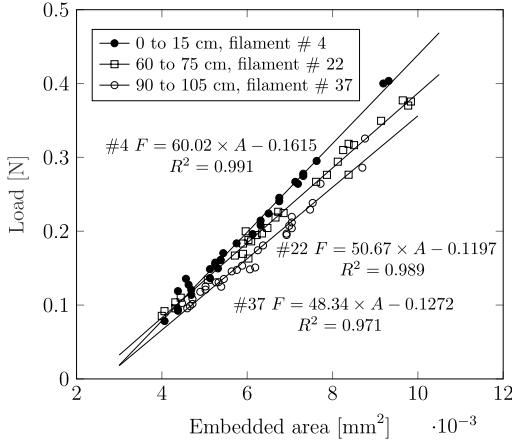
Fig. 5. Single filament data series examples from three different sections of roving.

in this case the error value $\pm$ 0.50 MPa is the standard error of the slope from the linear regression. Linear regression for the 50 filaments separately, taking the average slope as IFSS, results in 52.76 $\pm$ 9.79 MPa. The average IFSS also varies along the length of the roving. The average IFSS for 10 parallel samples from a single roving section varies between 57.32 $\pm$ 5.36 MPa and 49.72 $\pm$ 9.75 MPa. It is clear that the apparent IFSS, without further analysis, is not a suitable measure for the behaviour of the interface.

4. Discussion

Most methods of analysis for microbond results do not consider the role of displacement. However, to improve the applicability of the method from comparative studies, the incorporation of more in-depths analysis such as FEA is needed and the validation of FEA requires accurate force-displacement information from the test. Similarly to FEA, the displacement is an important parameter in analysis methods which consider the crack propagation, such as the analysis proposed by Lilholt and Sørensen [25]. Many aspects of the displacement error, such as the elastic deformation of the load cell (see Figure S3), can be fairly easily compensated or even ignored. The strain rate however, needs to be controlled and accurate for reliable testing and the performance of the movement actuator is crucial, as can be seen in Figure S4.

The error in the estimation of the embedded area can cause significant scattering of microbond results. Most importantly the estimation should be consistent. Consistent over- or under-evaluation of the embedded lengths can still result in a low scatter of the data. This however, shifts the data accordingly and makes the apparent IFSS from individual droplets very unreliable. The significance of operator and method variation on the results was examined by comparing the results of sample # 24, which was used in embedded area analysis by different operators. The variation of the computer vision results between the operators and the variation between the methods for a single, representative operator are presented in Fig. 6. The reproducibility of the computer vision is slightly better compared to the other methods. The computer vision and optical microscope result in very similar slopes, with some variation in the axis intercept, whereas the results from manual image analysis differed noticeably. For one operator however, the slopes were almost identical for all three methods and the results of computer vision and microscope were close to identical. The most important outcome of the analysis are the similar slopes from microscope and computer vision methods. Therefore, there is little difference in the slope-based IFSS analysis for the two methods.

The level of uncertainty in the microbond measurements was determined by calculating the sum of errors from all relevant error sources. The formulation is presented in the supplementary data. The error in IFSS from the experimentation was determined as 3.00 $\pm$ 0.70 MPa. The uncertainty of embedded length was identified as the most important contributor and the result can be improved significantly if the operators' influence can be further mitigated. Even with some uncertainty in the embedded area determination, the total error from experimentation is significantly lower than the natural variation of the IFSS, which for our results is in the range of 7 to 10 MPa.

Modern analysis of microbond results utilizes usually either FEA or analytical models to better understand the test system and the results in terms of actual material behaviour. The apparent IFSS (τ_{app}) is, as discussed in Section 3.2, a poor measure of the true interfacial performance as it fails to account for important factors such as thermal residual stresses. To better understand the results, the data is fitted to the stress based model presented by Zhandarov and Mäder [22]. The model includes the Nayfeh shear lag parameter β presented as

$$\beta^2 = \frac{2}{r_f^2 E_A E_m}\left[\frac{E_A V_f + E_m V_m}{\frac{V_m}{4G_A} + \frac{1}{2G_m}\left(\frac{1}{V_m}ln\frac{1}{V_f} - 1 - \frac{V_f}{2}\right)}\right] \tag{1}$$

where E_A, E_m, G_A and G_m are the tensile and shear modulus of the fibre and the matrix, respectively. V_f and V_m are the volume fractions of the two components and r_f is the fibre radius. To calculate the volume fractions, the resin droplets are approximated using an elliptical shape with a length equal to l_{emb} and a maximum thickness equal to the droplet maximum thickness.

The aforementioned formulation for the shear lag parameter resulted in negative β^2 values for some of the smallest droplets. This is a known feature of the Nayfeh parameter when the fibre volume fraction is higher than a certain material dependent critical value [22]. To still include these droplets into the analysis, the Cox shear lag parameter is used to analyse these droplets [16] despite its limitations [22] as it is generally well behaved for higher fibre volume fractions [16,22,26].

$$\beta^2 = \frac{2G_m}{E_A ln\left(\frac{1}{V_f}\right)} \tag{2}$$

The shear lag parameter can be used to estimate the thermal residual stresses τ_T with

$$\tau_T = \frac{\beta r_f E_A}{2}(\alpha_A - \alpha_m)\Delta T \tag{3}$$

where α_A and α_m are the fibre and resin thermal expansion coefficients (Table 2) and ΔT is the temperature difference from stress free temperature and testing conditions. In this case it is taken as the difference between the curing temperature (80°C) and approximate lab temperature of 23 °C.

Zhandarov and Mäder [22] present two cases of debonding event. The first case is a catastrophic crack propagation through the embedded length where the friction at the interface does not contribute to the measured load. The second is a stable crack propagation case where the interfacial friction needs to be considered a part of the loading case. These two analysis cases are determined by the conditions $\beta l_{emb} < ln(u + \sqrt{(u^2 + 1)})$ and $\beta l_{emb} \geqslant ln(u + \sqrt{(u^2 + 1)})$, where u is a parameter defined as

$$u = \frac{\sqrt{\tau_T^2 + 4\tau_f(\tau_d - \tau_f)} - \tau_T}{2\tau_f} \tag{4}$$

where τ_f and τ_d are the interfacial friction and interfacial shear strengths, respectively. We have evaluated the interfacial friction based on the embedded area and the load level after the debonding event [27]. In some measurements, however, no such load was detected after
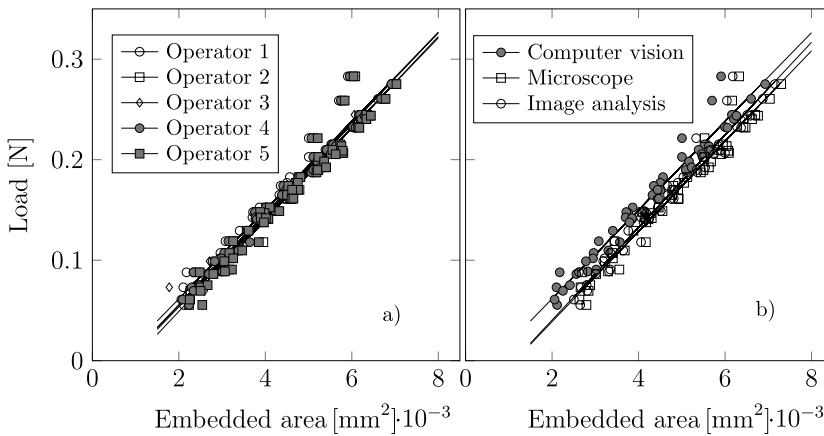
Fig. 6. Filament # 24 analysed with embedded areas measured with a) computer vision by all five operators, b) all three methods by operator 1.

Table 4
Distribution of the result to the three analysis cases defined in

Case	# of droplets	Explanation of the case
1: $\tau_f \approx 0$	277	No friction force detected
2: $\beta l_{emb} < ln(u + \sqrt{(u^2 + 1)})$	1146	Catastrophic debonding [22]
3: $\beta l_{emb} \geqslant ln(u + \sqrt{(u^2 + 1)})$	104	Stable crack propagation [22]

debonding and these have been included in the analysis as a separate third case. The result of the linear regression based analysis presented in Section 3.2 was used for each filament dataset as the interfacial shear stress τ_d. Table 4 presents the distribution of the results into these three analysis cases. The first two cases in Table 4 are analogous as the analytical formulations for the frictionless case and the catastrophic debonding case are the same. Only the third case takes the friction forces into account in the analysis. The model used to predict the maximum load for each droplet has the form [22]:

$$F_{max}(l_{emb}) = \begin{cases} \frac{2\pi r_f}{\beta} \left[\tau_d tanh(\beta l_{emb}) \\ -\tau_T tanh(\beta l_{emb}) tanh(\frac{\beta l_{emb}}{2}) \right], & \text{for } 1, 2 \\ \frac{2\pi r_f}{\beta} \left[\tau_d \frac{u}{\sqrt{(u^2+1)}} - \tau_T \left(1 - \frac{1}{\sqrt{(u^2+1)}}\right) \\ + \tau_f \left[\beta l_{emb} - ln(u + \sqrt{(u^2 + 1)})\right]\right], & \text{for } 3 \end{cases}$$

(5)

The output from the model presented in Eq. (5) is the expected maximum force for a microbond measurement of that droplet. Fig. 7 presents the full measured dataset and the model predictions for comparison. As can be seen from the figure, the model predicts the experimental behaviour very well. The fit is poorer for the droplets analysed with the Cox shear lag parameter, visible as the series of higher loads at low embedded areas. The axis offset results mostly from the thermal stresses and is accurately predicted by the model.

Based on this analysis, the role of the interfacial friction is overall minor. Only a small percentage of the droplets fulfil the condition for stable crack propagation and, according to the model, require consideration for the friction component. In Fig. 8, the relative portion of the force associated with interfacial friction is plotted against the corresponding fibre volume fraction. The results indicate that even relatively large frictional forces can be measured without requiring consideration for them in the final analysis. However, the Cox shear lag parameter does not appear to function properly for this part of the

analysis, as those droplets are grouped into case 2. At least some, if not all, would be expected to fulfil the case 3 condition based on Fig. 8. The role of interfacial friction in microbond testing requires further experimental study to be fully understood.

For further comparison, the model presented in Eq. (5) was fitted to the measured maximum load values to estimate the IFSS (τ_d). These results are presented in Fig. 9. Based on the results, we can detect a lower limit for the embedded length after which the experimental and analytical results coincide well. It should be noted that these smallest droplets are also quite unreliable to measure and were included more to test the limits of the device. Limiting the measured droplets to embedded lengths around 55 μm and above would significantly mitigate any issues. This lower limit depends on the fibre dimensions – and to a lesser extent on the fibre-resin combination [22] – and is therefore difficult to predict before measurement. An overview of the IFSS analysed with the methods presented in this paper is shown in Table 5. For the analytical model, limiting the analysis only to droplets above 55 μm in embedded length gives an average IFSS of 47.85 ± 7.83 MPa. The interfacial properties vary along the roving length, with the highest values measured from the start of the roving.

The validity of the maximum load based apparent IFSS as a measure for interfacial strength has been under much discussion, with some publications stating it as not valid, e.g. [15,28]. This is true if the analysis only considers the maximum load from a single measurement, but simply measuring a range and estimating the slope can give a good approximation of true interfacial properties without needing more complex methods of analysis. Many studies, utilise the more traditional pull-out scheme – where the sample behaviour during the test is vastly different – or microbond with large droplets in the range of 100–500 μm or even larger. Based on our experience, when measuring smaller droplets (e.g. from 50–200 μm as in this paper) the test usually follows the optimal behaviour of catastrophic debonding, as is also predicted by the stress based analytical model. The behaviour of the analytical model for other fibre-resin systems needs to be explored in future work. For many resin systems, the final properties of a microscale sample are much less predictable and finding suitable parameters for the model may prove more difficult. On the other hand, if the model performs equally well, fitting to the model could help predict the properties in cases where direct measurements are difficult or impossible.

The important outcome is that the average IFSS for the droplets on a single filament can be quickly evaluated from the slope seen in Fig. 5 with reasonable accuracy. The fibre-resin system is then characterised by measuring several filament samples. This approach enables simple
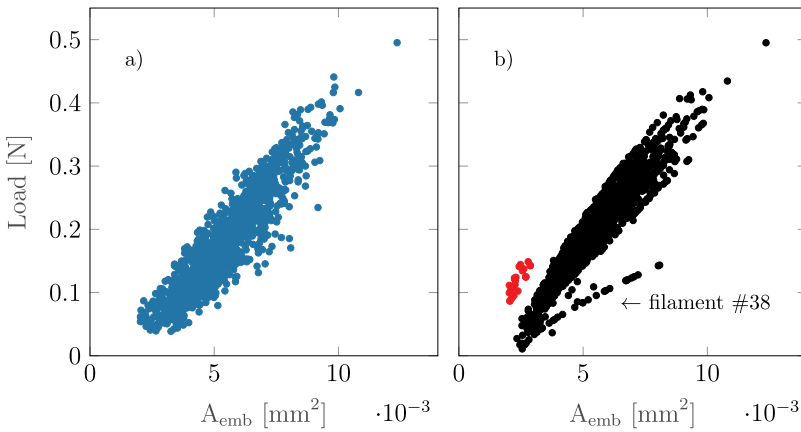
Fig. 7. Load vs. embedded area for all measured droplets, a) Measured data, b) Data based on the model. The weaker dataset from filament # 38 is clearly visible in the model data. Data points analysed with the Cox shear lag parameter are indicated in red. (For interpretation of the references to color in this figure legend, the reader is referred to the web version of this article.)
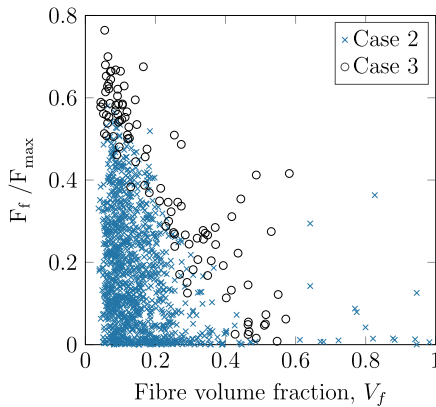

Fig. 8. Role of interfacial friction based on the stress based analysis, separated into cases according to Table 4. (For interpretation of the references to color in this figure legend, the reader is referred to the web version of this article.)
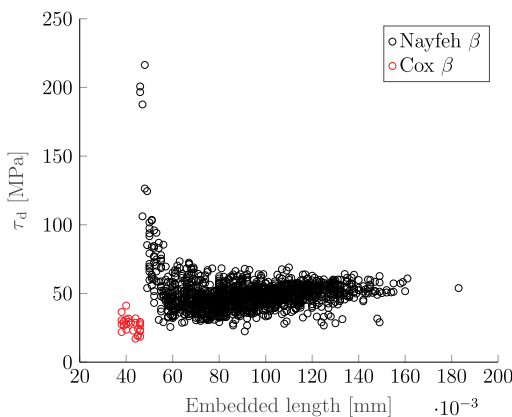

Fig. 9. IFSS (τ_d) analysed according to Eq. (5) vs. droplet embedded length. (For interpretation of the references to color in this figure legend, the reader is referred to the web version of this article.)

Table 5
Overview of the Araldite LY 5052 - HiPer-tex W 2020 IFSS with various analysis methods.

Roving section [cm]	Individual droplets, τ_{app}	Linear regression, all data [24]	Linear regression, filaments	Stress based model [22]
0–15	33.62 ± 6.48	–	57.32 ± 5.36	52.44 ± 13.63
30–45	31.87 ± 7.12	–	53.77 ± 5.00	48.84 ± 16.55
60–75	31.47 ± 5.63	–	51.95 ± 5.32	47.81 ± 11.41
90–105	30.95 ± 7.18	–	49.72 ± 9.75	47.74 ± 10.68
120–135	29.95 ± 6.60	–	50.01 ± 6.28	45.47 ± 10.62
Average	31.71 ± 6.70	45.78 ± 0.50	52.76 ± 9.79	48.68 ± 12.84

and reliable analysis of the interfacial properties and provides valuable input for a more thorough analysis of the micromechanics of the system.

The preparation of suitable samples can be challenging. One possible sample preparation scheme has been proposed by Hou and Sun [29], who presented a polymer solution based method for samples with multiple droplets on each filament. Sample preparation is also important in terms of the final droplet shape. Inconsistent sample behaviour can therefore be expected to increase the scatter of the experimental results and make the direct estimation of the IFSS from the experimental results difficult. However, the analytic model can take the shape of the droplet into account and fitting the data to the model could therefore lead to more reliable analysis. In this study, however, the sample preparation was very predictable and the droplet thickness corresponds similarly to the embedded length in all samples.

5. Conclusions

The high scatter of microbond results can be mitigated by minimizing the device related scatter and by measuring multiple droplets with a suitably wide range of droplet sizes from a single filament. The embedded length range should favour immediate debonding so that the maximum force corresponds linearly to the embedded area. However, measuring too small droplets can also hinder the analysis and the lower limit should be identified before, or early during, the measurement. Working on this scale requires accurate equipment and the sample preparation needs to have suitable control over the embedded length distribution. Based on our results, 30 droplets for each filament is sufficient to analyse the interfacial properties. A suitably large number of filaments should be measured if one expects to reliably characterise the properties of the fibre-resin combination. Our results show variation of

the interfacial properties both between the individual filaments of the roving and along the length of the roving, which should be considered when selecting the samples. Stress based analysis is found to agree well with the experimental results and can be used to evaluate for example the contribution of thermal stresses to the measured results. The role of the microvise blade gap can be largely ignored by measuring with the blades touching, but not compressing, the fibre. By measuring with this methodology we characterised the average IFSS of W2020 glass fibres with Araldite LY 5052 epoxy resin as 52.76 ± 6.85 MPa, but in small sections of the roving the IFSS can be significantly lower, in the range of 20–25 MPa.

CRediT authorship contribution statement

P. Laurikainen: Conceptualization, Formal analysis, Investigation, Data curation, Writing - original draft, Writing - review & editing, Visualization. **M. Kakkonen:** Conceptualization, Methodology, Software, Investigation, Resources, Writing - original draft, Writing - review & editing. **M. von Essen:** Methodology, Software, Writing - review & editing. **O. Tanhuanpää:** Conceptualization, Methodology, Resources, Writing - review & editing, Visualization. **P. Kallio:** Conceptualization, Resources, Writing - review & editing, Supervision. **E. Sarlin:** Conceptualization, Resources, Writing - review & editing, Supervision.

Declaration of Competing Interest

The authors declare that they have no known competing financial interests or personal relationships that could have appeared to influence the work reported in this paper.

Acknowledgements

Appendix A. Supplementary material

Supplementary data associated with this article can be found, in the online version, at https://doi.org/10.1016/j.compositesa.2020. 105988.

References

[1] Dey M, Deitzel J, Gillespie J, Schweiger S. Influence of sizing formulations on glass/ epoxy interphase properties. Compos Part A: Appl Sci Manuf 2014;63:59–67. https://doi.org/10.1016/j.compositesa.2014.04.006.

[2] Teklal F, Djebbar A, Allaoui S, Hivet G, Joliff Y, Kacimi B. A review of analytical models to describe pull-out behavior – fiber/matrix adhesion. Compos Struct 2018;201:791–815. https://doi.org/10.1016/j.compstruct.2018.06.091.

[3] Miller B, Muri P, Rebenfeld L. A microbond method for determination of the shear strength of a fiber/resin interface. Compos Sci Technol 1987;28:17–32. https://doi.org/10.1016/0266-3538(87)90059-5.

[4] Penn LS, Bowler ER. A new approach to surface energy characterization for adhesive performance prediction. Surf Interface Anal 1981;3:161–4. https://doi.org/10.1002/sia.740030405.

[5] Pitkethly M, Favre J, Gaur U, Jakubowski J, Mudrich S, Caldwell D, et al. A round-robin programme on interfacial test methods, Compos Sci Technol 1993;48:205–14. doi: 10.1016/0266-3538(93)90138-7, Special Issue Microphenomena in Advanced Composites.

[6] Sockalingam S, Nilakantan G. Fiber-Matrix Interface Characterization through the Microbond Test. Int J Aeronaut Space Sci 2012;13:282–95. https://doi.org/10.5139/IJASS.2012.13.3.282.

[7] Miller B, Gaur U, Hirt DE. Measurement and mechanical aspects of the microbond pull-out technique for obtaining fiber/resin interfacial shear strength. Compos Sci Technol 1991;42:207–19. https://doi.org/10.1016/0266-3538(91)90018-K special Issue Interfaces in Composites.

[8] Chou C, Gaur U, Miller B. The effect of microvise gap width on microbond pull-out test results. Compos Sci Technol 1994;51:111–6. https://doi.org/10.1016/0266-3538(94)90161-9.

[9] Heilhecker H, Cross W, Pentland R, Griswold C, Kellar JJ, Kjerengtroen L. The vice angle in the microbond test. J Mater Sci Lett 2000;19:2145–7. https://doi.org/10.1023/A:1026787012473.

[10] Ash J, Cross S, Svalstad D, Kellar J, Kjerengtroen L. Finite element evaluation of the microbond test: meniscus effect, interphase region, and vise angle. Compos Sci Technol 2003;63:641–51. https://doi.org/10.1016/S0266-3538(02)00256-7.

[11] Nishikawa M, Okabe T, Hemmi K, Takeda N. Micromechanical modeling of the microbond test to quantify the interfacial properties of fiber-reinforced composites. Int J Solids Struct 2008;45:4098–113. https://doi.org/10.1016/j.ijsolstr.2008.02.021.

[12] Biro DA, McLean P, Deslandes Y. Application of the microbond technique: Characterization of carbon fiber-epoxy interfaces. Polym Eng Sci 1991;31:1250–6. https://doi.org/10.1002/pen.760311704.

[13] Zinck P, Wagner H, Salmon L, Gerard J. Are microcomposites realistic models of the fibre/matrix interface? ii. physico-chemical approach. Polymer 2001;42:6641–50.

[14] von Essen M, Sarlin E, Tanhuanpää O, Kakkonen M, Laurikainen P, Hoikkanen M, et al. Automated high-throughput microbond tester for interfacial shear strength studies. In: Proceedings of the SAMPE Conference 2017 Stuttgart, SAMPE Europe; 2017.

[15] Zinck P, Wagner H, Salmon L, Gerard J. Are microcomposites realistic models of the fibre/matrix interface? i. micromechanical modelling. Polymer 2001;42:5401–13. https://doi.org/10.1016/S0032-3861(00)00870-3.

[16] Scheer RJ, Nairn JA. A comparison of several fracture mechanics methods for measuring interfacial toughness with microbond tests. J Adhesion 1995;53:45–68. https://doi.org/10.1080/00218469508014371.

[17] Piggott M. A new model for interface failure in fibre-reinforced polymers. Compos Sci Technol 1995;55:269–76. https://doi.org/10.1016/0266-3538(95)00103-4.

[18] Zhandarov S, Gorbatkina Y, Mäder E. Adhesional pressure as a criterion for interfacial failure in fibrous microcomposites and its determination using a microbond test. Compos Sci Technol 2006;66:2610–28. https://doi.org/10.1016/j.compscitech.2006.03.023.

[19] Craven J, Cripps R, Viney C. Evaluating the silk/epoxy interface by means of the microbond test. Compos Part A: Appl Sci Manuf 2000;31:653–60. https://doi.org/10.1016/S1359-835X(00)00042-7.

[20] Day R, Rodrigez J. Investigation of the micromechanics of the microbond test. Compos Sci Technol 1998;58:907–14. https://doi.org/10.1016/S0266-3538(97)00197-8.

[21] HiPer-tex™W 2020 Rovings datasheet, 3B-the fiberglass company; 2018.

[22] Zhandarov S, Mäder E. Peak force as function of the embedded length in pull-out and microbond tests: effect of specimen geometry. J Adhes Sci Technol 2005;19:817–55. https://doi.org/10.1163/1568561054929937.

[23] Araldite LY 5052 Resin/ Aradur 5052 Cold curing epoxy systems, Huntsman Advanced Materials Inc.; 2012.

[24] Cai G, Wada M, Ohsawa I, Kitaoka S, Takahashi J. Interfacial adhesion of recycled carbon fibers to polypropylene resin: Effect of superheated steam on the surface chemical state of carbon fiber. Composi Part A: Appli Sci Manuf 2019;120:33–40. https://doi.org/10.1016/j.compositesa.2019.02.020.

[25] Lilholt H, Sørensen BF. Interfaces between a fibre and its matrix. IOP Conf Ser: Mater Sci Eng 2017;219:012030. https://doi.org/10.1088/1757-899x/219/1/012030.

[26] Nairn JA. On the use of shear-lag methods for analysis of stress transfer in unidirectional composites. Mech Mater 1997;26:63–80. https://doi.org/10.1016/S0167-6636(97)00023-9.

[27] Zhandarov S, Mäder E, Scheffler C, Kalinka G, Poitzsch C, Fliescher S. Investigation of interfacial strength parameters in polymer matrix composites: Compatibility and reproducibility. Adv Ind Eng Polym Res 2018;1:82–92. https://doi.org/10.1016/j.aiepr.2018.06.002.

[28] Zhandarov S, Mäder E. Determining the interfacial toughness from force–displacement curves in the pull-out and microbond tests using the alternative method. Int J Adhes Adhes 2016;65:11–8. https://doi.org/10.1016/j.ijadhadh.2015.10.020.

[29] Hou Y, Sun T. An improved method to make the microdroplet single fiber composite specimen for determining the interfacial shear strength. J Mater Sci 2012;47:4775–8. https://doi.org/10.1007/s10853-012-6317-2.

PUBLICATION

II

Exploring the role of fibre sizing to the fatigue of glass fibre composites using a novel, reliable micro-fatigue test

P. Laurikainen, R. Dsouza, M. Kakkonen, M. Kanerva and E. Sarlin

Exploring the role of fibre sizing to the fatigue of glass fibre composites using a novel, reliable micro-fatigue test

P. Laurikainen [a],*, R. Dsouza [a], M. Kakkonen [b], M. Kanerva [a], E. Sarlin [a]

[a] *Tampere University, Faculty of Engineering and Natural Sciences, PO Box 589, FI-33014 Tampere University, Finland*
[b] *Fibrobotics Oy, Finland*

ARTICLE INFO

ABSTRACT

Single fibre micro-composite tests are among the most reliable methods for characterising the fibre–matrix interphase. To improve their versatility, this study utilises a well-characterised microbond setup in a cyclic loading case to create a so-called micro-fatigue test. The surface of the fibres is controlled to create two distinctive interphase types: a clean glass fibre surface, and a model sizing. The sizing improved the average interfacial performance in all tested cases, but the role of the sizing was most prominent in the fatigue lifetime of the microdroplet samples. Finite element analysis was used to evaluate the strain-rate dependency and heating related to the plastic deformation of the microdroplet samples in cyclic loading and predicted a well behaving experimental setup. The method offers a promising pathway for further studies on interfacial fatigue and the role of sizing in it.

1. Introduction

Fibre-reinforced composites find a variety of applications in the automotive and aerospace industries due to their high strength-to-weight ratio. However, to get the most out of the composite material the fibre–matrix interface cannot be ignored, as the stress transfer from the matrix to the fibres is crucial in order to reach the full potential of the material. In glass fibre composites, this stress transfer is ensured with the use of specific surface treatments on the fibre surface, the most common by far being a thin coating known as sizing. Commercial sizing comprises both components for improving interfacial performance – such as coupling agent and film former – and processing aids that improve wetting, protect the fibre and otherwise ease the handling during further process steps [1]. When the fibres are coated with resin, the sizing mixes partially with the resin, creating the interphase: a region distinctive from both fibre and matrix and of significant importance to the overall composite performance. Thus, experimental approaches for measuring the properties of this interphase region have seen considerable research effort in the past decades and resulted in fairly well established quasi-static micro-composite experiments, such as the pull out and microbond tests [2]. These tests are frequently used to determine the local interfacial parameters such as shear strength and fracture toughness of the interface.

Many – if not most – composite products are utilised in applications that result in fatigue due to vibrations, varying wind loads or even impacts, and the performance of the interphase in such applications is almost impossible to predict from quasi static experiments. Unstable crack propagation is difficult to measure using these quasi-static destructive tests and detailed analysis of dissipative and non-dissipative energy contributions is not possible. These factors are only observable through cyclic loading tests and could provide valuable information on the nature of the interphase in terms of, for example, viscoelasticity. A successful microcomposite fatigue test would also enable the much needed opportunity to study the fatigue failure process at the interphase without the influences of fibre breaks and fibre-fibre interactions, which contribute significantly in macroscale fatigue [3].

Currently, only a few examples for this type of test are found in literature. Combining the complexity of microcomposite testing to the already complex case of cyclic loading presents a significant challenge. As with quasi-static microcomposite testing, the underlying phenomena and the limitations of the device must be addressed to ensure the measured property has any physical meaning to actual composite performance.

Mai et al. [4] have tested cyclic loading in microscale based on the pull out scheme. The test uses a piezoelectronics-based transducer to achieve cyclic loading with position and force recording. The tests themselves comprise frequency sweeps to determine the phase angle and loss factor (tan δ). In a sense, the test in this case could be compared to a microcomposite dynamic mechanical analysis (DMA). Mäder et al. [5] and Brodowsky et al. [6] have later used the same setup to

perform a type of fatigue testing with altering strain amplitude and frequency and reported significant improvement in fatigue lifetime for high stress loading when their model sizing was used to improve the apparent interfacial adhesion. They also noted that the improvement was far lesser for low stress dynamic loading [5]. The embedded length ranges for the tests in question were between 100–800 μm with the displacement amplitudes varying up to two microns [6]. No explicit description on number of tested samples is given, but the presented data focuses on single measurements per sample type.

Shin et al. [7] have used a microbond-based cyclic loading scheme to explore the effects of dopamine as a compatibiliser – or coupling agent – between glass fibres and epoxy. The test utilised relatively high levels of pre-stress followed by cyclic loading of the pre-stressed state. The results showed minor improvement in fatigue behaviour under cyclic loading with the addition of dopamine. However, the testing setup was based on a universal testing system and both the number of tested samples and the number of cycles in the test were very low.

Several theories exist on how the sizing applied on fibre surface helps create the improved interfacial contact observable in actual macroscale composites — ranging from covalent bonding of the coupling agent to both fibre and matrix, to simply plasticising and toughening of the matrix by the low molecular weight sizing components. Both of these likely contribute to the properties of real interphases with relative contributions changing based on the used sizing [8,9]. The interphase could be described as a gradient shift in composition from covalently and hydrogen bonded coupling agent [1,8], film former and matrix. Such a structure would hypothetically offer both the improved interfacial contact – via an interpenetrating network of matrix and the sizing connected to the fibre surface, not excluding the possibility of direct covalent bonding – and an altering of matrix properties in relation to bulk matrix. Cyclic loading of microcomposites of the appropriate scale range could provide valuable insights into the performance of this region and thus help understand also the interphase structure in more detail.

So, many questions about the nature of the interphase and its performance under cyclic loading still remain. In the context of microcomposite testing, however, among the greatest issues is still the discussion around scale related issues in resin properties and whether microcomposite tests in general have any correlation with macroscale [10–12]. Further work is needed to bridge the gap in qualitative understanding of the correlation between structure and composition the properties of the interphase, determining how quantitative the results can be, and how to utilise the results in composite design. Incorporating finite element analysis (FEA) has proven an increasingly effective tool for predicting test related phenomena, which remain otherwise difficult to observe [13]. Incorporating FEA in the analysis can therefore both help understand the phenomena and validate the experimental approach.

Here, we present an efficient micro-fatigue test based on the microbond concept for characterising composite interphases. Reliability was achieved by the collection of a large range of data to analyse the fatigue properties of the interface, and thorough characterisation of the testing setup to minimise device and test related contributions. On average 10 to 15 droplets were measured per single filament and the effect of fibre sizing was analysed based on both fatigue life performance and an in-depth analysis of the micromechanics, using FEA, based on the recorded force-strain data. Each test was performed as cyclic tensile loading (R ratio = 0) test with near-constant peak force until the droplet was completely sheared from the fibre. The damage propagation at the interface during cyclic loading was analysed and the contributions of dissipative and non-dissipative energies were evaluated. The heating of the micro-droplet due to the plastic deformation, the strain strain-rate dependency of the results and the role of friction in the test were explored through FEA.

2. Materials and methods

2.1. Experimental

The experimental setup for fatigue testing was based on the FI-BRObond device [14]. The only major modification was the change of the displacement actuator from a DC motor to a magnetic linear actuator capable of rapid accelerations and near frictionless operation — both crucial for this type of cyclic testing. During the test, the drive was operated at a speed of 2.0 mm/s, with the displacement amplitude varying based on the droplet embedded length and the desired load level for each test. The resulting frequency range was 6–10 Hz depending on the displacement amplitude of each measurement. The higher strain-rate – compared to the quasi-static microbond test – was expected to affect results but the increased rate was also necessary to control the time required for a single measurement. The role of strain-rate was evaluated in Section 2.2.

Early on, an issue was identified where the peak force level gradually decreases as the test progresses, both due to the plastic deformation of the droplet at the beginning of the measurement and possibly the propagation of the damage in the later stages. To keep the peak strain (and force) as constant as possible throughout the measurement, an algorithm was added to the measurement control that monitors the peak force levels and compensates for any changes over time with approximately 0.5–3.5 micrometer shifts to the starting position of the cyclic displacement along the fibre axis. The exact value for each compensation was dependent on the displacement amplitude and the stage of the measurement. Preliminary tests supported the initial hypothesis that the later stage compensation events correspond to propagating damage in the microcomposite sample, and thus, were logged into the measurement outputs as a potential qualitative measure of damage evolution. To better understand the loading state in terms of strain – an inarguably important part of any fatigue consideration – the fiber Bragg grating (FBG) sensor solution presented by Dsouza et al. [13] was used to monitor the fibre strain to provide additional input for FEA.

For fibres, an old batch of Jushi ECR-17 glass fibre roving, was treated with pirahna solution to remove any organic sizing or residues from the fibre surface. Half of the cleaned fibres were then resized with a 1% non-volatile content solution comprising 3-aminopropyl triethoxysilane (10%) and Hydrosize EP871EU epoxy dispersion (90%), kindly supplied by Michelman (Michelman International SARL, Luxembourg). The solution was used to create a fresh – and compositionally known – model sizing on the fibres. These two fibre types are denoted as unsized and sized fibres, respectively, in this study.

Several dozen droplets of Araldite 5052 LY/Aradur 5052 (resin/hardener, 100/38 parts by weight) epoxy system were deposited on each single fibre, spanning a length of 14–15 mm between the points of support provided by the sample holder (see Fig. 1). The droplets were cured at 80 °C for eight hours. The droplets were debonded either with both quasi-static loading (microbond test) or cyclic loading (micro-fatigue test). The microbond test was to provide a direct point of comparison for the fatigue test results. For the microbond tests, the speed of the magnetic actuator was set to 0.008 mm/s.

2.2. Finite element analysis

A 3D finite element model (FE) of the test was developed using Abaqus Standard/Explicit 2020 (Dassault Systèmes, France). The droplet ($\phi_{droplet} = 0.036$ mm and $A_{embedded} = 0.102$ mm) was chosen from the test of sized filament ($\phi_{fibre} = 0.0178$ mm) located 6 mm from the fixed position of the fibre. A systematic approach was followed wherein the FE model was developed for a quasi-static microbond test using an implicit solver for static analysis (*FE1-static*) and the coupled temperature–displacement analysis (*FE2-accum* and *FE3-dissip*). To investigate the dynamic effects, the FE models were further simulated with an explicit solver (*FE4-dyn*). In all cases, the filament (fibre in test),
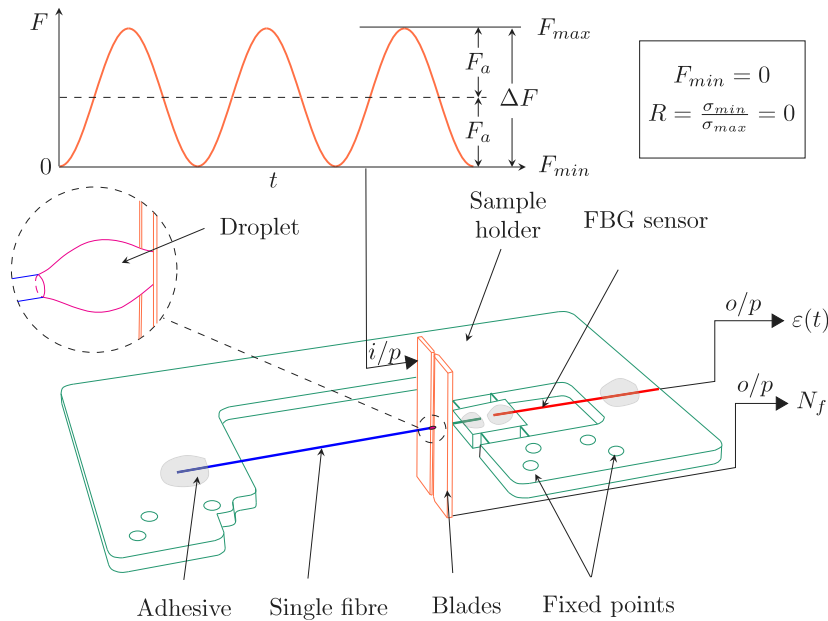
Fig. 1. Experimental arrangement of the microbond-based fatigue test used in the study. Here F_a, R, $\epsilon(t)$ and N_f represent force amplitude, fatigue stress ratio, time dependent strain and number of cycles to failure, respectively.

FBG sensor, sample holder and adhesive were modelled as linear elastic materials and the loading blades as rigid bodies (setup of FE model in Fig. 2). For the interface, surface-based cohesive zone modelling (CZM) was used with the maximum stress criterion for damage onset and a mixed-mode power law for damage evolution. Force and fibre strain data from the experiments were used to validate the interfacial constants such as critical stress (τ_c) and critical energy of debonding (G_c) using force-strain derivative data [15]. The interfacial constants were determined as $\tau_c = 50$ MPa and $G_c = 50$ J/m² for the sized filament (used for all FE models in this paper). For the unsized filaments these constants are $\tau_c = 39$ MPa and $G_c = 44$ J/m². It was assumed that the mode I component of G_c and τ_c behaved in the same way as the mode II and mode III components. In all cases, the epoxy droplet was treated as elastic–plastic with isotropic hardening conditions. The evolution of the plastic strain at different strain rates was incorporated into the *FE4-dyn* model (the data is provided in Supplementary Data S1). Details of the boundary conditions and numerical values of the mechanical constants can be found in previous publications [13,15]. The shrinkage of the droplet due to cooling from the curing temperature of 80 °C to a room temperature was simulated by including a temperature difference of −56 °C as a loading step in the analysis. For element types, linear brick elements with reduced integration (C3D8R) were used for *FE1-static* and *FE4-dyn*, whereas tri-linear displacement and temperature brick elements with reduced integration (C3D8RT) were used for *FE2-accum* and *FE3-dissip*.

The thermal material constants of the components at room temperature, which were used for the *FE2-coup* and *FE3-dissip* cases are provided in Table 1. The full, temperature dependent thermal conductivities and specific heats are provided in supplementary data S2 and S3, respectively. The convective heat transfer coefficient of 13 Wm⁻² K⁻¹ was defined as a film coefficient and was applied on the outer surface of the droplet and the fibre. A thermal conductance of 21 Wm⁻² K⁻¹ was used between the fibre and the droplet: the detailed explanation for this is provided in supplementary data S4. Only the inelastic deformation (90%) of the droplet was considered for the heat generation and no

frictional component was modelled in the current simulations. It is also important to note that the heat originated due to the interfacial degradation is not taken into account for any of the FE simulations. The FE model attributes were set to a temperature of 24 °C for all the cases.

To study the effect of blade velocity during the cyclic test, a single cycle test was simulated at different displacement rates using *FE4-expl*. A displacement amplitude lower than the damage onset value was chosen and kept constant while the cycle time is varied to achieve certain displacement rate. A stable time increment was selected and kept constant ($\delta t = 8 \times 10^{-10}$ s). To simulate the cyclic testing, a cyclic load with constant peak force at different levels was provided as an input to the models and corresponding compensation of blade displacement was recorded. For friction, two different origins are considered relevant in this study. Friction at not fully debonded regions (adhesional friction) and at debonded regions (sliding friction), the former being very complex to observe or measure. Even for the sliding friction, a definitive value of the friction coefficient (μ) cannot be accurately determined from the values of the sliding force in the experiment (i.e. when the droplet slides on the fibre after debonding, denoted F_{fric}). A very thin residual film is formed at the droplet exit point during droplet preparation, which increases the experimental F_{fric}. This in turn leads to overestimated the values of μ and poses a challenge in estimating it. Thus, for the purpose of this study, friction is addressed qualitatively using FEA through μ values, which lie within reasonable limits for the tests. An isotropic Coulomb friction model is used in conjunction with the CZM. The temperature effects are investigated by simulating *FE3-dissip* with $\mu = 0.1$, 0.3 and 0.5, where the fraction of friction converted to heat is defined as 100%. To explore the role of friction in the results, *FE4-expl* is simulated with $\mu = 0.1$ and the number of input cycles is increased until the droplet debonds from the interface.
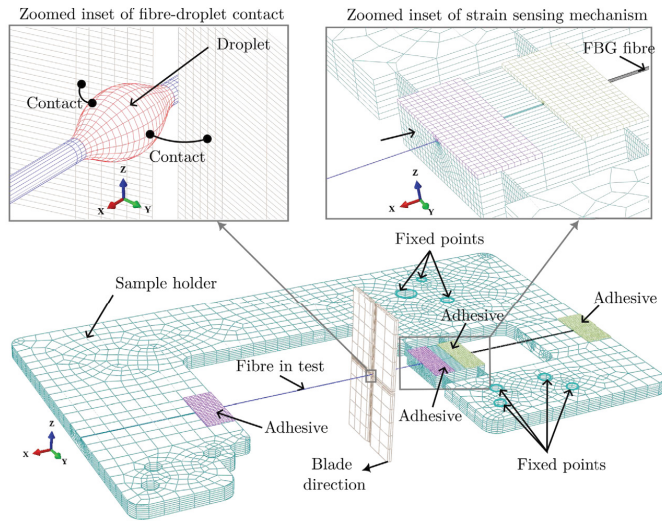
Fig. 2. Full setup of the FE model along with the zoomed insets.

Table 1
Values of the thermal material constants used in FE modelling.

Constituent	Thermal conductivity, K (W m^{-1} °C^{-1})	Specific heat (J kg^{-1} °C^{-1})	Coefficient of thermal expansion (×10^{-6}1 °C^{-1})	Source
Droplet	0.241[a]	237[a]	71[a]	in-house
Filament	1.3	805	4.1	[16,17]
Optical fibre	1.3	805	4.1	[16,17]
Sample holder	7.1	553	8.7	[18]
Blades	45	460	10.8	[19]
Adhesive	0.14	300	25	[b]

[a]Temperature dependent data available in the supplementary file.
[b]Generic adhesive values from different sources.

3. Results and discussion

3.1. Experimental results

A total of 117 droplets were measured with cyclic loading. Out of these, 108 were considered successful measurements. The rest comprised either fibre breakages or prematurely halted measurements — due to either run outs (i.e. tests run for 10^7 cycles without failure) or software problems. The scattering of the results was fairly high, which is expected in a fatigue test [20]. To ensure the comparability of the two data sets the embedded length ranges of the droplets were kept similar, i.e. 98.1 ± 12.9 μm for the unsized and 94.1 ± 11.2 μm for the sized fibres. The fibres were also similar in diameter: unsized fibres 18.3 ± 0.9 μm, sized fibres 18.3 ± 1.3 μm.

As the primary output of the fatigue testing, the stress-number of cycles (SN) curves for the two sample systems are presented in Fig. 3(a) and (b) along with results from the quasi-static (microbond) testing for comparison.

Fig. 3(c and d) show the Weibull probability plots for the cyclic tests separated into three apparent peak stress groups. The groups were selected by selecting the datapoints with average apparent stress levels during the test in the range of mean ±1/2× standard deviation of the whole dataset, with the high and low outliers forming the two other groups. The sized fibres outperformed the unsized fibres at all loading levels. The Weibull analysis indicates that at practically any comparable loading levels, the sized fibres have a smaller probability of failure. Therefore, it seems the sizing and the resulting interphase

are crucial for the fatigue life under cyclic loads similarly to what was previously reported by Mäder et al. [5]. The Weibull fits were used to predict fatigue life (Nf) at probability levels 2.3% ($Nf_{2.3\%}$), 50 % ($Nf_{50\%}$) and 97.7% ($Nf_{97.7\%}$). For the average apparent stress levels of the two fibre types, these values are estimated as: $Nf_{2.3\%}$ of 5.8 (sized) and 3.2 (unsized), $Nf_{50\%}$ of 4780 (sized) and 2180 (unsized), and $Nf_{97.7\%}$ of 136 000 (sized) and 57 000 (unsized). The amount of data is, however, not sufficient for a more detailed analysis, and the results cannot be considered more than qualitative.

Analysis of the Pearson's linear correlation coefficients of the experimental outputs (peak force, fibre/droplet volume fraction) versus number of tested cycles reveals a significant difference between the two sample types. Volume fraction was selected as it combines all geometrical aspects of the drop-on-fibre sample and to avoid significant changes in sample behaviour – due to, for example, local stress fields, strain rate dependency or changes in resin degree of cure – the intent was to have a suitably narrow range of droplet sizes to minimise any correlation. Thus the result would mainly be dependent on the applied load. Analysis of variance (ANOVA) was utilised to identify deviating datasets based on the individual filaments, which could highlight problems in experimentation or sample preparation. The results of this analysis are presented in Fig. 4. The correlation analysis in Fig. 4 appears to distinguish two very different behaviours for the sample types where for sized fibres the tested number of fatigue cycles correlates most with the volume fraction i.e. the relative size of the droplet with little of the expected correlation with the applied peak force level while the reverse is true for the unsized fibres. The ANOVA,
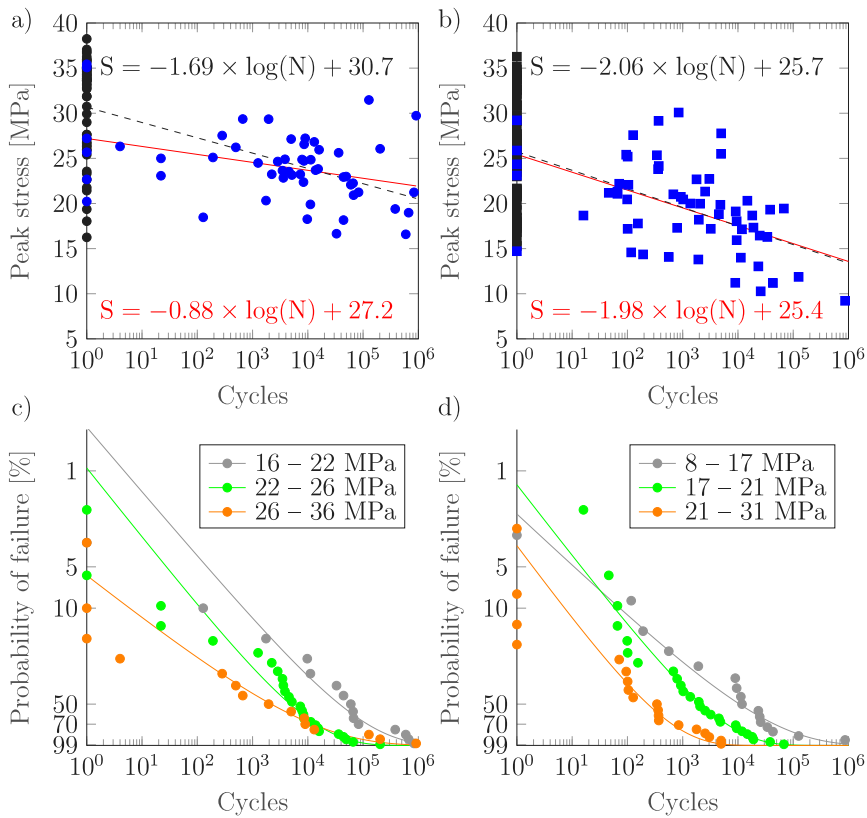
Fig. 3. Results of the fatigue testing, SN plot of (a) sized and (b) unsized fibres at R = 0 (displacement rate: 2.0 mm/s). Quasi-static results (displacement rate: 0.008 mm/s) presented for comparison in black. Red fitted curve: micro-fatigue results only. Dashed fitted curve: all results included. Weibull probability plots for sized (c) and unsized (d) fibres. Data is separated into three stress level groups signified in the legend.

however, revealed both complete datasets comprise several behaviour groups. For both sized and unsized fibres, the largest filament datasets follow the originally assumed behaviour: correlation mainly between peak force and number of cycles. Some correlation with droplet size is also noted for several datasets, while for some the number of measured droplets was too small to draw any reliable conclusions. Overall, this follows the behaviour reported earlier for the quasi-static test [14]: a significant portion of the scatter in the data arises from the variation between the individual filaments of the fibre bundle. The problem of high scatter of the results and the resulting poor correlation could be mitigated with either significantly more data, or by more extensive use of local parameters, such as the local strain recording [15], which in this study was mainly utilised for the purpose of FEA.

The sample deformation during the fatigue testing was observed by the compensations done by the algorithm to keep the load level constant. Examples are presented in Fig. 5 with arrows indicating the same compensation events in the peak force and number of compensation plots. The compensation counts in Fig. 5 hint at two very different damage evolution processes. The initial compensations – coinciding with the increasing load level – correspond to the plastic deformation of the meniscus at the blade contact and initial damage formation quite early in the measurement. In Fig. 5 these are observable as the frequent early compensations at steady intervals. This behaviour was also predicted by the FE simulation of multiple loading cycles (see Section 2.2). The progression of the deformation tended to differ between

the two sample types. For the sized fibres, the rate of compensations was lower, possibly indicating the interphase is more stable. However, after a significant number of cycles, the rapid compensations indicated a quite rapid propagation of damage until failure. For the samples with no sizing, the rate of compensations remained consistent throughout the measurement. The behaviour correlates with the observations made during the measurements: the washed samples exhibited a generally more brittle behaviour.

Comparing the results with quasi-static method, i.e. the microbond test, revealed a similar difference in performance of the two fibre batches. The microbond results were measured from the same filaments as the fatigue testing to minimise the effect of variation between filaments, which has previously been shown to be quite significant [14]. The results of the microbond tests are presented in Fig. 6 as maximum force during the experiment vs. droplet embedded area ($A_{embedded}$) calculated from the droplet embedded length and fibre diameter.

The results are sufficient for comparative analysis. The amount of tested droplets was, however, slightly limited due to the increased risk of fibre breakage during and after the fatigue testing. The fibre breakages were caused either by a poor guess of the initial displacement amplitude causing a too high force level, or unexpected fibre failure due to the repeated loading cycles. The most common filament breaks were, however, caused during microbond testing of a fibre subjected to significantly over 10^7 loading cycles, i.e. after several droplets were measured in with cyclic loading. The stress levels on the filament during the cyclic
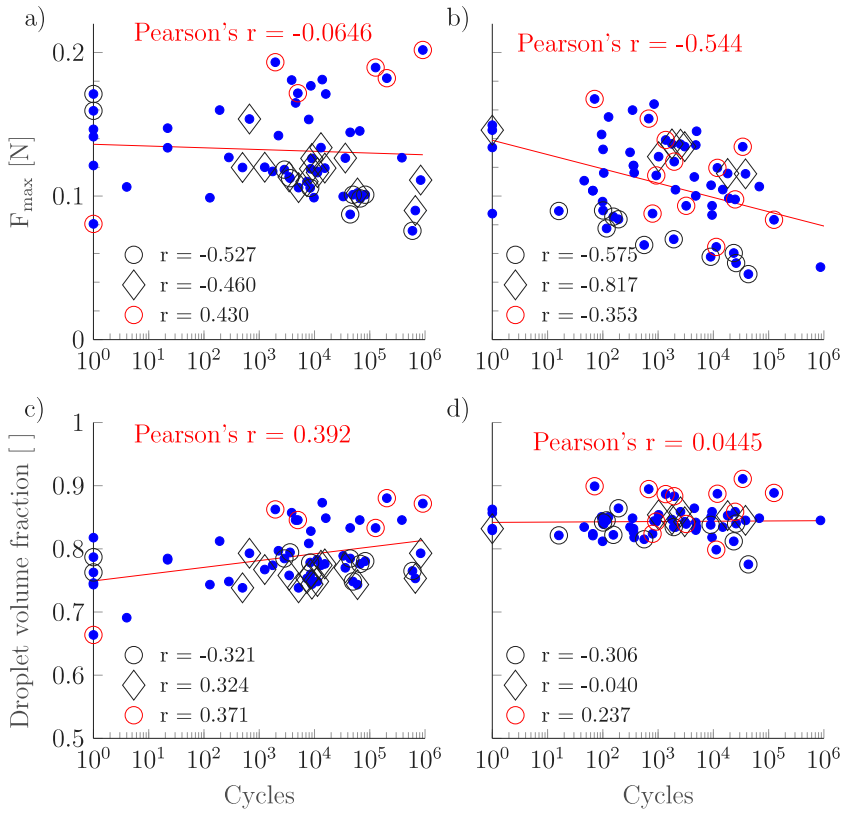
Fig. 4. Correlation analysis of different factors vs. the number of cycles. (a)–(b) Peak force (F_{max}) for sized and unsized fibres, respectively. (c)–(d) Droplet volume fraction for sized and unsized fibres, respectively. Overall Pearson's r for all data in red. Highlighted datapoints correspond to data from different individual filaments along with their Pearson's r values.
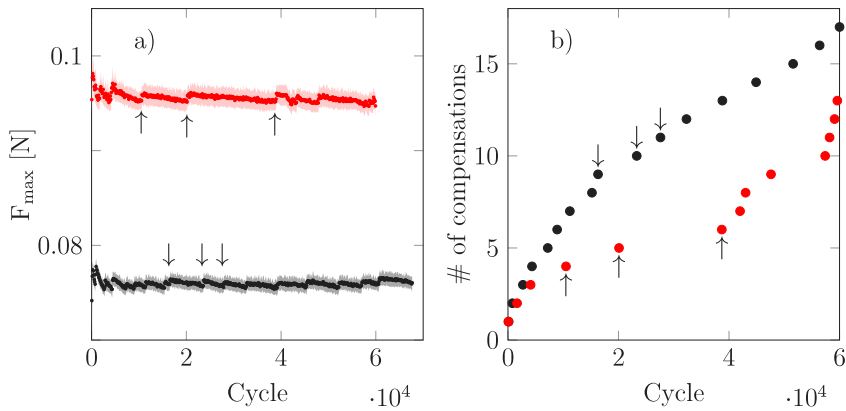

Fig. 5. Local averages and standard deviations (100 points) of load peaks (a) and compensations (b) for selected measurements of unsized (black) and sized (red) samples lasting approx. 67 000 and 60 000 cycles, respectively. The arrows indicate examples of corresponding compensation events in the two plots.
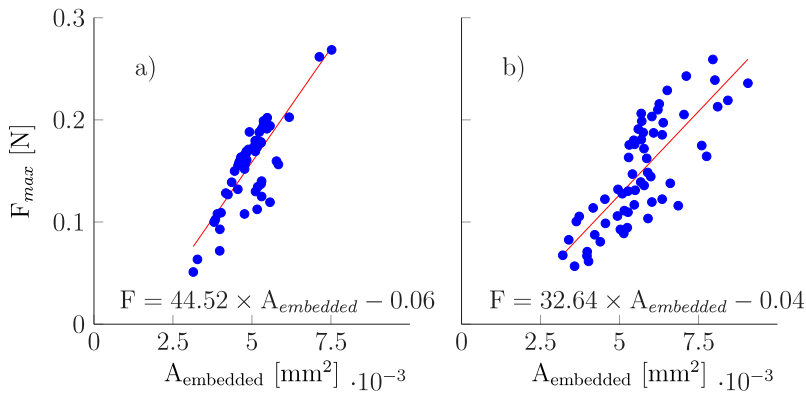
Fig. 6. Results of the quasi-static (microbond) tests for (a) sized (b) unsized fibres. $A_{embedded}$ is droplet embedded area.
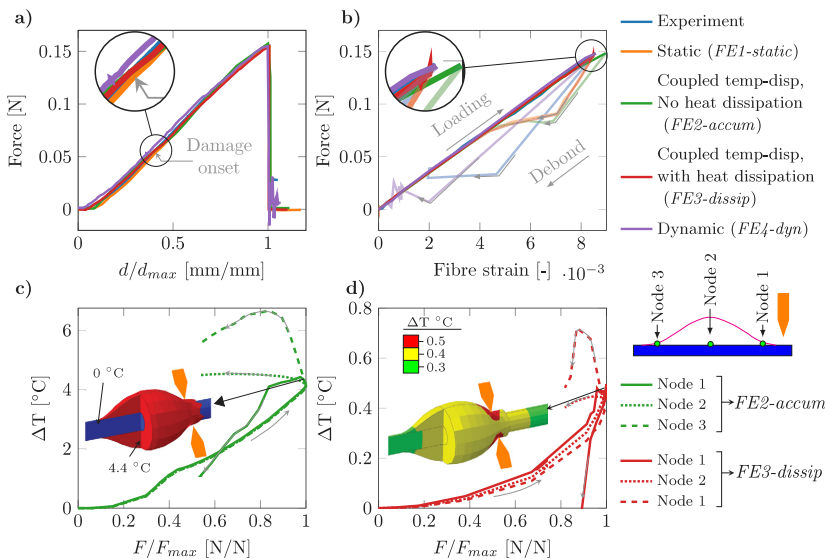

Fig. 7. Plot (a) force as a function of displacement; (b) output force as a function of fibre strain; (c,d) temperature at three different nodal points (close to the interface) from FE model as a function of force. Blade displacement (d) and force (F) are normalised with the corresponding d and F at the maximum value of force (F_{max}).

loading are low compared to the fibre ultimate properties and assumed to not affect the fibres excluding the aforementioned scenarios of fibre breakage.

3.2. FEA results

The FE simulation results for the quasi-static microbond test with different solvers are presented in Fig. 7(a)–(b). Except for *FE2-accum*, all the FE simulation results are in excellent agreement with the experimental force-fibre strain data, in-turn validating the interfacial constants used for the simulations. *FE2-accum*, deviates slightly from the experimental results as the accumulated heat in the droplet affects the interfacial damage.

Fig. 7(c)–(d) shows the distribution of temperature at three nodal points close to the interface. In the quasi-static case, a significant amount of heat was generated due to the plastic deformation of the droplet with $\Delta T \approx 7$ °C (Fig. 7(c)). This heat was dissipated to the

fibre via thermal conduction and further to the surroundings through the fibre and the droplet surfaces. There was no physical heat transfer through convection in the FE model, but the effective heat transfer was simulated using the surface film coefficient, which mimics the effects of convection. Under these conditions, *FE3-dissip* simulation showed that ΔT does not exceed 0.7 °C for a quasi-static test. Therefore, the deformation related heating of the sample does not affect sample behaviour in the static tests.

FE simulations also enable the evaluation of the role of strain-rate in the test. The resin itself has clear strain-rate dependency (of modulus of elasticity) and similar effects are expected in the microdroplet scale. A single cycle test at the blade displacement rate of 0.1 mm/s is shown in Fig. 8(a)–(c), wherein the input single cycle is provided to the blades in the form of smooth amplitude displacement (b_d). The maxima of the different quantities (denoted with subindex "*max*") are plotted as a function of displacement rates as shown in Fig. 8(d)–(f). The maximum of the kinetic energy (KE_{max}) is way lower than the maximum of the
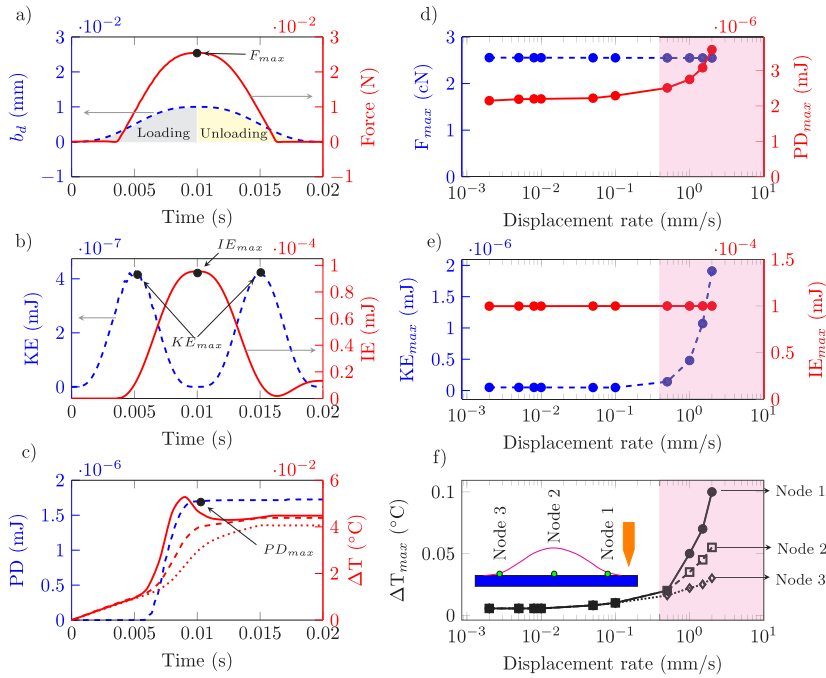
Fig. 8. (a)–(c) Results of FE simulations for a single cycle test at displacement rate 0.1 mm/s; (d)–(f) Results of FE simulations as a function of displacement rate.

internal energy (IE_{max}) up to a displacement rate of 0.5 mm/s. The micro-fatigue test exhibited dynamic behaviour when the displacement rate of the blades exceed 0.5 mm/s. This result is based on KE_{max} where a significant change in slope was observed. Similar behaviour was observed with the energy dissipated due to plastic deformation of the droplet (PD), which increases with the increase in displacement rate. This also led to the increase in the nodal temperatures (T_{max}). It is evident that the T_{max} was higher at Node 1, due to the higher rate of droplet deformation when compared to Node 2 and Node 3. As the micro-fatigue experiments were carried out at 2 mm/s, the tests were well within the strain rate range of these simulated dynamic effects.

For load levels corresponding to 25%, 60% and 80% of F_{max} (per simulated test), 20 consecutive input cycles were simulated and the results are presented in Fig. 9. The need for a steady increase in b_d was observed to keep the peak force per cycle constant. It is similar to the behaviour observed during the experiments, where a compensation is needed to keep the peak force level constant but actualised through a change of the zero position of b_d closer to the droplet. With an input force of 80% of F_{max} (0.12 N), the interface was completely debonded at 17 cycles. The crack initiates in the first cycle for all the cases. Comparing all the three force inputs (levels) one can observe a clear pattern in the growth of PD and energy dissipated due to interfacial damage and crack (DMD), with a non-linear rise of the curve at the start and abrupt rise at the end. For the initial blade contact with the droplet, contact area was lower at the meniscus, which promotes larger energy dissipation. This leads to the sudden rise of PD followed by a non-linear rise until the blades deform the meniscus region. The test becomes stable for a large number of cycles depending on the input force level, which represents the largest part of the cycles measured during the real test. For the case of complete debonding of the droplet, the undamaged area of the interface becomes so small, that the compensation of b_d increased drastically, which initiated an abrupt increase in PD and an unsteady propagation of DMD. At lower force

levels, PD and DMD does not increase significantly during the first few cycles followed by a slow growth during the subsequent cycles. This increased the expected fatigue lifetime of the interface during cycling loading compared to cases where significant plastic deformation and interfacial damage were generated early.

3.3. Effect of interfacial friction

When studying friction effects, it is important to note that damage evolution is a mixed mode, allowing damage propagation in all three modes. The friction created between the fibre and the droplet in the damaged zone can lead to a temperature increase at the interface and in the fibre-droplet assembly. Comparing the temperature profiles of the quasi-static simulations (Fig. 10(a)), it is clear that the friction at the interface can drive up the heat release. The change in ΔT is not significant until the onset of damage because friction is not activated, whereas ΔT increases when friction at the interface is increased (3 °C maximum in ΔT). Subsequently, these changes are very significant after the droplet is debonded, as the increase in ΔT is only due to the frictional contact between the surfaces. Overall ΔT values are quite minimal and heating of the sample can be ruled out in the static tests.

In micro-fatigue testing, the friction between the fibre and the droplet at the damaged zone can significantly increase the fatigue tolerance. When damage initiates at the interface, the frictional force in the damaged region stabilises the damage propagation, resulting in an increased number of cycles, indicating a good fatigue tolerance. As an example, for the same input force profiles (Fig. 9(b)), the frictionless interface debonds in 17 cycles (Fig. 9(f)), while the interface with $\mu = 0.1$ debonds in 66 cycles (Fig. 10(b) and (c)). Larger friction between the fibre and the droplet leads to an increase in the number of cycles to failure. Furthermore, the damage propagation is steady and no exponential growth of DMD is observed as in the case of a frictionless interface. This is due to the energy dissipated due to friction (FD)
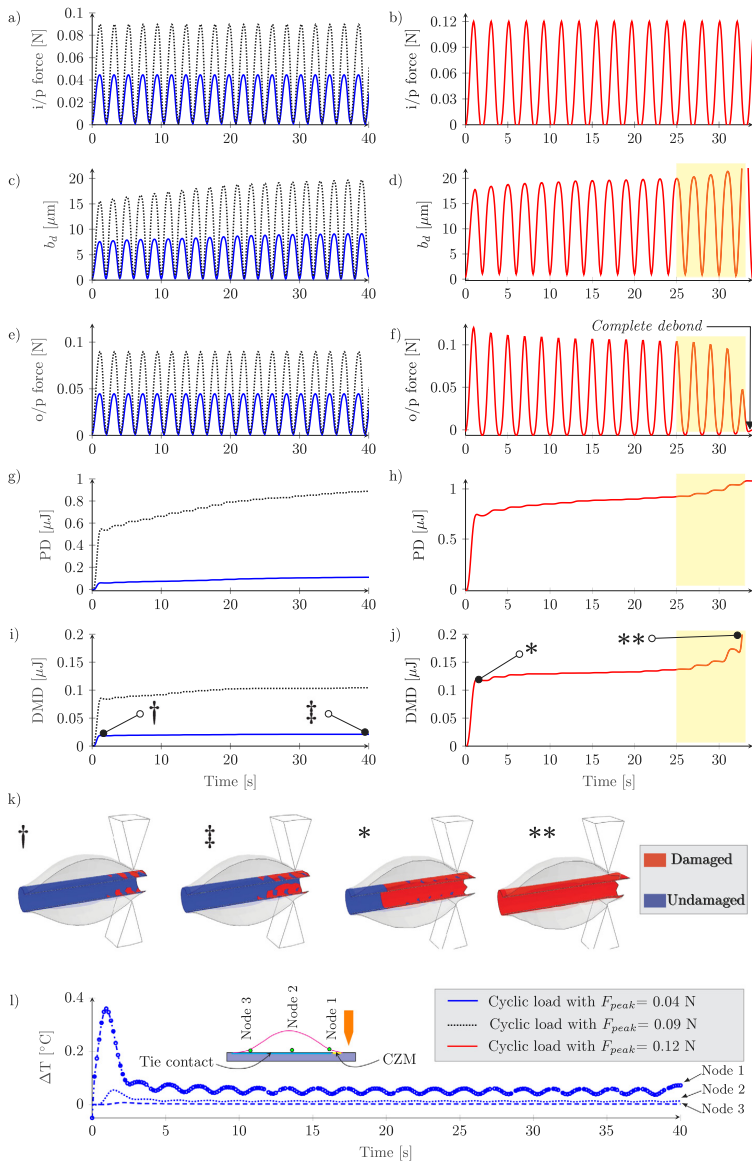
Fig. 9. (a–b) Input force as a function of time; (c–j) output quantities of FE simulations at different loading amplitudes; (k) visualisation of the damaged interface at specific simulation timepoints; (l) nodal temperature distribution for cyclic load with F_{peak} = 0.04 N. The shaded yellow box in (d), (f), (h) and (j) shows the abrupt rise in output quantities closer to the debonding of the droplet.

which steadily increases as the damage propagates at the interface. As the damage propagates, surface area of the damaged region increases, which increases *FD*.

3.4. Reliability and limitations

While promising, microcomposite fatigue testing is currently poorly established. Therefore a discussion on the possible problems and limitations is necessary. One point of consideration is the aforementioned

number of fibre loading cycles. Measuring multiple droplets from a single filament greatly reduces effort required in the sample preparation and experiment setup. The scatter in the results of droplets measured from the same filament is also significantly lower as previously reported for quasi-static tests. Further work is required to ensure the repeated loading of the fibre through several droplets does not significantly affect the results due to cumulative effects. Additionally, the free fibre-length changes based on the position of the droplet along the fibre (see Fig. 1). This directly affects the displacement amplitude necessary to reach a certain force level due to the fibre elastic deformation. Thus, in
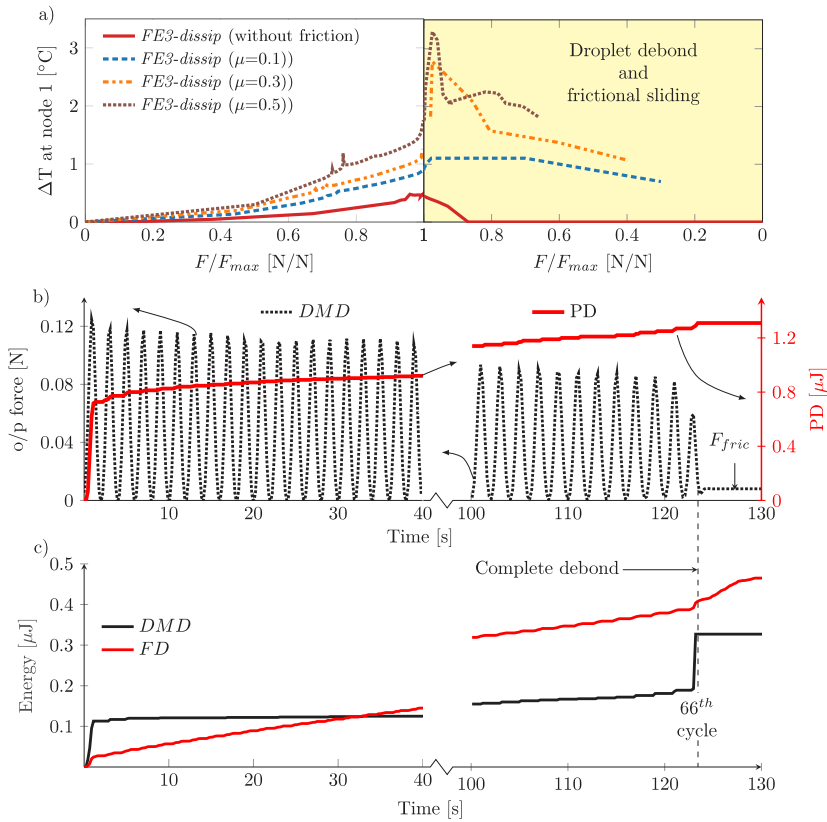
Fig. 10. (a) Simulation results showing the variation of temperature in quasi-static MB test for different values of frictional coefficient's; (b) and (c) different energy quantities extracted from the FE simulations for a cyclic test with interfacial friction with $\mu = 0.1$ used as a coefficient.

addition to the droplet size, the droplet position also contributes to the variation of the test frequency (blade movement speed kept constant). To minimise these factors in this study, the fatigue tests were performed only on droplets from the first 5–8 mm of the whole available 13–14 mm length of the fibre. The rest of the droplets were utilised for quasi-static testing when possible, as the effect of fibre's elastic deformation is mostly negligible in maximum load based analysis of the quasi-static results [14].

A problem also arises from the correlation between droplet size and the performance of the droplet in the test. While most of the samples did not exhibit such correlation, a notable portion did. The phenomenon is most likely related to the droplet degree of cure, which is a known source of uncertainty in microdroplet testing with thermoset resins [10–12]. It is, however, far more pronounced in fatigue testing and the underlying causes need to be identified and addressed before the method can be reliably utilised as more than a qualitative measure. In this study, the issue was mitigated by measuring similar size ranges droplets for both of the two fibre types and identifying the problematic data through analysis. Comparison to other methods and length scales is, however, not reliable until the issue of unpredictable microdroplet curing can be addressed.

Analysis of microcomposite interfacial tests commonly features considerations for two major contributing factors to the measured maximum load: friction and thermal stresses [14,21]. For the micro-fatigue test, while the presence of these factors cannot be argued, no in-depth analysis to their role is included based on the experimental results. The

FEA includes the thermal stresses from curing as a part of the model and the role of friction is likewise explored through FEA. It is worth of note that some qualitative correlation between the difference in damage evolution of the two sample types and the difference in frictionless and friction-included FEA: one exhibits sudden and catastrophic damage propagation, and the other a stable propagation and ultimately better fatigue tolerance. Possible explanations include the plasticising effect of the sizing, surface roughness and increased adhesive and/or sliding friction. The analysis of frictional contributions in the micro-fatigue test presents an interesting topic for future work.

Despite the aforementioned challenges, the method can provide valuable additional information about the interphase when coupled with quasi-static methods. At this stage of development, the method already offers unprecedented throughput and robustness (as a testing method) for a fatigue test at this scale. Based on the FE modelling used in characterising the method, the device and samples result in reasonably well-behaving measurements and the test exhibits good sensitivity to different interphase types. With future developments and understanding, the method could potentially provide quantitative data on the fatigue performance of the interphase.

4. Conclusions

In this study, the concept of a micro-fatigue test, based on the well-known microbond test setup was explored. The test exhibited excellent sensitivity to changes at the interphase as represented by two

fibre samples that were identical except for their surface treatments — a clean glass surface and a model sizing comprising an aminosilane coupling agent and an epoxy film former. A clear difference was noted in the fatigue performance at all tested loading levels and a difference in damage propagation was observed both experimentally and in FEA. This represents an important result towards understanding the role of sizing in composites and highlights the need to consider more than maximising the interfacial strength. The presented micro-fatigue test provides a potential methodology for further studies on the topic.

Finite element analysis was used extensively to study various aspects of the micro-fatigue test to identify the advantages and disadvantages of the methodology. The higher strain-rate – used to minimise the time requirement of a single measurement – had a clear but predictable minor effect on the force required to debond the droplets. This was supported by both FEA and experimental observations. Plastic deformation at the meniscus region is a known disadvantage of the microbond test but caused no additional changes in the sample behaviour and the resulting decrease in load level could be compensated in the cyclic testing. Damage evolution during the fatigue test can be qualitatively monitored via these compensations and the results agree well with the trend seen in finite element analysis. FEA analysis of the role of friction shows it can stabilise the damage propagation significantly, which also has possible implications on the mechanism of improvement by the sizing. Overall, the micro-fatigue test presented here is promising novel addition to the increasing selection of microcomposite testing approaches.

CRediT authorship contribution statement

P. Laurikainen: Conceptualization, Methodology, Formal analysis, Investigation, Data curation, Writing – original draft, Writing – review & editing, Visualization. **R. Dsouza:** Conceptualization, Formal analysis, Investigation, Data curation, Validation, Writing – original draft, Writing – review & editing, Visualization. **M. Kakkonen:** Methodology, Software, Resources, Writing – review & editing. **M. Kanerva:** Validation, Resources, Writing – review & editing, Supervision. **E. Sarlin:** Conceptualization, Resources, Writing – review & editing, Supervision.

Declaration of competing interest

The authors declare that they have no known competing financial interests or personal relationships that could have appeared to influence the work reported in this paper.

Data availability

Data will be made available on request.

Acknowledgements

Appendix A. Supplementary data

Supplementary material related to this article can be found online at https://doi.org/10.1016/j.compositesa.2023.107425.

References

[1] Thomason J. The interface region in glass fibre-reinforced epoxy resin composites: 3. Characterization of fibre surface coatings and the interphase. Composites 1995;26(7):487–98. http://dx.doi.org/10.1016/0010-4361(95)96806-H.

[2] Miller B, Muri P, Rebenfeld L. A microbond method for determination of the shear strength of a fiber/resin interface. Compos Sci Technol 1987;28(1):17–32. http://dx.doi.org/10.1016/0266-3538(87)90059-5.

[3] Fazlali B, Lomov SV, Swolfs Y. Fiber break model for tension-tension fatigue of unidirectional composites. Composites B 2021;220:108970. http://dx.doi.org/10.1016/j.compositesb.2021.108970.

[4] Mai K, Mäder E, Mühle M. Interphase characterization in composites with new non-destructive methods. Composites A 1998;29(9):1111–9. http://dx.doi.org/10.1016/S1359-835X(98)00092-X.

[5] Mäder E, Gao S-L, Plonka R. Static and dynamic properties of single and multi-fiber/epoxy composites modified by sizings. Compos Sci Technol 2007;67(6):1105–15. http://dx.doi.org/10.1016/j.compscitech.2006.05.020.

[6] Brodowsky HM, Jenschke W, Mäder E. Characterization of interphase properties: Microfatigue of single fibre model composites. Composites A 2010;41(11):1579–86. http://dx.doi.org/10.1016/j.compositesa.2010.07.006.

[7] Shin P-S, Kim J-H, Baek Y-M, Park H-S, Park J-M. Epoxy matrix with adding dopamine for improving mechanical property and interfacial adhesion with glass fiber. Compos Res 2019;32(2):96–101.

[8] Schutte CL. Environmental durability of glass-fiber composites. Mater Sci Eng R 1994;13(7):265–323. http://dx.doi.org/10.1016/0927-796X(94)90002-7.

[9] Ishida H. A review of recent progress in the studies of molecular and microstructure of coupling agents and their functions in composites, coatings and adhesive joints. Polym Compos 1984;5(2):101–23. http://dx.doi.org/10.1002/pc.750050202.

[10] Zinck P, Wagner H, Salmon L, Gerard J. Are microcomposites realistic models of the fibre/matrix interface? II. Physico-chemical approach. Polymer 2001;42(15):6641–50. http://dx.doi.org/10.1016/S0032-3861(00)00871-5.

[11] Laurikainen P, Pötz S, Jokinen J, von Essen M, Lindgren M, Kallio P, Kanerva M, Oreski G, Sarlin E. High-throughput mechanical micro-scale characterization of composites and the utilization of the results in finite element analysis. In: Proceedings of the 18th European conference on composite materials. European Society of Composite Materials; 2018.

[12] Bryce D, Thomason J, Yang L. Micromechanical and spectroscopic characterisation of the curing performance of epoxy resins in the microbond test. IOP Conf Ser: Mater Sci Eng 2020;942(1):012019. http://dx.doi.org/10.1088/1757-899x/942/1/012019.

[13] Dsouza R, Antunes P, Kakkonen M, Tanhuanpää O, Laurikainen P, Javanshour F, Kallio P, Kanerva M. Microscale sensor solution for data collection from fibre-matrix interfaces. Sci Rep 2021;11:8346. http://dx.doi.org/10.1038/s41598-021-87723-9.

[14] Laurikainen P, Kakkonen M, von Essen M, Tanhuanpää O, Kallio P, Sarlin E. Identification and compensation of error sources in the microbond test utilising a reliable high-throughput device. Composites A 2020;137:105988. http://dx.doi.org/10.1016/j.compositesa.2020.105988.

[15] Dsouza R, Antunes P, Kakkonen M, Jokinen J, Sarlin E, Kallio P, Kanerva M. 3D interfacial debonding during microbond testing: Advantages of local strain recording. Compos Sci Technol 2020;195:108163. http://dx.doi.org/10.1016/j.compscitech.2020.108163.

[16] Lin W-Q, Zhang Y-X, Wang H. Thermal conductivity of unidirectional composites consisting of randomly dispersed glass fibers and temperature-dependent polyethylene matrix. Sci Eng Compos Mater 2019;26(1):412–22.

[17] Nagy B, Nehme SG, Szagri D. Thermal properties and modeling of fiber reinforced concretes. Energy Procedia 2015;78:2742–7.

[18] Boyer R, Welsch G, Collings E. 32. Ti-6Al-4V. In: Materials properties handbook - titanium alloys. ASM International; 1994, p. 513–6.

[19] Harvey PD. 4.8 AISI Type 304. In: Engineering properties of steel. ASM International; 1982, p. 273–80.

[20] Lee Y-L, Pan J, Hathaway RB, Barkey ME. 4.2 The stress-life (S-N) and fatigue limit testing. In: Fatigue testing and analysis - theory and practice. Elsevier; 2005.

[21] Zhandarov S, Mäder E. Peak force as function of the embedded length in pull-out and microbond tests: effect of specimen geometry. J Adhes Sci Technol 2005;19(10):817–55. http://dx.doi.org/10.1163/1568561054929937.

PUBLICATION

III

Cut-off Scale and Complex Formation in Density Functional Theory Computations of Epoxy-Amine Reactivity

P. V. Laurikainen and E. L. Sarlin

Cut-off Scale and Complex Formation in Density Functional Theory Computations of Epoxy-Amine Reactivity

Pekka V. Laurikainen* and Essi L. Sarlin

Read Online

ACCESS | Metrics & More | Article Recommendations | Supporting Information

ABSTRACT: Most of the properties of epoxy resins are tied to their degree of cross-linking, making understanding the reactivity of different epoxy systems a crucial aspect of their utilization. Here, epoxy-amine reactivity is studied with density functional theory (DFT) at various cut-off levels to explore the suitability of the method for estimating the reactivity of specific epoxy systems. Although it is common to use minimal structures in DFT to reduce computational cost, the results of this study highlight the important role of hydrogen bonding and other noncovalent interactions in the reactivity. This is a promising result for differentiating the most probable reactive paths

for different resin systems. The significance of amine groups as a potential source of catalyzing H-bonds was also explored and, while not quite as effective as a catalyst as a hydroxyl group, a clear catalyzing effect was observed in the transition state energies. Unfortunately, the added complexity of a more representative reactive system also results in increased computational cost, highlighting the need for proper selection of structural cutoffs.
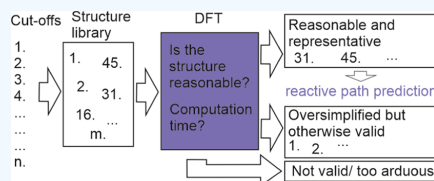
1. INTRODUCTION

For many epoxy applications, in-depth knowledge of the resin system chemistry is essential. The basic reactions of epoxy resins can be considered well understood, but the kinetics of curing,[1−3] ageing behavior,[4,5] polymer network formation,[3,6,7] and options for tailoring the structure and properties[8−10] remain subjects of active study in the field. The studies of the reactivity at the scale of individual molecules, bonds, and small differences between spatial isomers are only possible through *ab initio* or the computationally less arduous density functional theory (DFT) computations.[11−13] The performance and approximations offered by modern DFT implementations enable approaching the scale of full resin molecules, expanding the potential user base of the methods also toward materials science and chemical engineering.

Research on epoxy-amine reactivity commonly relates to different modifications of the base reaction, for example, the catalysis provided by hydrogen bonding.[14] The possible effects of hydrogen bonds (H-bonds) are twofold: H-bonding can lower the reactive barrier (catalysis) or stabilize the intermediate structure, causing a retardation effect.[13] Raman and Palmese[13] studied the latter by adding tetrahydrofuran into an epoxy-amine mixture. A similar retardation could also result from H-bond acceptors in the structure of the reagents, such as oxygen bridges in the epoxy and/or amine backbone. The catalyzing H-bonds are mostly considered to form with the hydroxyl groups formed during the addition reaction between the primary amine and the epoxide ring.[11−15] Most studies ignore the possible role of another H-bond donor—the amine groups themselves—likely due to the lower reactive barriers reported for hydroxyl group-catalyzed reactive paths.[11] However, the abundance of

available amine end-groups in epoxy-amine systems, especially in the early stages of the curing reactions, makes the amine groups a promising source of H-bonds.

In addition to H-bonding, epoxy-amine reactions are affected by inductive effects from the various chemical groups connected to the reactive center.[14] One example is the α-effect.[16] The α-effect is strong in methylated amines[17] and can, therefore, contribute to the results of computations of simplified structures. At least, if correctly predicted by the computation. The inductive effects are much weaker for larger structures[18] but, nevertheless, need to be considered in the total effect substituents have on the energy of the reaction and when estimating how changing the scale of the model system affects the computational results.

In this study, epoxy-amine reactions are studied computationally using modern DFT methods. The energy levels of the structures along the reactive path are computed at varying structural cutoffs. The aim is to explore the accuracy versus computational cost relation for a model epoxy-amine system and to see the effects various neighboring chemical groups can have on the reactive path. This should allow the qualitative prediction of the most probable reactive path for a given cutoff and offer insights into the complex role of noncovalent bonding in

stabilizing the structures along the reactive path. The different cut-off structures are manually built to represent commonly encountered epoxy-amine reactive systems with increasing complexity. For example, all epoxy structures are simplified cutoffs of diglycidylether of Bisphenol-A (DGEBA).

2. COMPUTATIONAL METHODS

The numerical computation was performed using the Schrödinger Materials Science Suite (Schrödinger Inc., New York, USA) software package (version 2020-4)—most prominently the Jaguar (version 11.0) DFT program.[19] The long-range corrected hybrid nonlocal B3LYP-D3 theory level was used for all DFT computations. The functional has been shown to give a good combination of accuracy and computational efficiency with many types of chemical structures and non-covalent bonding cases.[20,21] The M06-2X and ωB97X-D functionals along with B3LYP-D3 with Becke−Johnson damping[22] were tested in single point energy (SPE) computations for comparison. This part of the discussion is presented in the Supporting Information. The basis set was varied depending on the computational task. The 6-31G** basis set was used for the transition state searches and other initial structural optimizations.

The role of the structural cutoffs was explored using reaction workflows recently introduced to the Schrödinger Materials Science Suite. These simulations involve freezing the primary reactive groups of the structures and swapping fragments from the rest of the structure based on pregenerated examples shown in Figure 1. Ethylamine was selected as A1, instead of the simpler
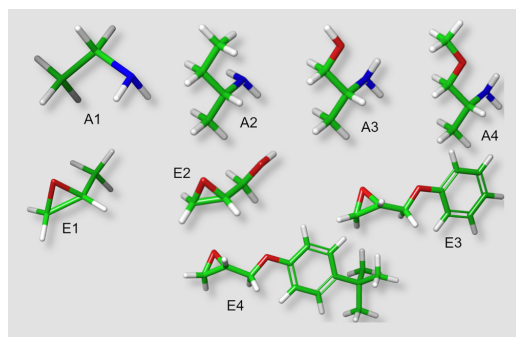

Figure 1. Cut-off structures for amine (A1−A4) and epoxy (E1−E4). The element coloring C: green, N: blue, O: red, and H: white, will be used throughout the study.

methylamine, to reduce the otherwise expected significant contribution of the α-effect for the reference structure. Ethylamine was also used as the catalyzing amine for all relevant simulations. Similarly, isopropyl alcohol was used as the source of the catalyzing hydroxyl group. In the figure (Figure 1), carbons are colored green, nitrogens blue, oxygens red, and hydrogens white. The same coloring will be used throughout this study.

In order to find the most probable reactive paths, a conformational search—using the MacroModel program with the OPLS3e force-field[23] for Monte Carlo Multiple Minimum searches—was added to each transition state search and reaction workflow. For the transition state searches only the lowest energy conformers are available as outputs, whereas in the

reaction workflows ten lowest energy conformers are requested from separate conformational search runs the same starting structure. The final structural optimizations in DFT were performed using the LACVP** basis set, which—as the workflow default—resulted in significantly less convergence issues in the workflow than the 6-31G** basis set.

The final energies of each structure—including the outputs of the transition state searches—were calculated as SPE computations using the cc-pVTZ(-F) triple zeta basis set for improved accuracy. Other relevant parameters of the Jaguar code include grid density for the DFT computations (fine for SPE, medium for all other computations) and the accuracy of the pseudospectral computations (ultrafine grids with tight cutoffs for SPE, mixed grid with loose cutoffs for all other computations).

All results are reported as averages and standard deviations of grouped sets of these computational results. The conformers are grouped based on the used fragments (Figure 1) and subgrouped based on conformational similarities, for example, similar H-bonding states. The computation times are reported from SPE computations. Because the actual duration of the computation depends on the computational performance of the hardware and, for example, the use of parallelization to speed up the computation, the values are reported relative to the fastest computation (A1,E1 uncatalyzed primary amine reaction) and are based on the total CPU time.

3. RESULTS AND DISCUSSION

The computations begin with a transition state search for the simple A1,E1 system. This was needed both to find the reference energy levels for the simplified system and for use as an input for the reaction workflow computations. Figure 2 presents the results of the transition state searches used to find the primary amine addition reactive paths, including the A1,E1 version of the amine-catalyzed reactive path. These act as starting points for the rest of the computations.

The results for uncatalyzed reactions are presented in Table 1 as transition state energies relative to the lowest reactant structure energy. This relative energy is used as a measure for the activation energy (E_a) or reactive barrier height.

The β-methylated hardeners (A2−A4) are known to result in slightly slower reactive systems compared to their linear counterparts. This is caused by the steric hindrance from the methyl group next to the amine.[14] The effect is overlooked by the simplified reactive system (A1,E1), but clearly evident as higher activation energies for each larger amine structure (A2−A4,E1). This already highlights the crucial role of the selection of the cutoffs when studying specific reactive systems.

For the more complex structures, certain specific noncovalent interactions emerge and—despite the vast number of possible conformations for the rest of the molecule—the structures involving these interactions share structural and energetic similarities. To highlight these specific interactions, they are presented in Schemes 1−3.

Contributions to the total energy can also be noted from conformations where the presence of H-bonding is uncertain but the proximity creates a more favorable energetic state. This is most common, for example, between an amine hydrogen and the nearby backbone oxygen (see, e.g., Figure 3a). Although similar to Scheme 1b, for larger structures, these often present as conformers with multiple oxygen groups coordinating around the amine hydrogen, as presented in 3e, Schemes 2a and 3. This type of complex is presented in Scheme 4.
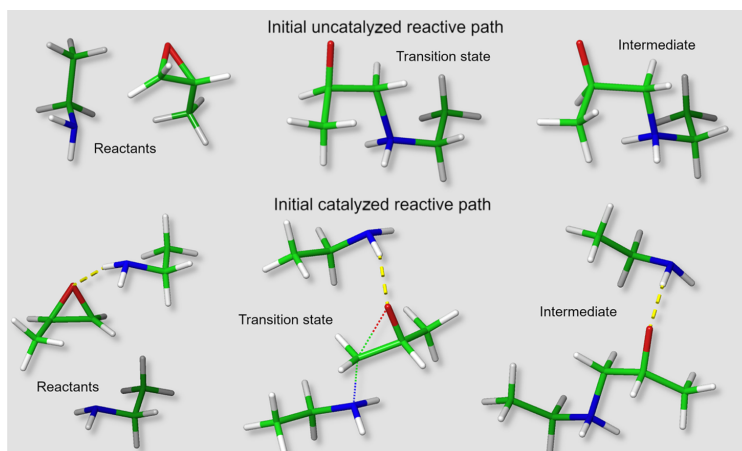
Figure 2. Reactive paths for simple and catalyzed primary addition reactions (A1,E1). The yellow dotted lines represent software identified H-bonds.

The hydroxyl group in the structure E2 manifested mostly conformations where the hydroxyl group interacts with the epoxide oxygen (See Figure 3c). Although accurate for the structure in question, these conformations are considered bad for the purposes of exploring the reactivity of a DGEBA-based epoxy system, in which the oxygen is part of the epoxy backbone (see e.g. Figure 3d,e). The A3 hydroxyl group also manifested some conformations that would be very unfavorable in a larger system (Figure 3b) at least with the assumption that this oxygen is similarly part of the amine backbone. Due to these considerations the choice was made to exclude these systems from the computations of the catalyzed systems.

Interactions are also observed between the aromatic ring and the polar functional groups. First examples of this type of behavior are observable from the A1,E3 secondary amine reaction, where the average height of barrier changes approximately 1−2 kcal/mol depending on the type of interaction. The highest reactive barriers (32.00 ± 0.48 kcal/mol) are observed for the conformers with no interactions between the hydroxyl group from the primary amine reaction and the aromatic ring in the epoxy structure. For a PhH → OH type interaction (Scheme 3b), the average barrier height decreases to approximately 31.13 ± 0.21 kcal/mol. Aromatic H-bonds are more commonly reported between an H-bond donor and the aromatic ring.[24] It is worth noting that the aromatic hydrogen in ortho-position to an oxygen is expected to have a slightly more acidic nature compared to a benzene hydrogen, which makes such interactions plausible. The lowest energy conformers (average of 29.01 ± 0.77 kcal/mol) present a OH → Ph type interaction (Scheme 3a) resembling the aromatic H-bond discussed by Brinkley and Gupta.[24] The examples of such structures are presented in Figure 4. Similar interactions were observed in the uncatalyzed A4,E4 secondary amine system.

When functional groups (amine or hydroxyl) are added to catalyze the reaction, the H-bonding of these added functional groups clearly changes the energetics of the reaction, which is in line with existing studies on the topic.[11,15] The catalysis is based on the extra functional group interacting with the opening epoxide ring, as presented in Scheme 5.

Mobility around the reactive center is likely overestimated in such a small model system, that is, it is improbable that every reactive site would have sufficient free volume surrounding it to allow this type of catalysis. Nevertheless, the model still helps highlight the differences between different options for H-bond formation, namely the hydroxyl and amine groups, and helps estimate the role of such catalysis in total reactivity. The transition state energies for the catalyzed reaction paths are presented in Table 2.

The H-bond between the amine group and a backbone oxygen (Scheme 1) appears a favorable conformation for systems large enough to orient suitably. Figure 5 shows examples of the effect this interaction has on the energy in the A1,E4 system. The effect on barrier height is unexpectedly minor. A possible explanation is that the orientation forces some bond angles to deviate from their equilibrium values increasing the energy.

Figure 6 shows the lowest and highest energy conformers for the amine-catalyzed A2,E1 secondary amine transition states. A complex H-bond network formed between the hydroxyl group—created in the primary amine reaction—and the amine-catalyzed reactive core (Scheme 5b) significantly lowers the reactive barrier for this path. It is also worth noting that the required orientation of the hydroxyl group also brings it close to the remaining amine hydrogen. The combined effect is quite significant (29.21 ± 0.90 kcal/mol VS 35.19 ± 0.64 kcal/mol).

In general, for the larger systems, the conformations and their interpretation become challenging due to the number of available interactions including possible complex cases such as the one presented in Scheme 4. For example, in the catalyzed A4,E4 systems, multiple noncovalent interactions are noted for most conformers (see Figure 7). The lowest energy conformations show oxygens coordinating around the amine hydrogen as in Scheme 4. In the higher energy conformers, however, either the amine backbone oxygen or the hydroxyl group from the primary amine is oriented away from the amine hydrogen. The difference in energies between these conformations appears to be in the range of 2−4 kcal/mol but in all cases other interactions contribute. A similar coordination around the amine hydrogen can also be observed in the uncatalyzed system presented in Figure 3h, and a similar difference in energy is

Table 1. Activation Energies (E_a) and the Number of TS Conformers (n) for the Uncatalyzed Reactive Paths[a]

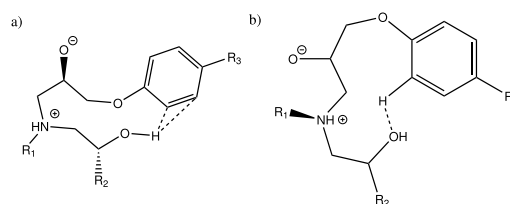| structure	E_a, [kcal/mol]		
− subgroup	primary (n)	secondary (n)	figure examples
A1, E1	34.26 (1)	32.31 (1)	Figure 2
− no interactions	34.26 (1)	32.31 (1)	
A2, E1	35.81 ± 0.72 (9)	39.75 ± 1.17 (10)	
− no interactions	35.81 ± 0.72 (9)	39.75 ± 1.17 (10)	
A3, E1	40.31 ± 1.55 (10)	41.03 ± 2.04 (9)	
− no interactions	41.47 ± 0.36 (6/10)	41.81 ± 1.70 (6/9)	
− Scheme 4	38.56 ± 0.39 (4/10)	40.58 ± 0.81 (2/9)	Figure 3a
− Scheme 2a	− (0)	37.21 (1/9)	Figure 3f,h
A4, E1	36.30 ± 1.67 (9)	36.81 ± 2.00 (10)	
− no interactions	36.30 ± 1.67 (9/9)	37.63 ± 1.09 (7/9)	
− Scheme 2a	− (0)	33.50 ± 0.66 (2/10)	Figure 3f,h
A1, E2	35.25 ± 1.39 (7)	35.46 ± 2.47 (9)	
− no interactions	35.25 ± 1.39 (7/7)	35.46 ± 2.47 (9)	
A1, E3	28.14 ± 0.77 (9)	30.48 ± 1.54 (9)	
− no interactions	28.88 ± 0.42 (3/9)	− (0)	
− Scheme 1b	27.77 ± 0.62 (6/9)	32.00 ± 0.48 (3/9)	Figure 3d,g,h
− Scheme 3b	− (0)	31.13 ± 0.21 (2/9)	Figure 4
− Scheme 3a	− (0)	29.01 ± 0.77 (4/9)	Figure 4
A1, E4	27.84 ± 0.51 (9)	29.66 ± 1.81 (9)	
− no interactions	28.27 ± 0.24 (3/9)	− (0)	
Scheme 1b	27.63 ± 0.47 (6/9)	30.27 ± 1.58 (4/9)	Figure 3d,g,h
− Scheme 3b	− (0)	31.30 ± 0.15 (2/9)	Figure 4
− Scheme 3a	− (0)	27.75 ± 0.66 (3/9)	Figure 4
A4, E4	27.14 ± 0.61 (10)	32.86 ± 1.68 (10)	
− Scheme 1	27.31 ± 0.57 (7/10)	33.51 ± 1.03 (6/10)	Figure 3d,g,h
−Schemes 1 and 2	− (0)	28.80 (1/10)	Figure 3h
− Schemes 1 and 4	26.72 ± 0.57 (3/10)	− (0)	Figure 3e
− Schemes 1 and 3b	− (0)	33.11 ± 0.81 (2/10)	Figure 4
− Schemes 1 and 3a	− (0)	32.51 (1/10)	Figure 4

[a]The conformers are subgrouped based on notable common interactions in Schemes 1−4. The "No Interactions" label indicates none of the presented schemes apply but other interactions with lesser impact on the reactivity can still be present.

Scheme 1. H-Bond between the Amine Group and a Backbone Oxygen from (a) Epoxy and (b) Amine. R_1 Epoxy Backbone; R_2 Amine Backbone
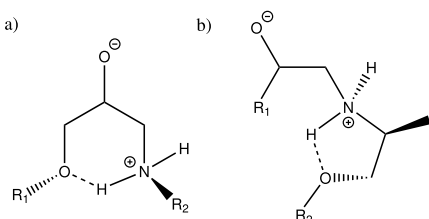
observed when one of the oxygens is oriented less favorably (see Figure 3g). Also, again additional interactions contribute, such as the OH → O H-bond presented in Figure 3h.

Scheme 2. H-Bond between the Hydroxyl Group and a Backbone Oxygen from (a) Amine and (b) Epoxy[a]
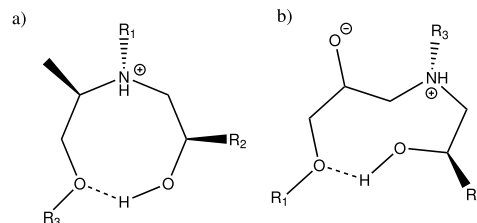
[a]R_1 = epoxy backbone, R_2 = epoxy backbone from primary amine reaction, R_3 = amine backbone.

Scheme 3. Noncovalent Interactions Involving the Aromatic Ring[a]

[a](a) Aromatic ring as a H-bond acceptor, (b) aromatic ring as a H-bond donor. R_1 = amine backbone; R_2 = epoxy backbone from primary amine reaction.

The aromatic interactions contribute significantly also in the catalyzed models. With the reactive center largely the same for a majority of the structures, the trend of increasing deviations for larger systems can be often attributed to how, for example, the hydroxyl group formed in the primary amine reaction is oriented in relation to the aromatic ring in the secondary amine reactions. The strength of the interaction—for cases resembling Scheme 3a—is in these results similar to what is observed for H-bonding, giving validity to the term of aromatic H-bonding.

Predicting the actual importance of the catalyzed paths using the DFT computation is difficult as the systems are effectively considered infinitely diluted, whereas molecular motion in the real epoxy-amine reactive systems is far more restricted. The observed catalyzing effect partly explains the accelerated reactivity when amine hardener is added in excess of the stoichiometric ratio. It is also very likely that whatever importance the catalysis has, it is mitigated as the curing process progresses, and the required molecular motions are restricted until it—after vitrification—become practically nonexistent.

Table 3 presents an overview of the computational times— the easiest measure for the computational cost—for the different systems. Some interesting observations can be made from these results. The most obvious one is as follows: increasing the complexity of the system increases the computational cost but also variation of the computational time. In the SPE computation, the biggest source of variation between similar structures appears to be the dispersion correction steps in the computation. The slightly longer computational times for hydroxyl-catalyzed compared to amine-catalyzed systems are likely a result of the slightly bigger system (isopropanol vs ethylamine).
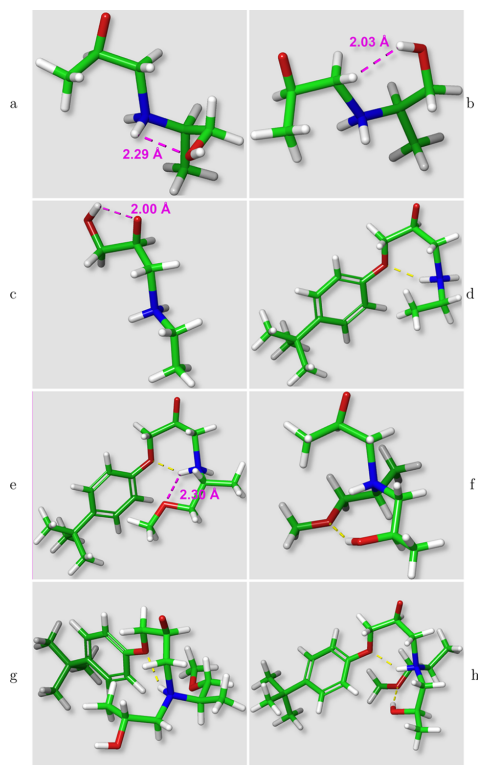
Figure 3. Uncatalyzed transition state conformers of (a,b) A3,E1, (c) A1,E2, (d) A1,E4, and (e) A4,E4 (primary) and (f) A4,E1, (g) A4,E4, and (h) A4,E4 (secondary). The yellow dotted lines represent software identified H-bonds.

Scheme 4. Complex Created from Multiple Surrounding O-groups Coordinating around the Amine Hydrogen. R_1 = Epoxy Backbone, R_2 = Amine Backbone, and R_3 = Epoxy Backbone from Primary Amine Reaction
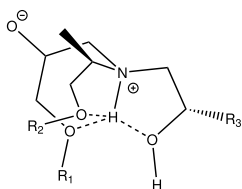
The reactant conformations of the reaction workflows provide an interesting point of discussion. Especially for the catalyzed reactive paths the lowest energy conformers show significant interactions between the added catalyzing functional group (OH or NH) and either one or both of the amine and epoxy functional sites. These minimal energy conformers tend to orient unfavorably considering the reactive path of the epoxy-amine addition reaction. Whether the needed reorientation manifests as an initial smaller reactive barrier, could be an interesting point of further study. However, the effect is likely
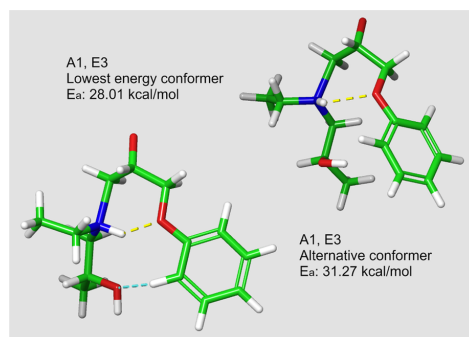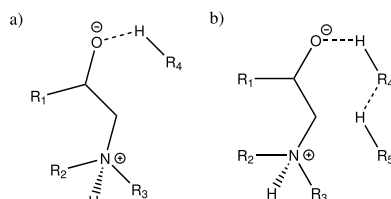

Figure 4. Different aromatic interactions in the A1,E3 secondary amine reaction. The yellow and blue dotted lines represent software identified H-bonds and aromatic interactions, respectively.

Scheme 5. Catalysis of the Epoxy-Amine Reaction by an Extra functional Group (OH or NH_2 = R_4)^a

^{a}R_1 = epoxy backbone, R_2 = amine backbone, R_3 = either hydrogen or the epoxy from primary amine reaction. In the models presented here R_5 is connected to one of R_{1-3}.

small compared to the advantage offered by the lowering of the reactive barrier in the rate determining step studied here.

No conclusive retardation effect was observed based on the computation results. However, some hints at possible metastable intermediate structures can be drawn from the results of the conformational searches of the intermediate structures. For example, the uncatalyzed primary amine reaction workflows resulted in intermediate structures close to the final product—indicating no local minima near the transition state. Whereas for the secondary amine reaction, the conformational search converged to local minima structurally and energetically near the transition state for all systems larger than the A1,E1 system. This could indicate the secondary amine reaction for our model system is in fact slower, even though the activation energies are largely similar. Here, as the core reactive path was kept largely constant in the set-up of the computations, possible key considerations, such as a backbone oxygen interacting and "deactivating" the catalyzing functional group, were not explored.

4. CONCLUSIONS

In this study, the epoxy-amine reaction was studied using the DFT computations at different cut-off scales to study the role various noncovalent interactions of the neighboring functional groups. A secondary goal was to test the potential of such computations in predicting the reactivity of a specific epoxy-amine system, at least qualitatively, with promising results. The selected cutoffs significantly affect the final energy levels. Most

Table 2. Overview of the Relative Barrier Heights for the Different Structural Cutoffs for the Catalyzed Cases[a]

| structure | E_a, amine-cat. [kcal/mol] | | E_a, hydroxyl-cat. [kcal/mol] | |
– subgroup	primary	secondary	primary	secondary
A1, E1	20.61	34.55 ± 2.90	32.22 ± 3.28	32.18 ± 1.48
– no catalysis			41.52	
– Scheme 5a	20.61		31.18 ± 0.16	32.56 ± 0.87
– Scheme 5b		30.48 ± 0.97		28.69
A2, E1	31.00 ± 0.78	32.20 ± 3.24	31.24 ± 0.66	31.67 ± 2.75
– no catalysis	31.33 ± 0.29			
– Scheme 5a	30.67 ± 0.99	35.19 ± 0.64	31.24 ± 0.66	33.28 ± 1.54
– Scheme 5b		29.21 ± 0.90		28.43 ± 0.91
A4, E1	30.14 ± 1.45	31.33 ± 3.43	29.38 ± 1.65	32.94 ± 1.67
– no catalysis		28.47		
– Scheme 5a	30.14 ± 1.45	34.68 ± 1.61	29.38 ± 1.65	32.98 ± 0.79
– Schemes 2a and 5a		32.23		32.96
– Scheme 5b		28.48 ± 2.39		29.85 ± 0.28
A1, E3	25.06 ± 0.69	26.40 ± 3.44	22.15 ± 0.50	26.09 ± 2.35
– no catalysis	24.66 ± 0.60			
– Scheme 5a		28.74 ± 0.71		
– Schemes 1a and 5a	25.66 ± 0.13	28.27 ± 1.60	22.09 ± 0.48	27.15 ± 1.31
– Schemes 1a and 5b		21.71 ± 0.69		22.35 ± 0.63
– Scheme 5b			22.68	24.67
– Schemes 3a and 5a				27.90 ± 0.21
A1, E4	26.76 ± 0.78	28.45 ± 3.58	23.69 ± 0.82	25.67 ± 1.46
– Scheme 5a	26.10 ± 0.52	31.46 ± 0.94		
– Schemes 1a and 5a	27.09 ± 0.67	28.94 ± 2.14	24.00 ± 0.88	25.69 ± 1.23
– Schemes 1a and 5b		22.68 ± 0.26		27.67
– Scheme 5b			23.22 ± 0.50	23.56
A4, E4	25.24 ± 1.50	32.06 ± 4.67	24.16 ± 1.22	24.45 ± 1.64
– Schemes 1 and 5a	25.24 ± 1.50	37.16 ± 3.97	24.32 ± 1.20	25.56 ± 0.01
– Scheme 5a		31.37 ± 1.46		
– Schemes 1, 3b and 5a		31.69		25.45 ± 0.63
– Schemes 3a, 4 and 5a				21.94 ± 0.08
– Scheme 5b			22.88	
– Schemes 1, 3b and 5b		26.81 ± 4.46		
– Schemes 1 and 5b		29.65		
– Schemes 3a and 5b				24.30

[a]The conformers are subgrouped based on notable common interactions in Schemes 1−5. "No catalysis" indicates conformations with no predicted interaction between the catalyzing functional group and the opening epoxide ring.
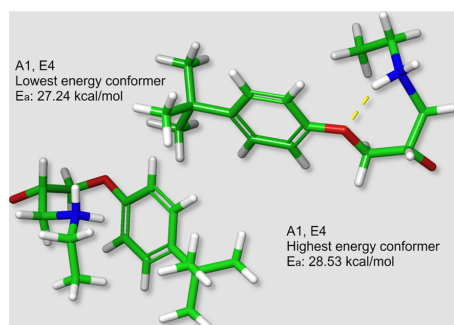

Figure 5. Maximum and minimum energy conformers for the A1,E4 primary amine reaction. The yellow dotted lines represent software identified H-bonds.
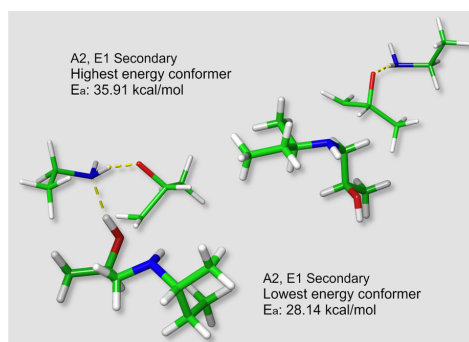
Figure 6. Maximum and minimum energy conformers for the amine-catalyzed A2,E1 secondary amine reaction. The yellow dotted lines represent software identified H-bonds.

consistent results were achieved with the largest and the smallest cut-off levels. The energy levels for the smallest and the largest structures are also very similar, which should be coincidental. Various important interactions were included in the computa-

tions as a result of the increased complexity of the systems. Based on our computations, the order of importance for different types of interactions to epoxy-amine reactivity is as follows:
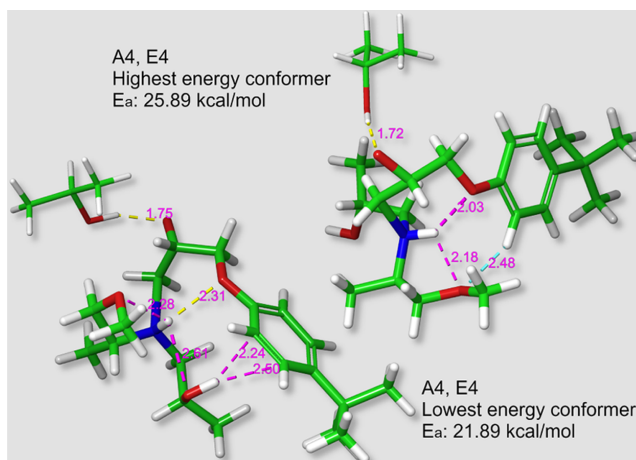
Figure 7. Maximum and minimum energy conformers for the hydroxyl-catalyzed A4,E4 secondary amine reaction. The yellow, blue, and magenta dotted lines represent software identified H-bonds, aromatic interactions, and the measured interatomic distances, respectively.

Table 3. Relative Computation Times for Different System Sizes (Single SPE Computation)[a]

	uncatalyzed		amine		hydroxyl	
structure	primary	secondary	primary	secondary	primary	secondary
A1, E1	1.00 ± 0.09	3.61 ± 0.44	4.05 ± 0.43	6.43 ± 2.07	4.89 ± 0.31	11.4 ± 1.4
A2, E1	2.93 ± 0.29	6.09 ± 0.92	7.60 ± 1.54	11.5 ± 2.6	9.76 ± 1.56	19.3 ± 3.1
A3, E1	2.18 ± 0.12	5.60 ± 0.54				
A4, E1	2.61 ± 0.29	4.97 ± 0.47	8.85 ± 1.17	17.4 ± 3.1	10.3 ± 2.4	20.4 ± 3.7
A1, E2	1.55 ± 0.22	4.47 ± 0.66				
A1, E3	6.71 ± 0.83	10.8 ± 1.7	12.0 ± 3.9	26.1 ± 5.7	13.9 ± 4.0	24.0 ± 7.5
A1, E4	14.6 ± 1.9	17.9 ± 3.0	20.0 ± 5.3	35.0 ± 11.6	22.5 ± 7.0	40.6 ± 9.4
A4, E4	18.6 ± 1.7	35.5 ± 4.4	24.6 ± 3.4	35.3 ± 3.7	42.8 ± 10.1	38.4 ± 3.6

[a]The reference time is approximately 2332 cpu seconds.

intermolecular H-bonding, intramolecular H-bonding, aromatic interactions, and inductive effects, from most important to least important. Computations with the smallest cutoffs (largest structures) unveil the possible effects of the chemical groups near the reactive site that can stabilize the transition state or lower the energy level and accelerate the reaction. However, these overlapping phenomena proved to be quite challenging to analyze. Expanding the size of a reactive system in DFT computations must be approached with care. A simulation more representative of your real system can offer insights into the behavior of the system. The drawbacks are losing generality and, of course, a significant increase in computational cost..

■ ASSOCIATED CONTENT

Ⓢ Supporting Information
The Supporting Information is available free of charge at https://pubs.acs.org/doi/10.1021/acsomega.1c03229.

> All final structures in Maestro.mae format (ZIP)
> Overview of the comparative trials with other functionals than B3LYP-D3 (PDF)

■ AUTHOR INFORMATION

Corresponding Author
   Pekka V. Laurikainen − *Faculty of Engineering and Natural Sciences, Tampere University, FI-33014 Tampere, Finland;*
   ⓘ orcid.org/0000-0002-1918-2436;
   Email: pekka.laurikainen@tuni.fi

Author
   Essi L. Sarlin − *Faculty of Engineering and Natural Sciences, Tampere University, FI-33014 Tampere, Finland*

Complete contact information is available at:
https://pubs.acs.org/10.1021/acsomega.1c03229

Author Contributions
P.L.: conceptualization, methodology, formal analysis, investigation, data curation, visualization, and writing—original draft—review and editing. E.S.: conceptualization, resources, writing—review and editing, and supervision.

Notes
The authors declare no competing financial interest.

■ ACKNOWLEDGMENTS

REFERENCES

(1) Cole, K. C. A new approach to modeling the cure kinetics of epoxy/amine thermosetting resins. 1. Mathematical development. *Macromolecules* **1991**, *24*, 3093−3097.

(2) Hardis, R.; Jessop, J. L. P.; Peters, F. E.; Kessler, M. R. Cure kinetics characterization and monitoring of an epoxy resin using DSC, Raman spectroscopy, and DEA. *Composites, Part A* **2013**, *49*, 100−108.

(3) Estridge, C. E. The effects of competitive primary and secondary amine reactivity on the structural evolution and properties of an epoxy thermoset resin during cure: A molecular dynamics study. *Polymer* **2018**, *141*, 12−20.

(4) Mercier, J.; Bunsell, A.; Castaing, P.; Renard, J. Characterisation and modelling of aging of composites. *Composites, Part A* **2008**, *39*, 428−438.

(5) Zhavoronok, E. S.; Senchikhin, I. N.; Roldughin, V. I. Physical aging and relaxation processes in epoxy systems. *Polym. Sci., Ser. A* **2017**, *59*, 159−192.

(6) Komarov, P. V.; Yu-Tsung, C.; Shih-Ming, C.; Khalatur, P. G.; Reineker, P. Highly Cross-Linked Epoxy Resins: An Atomistic Molecular Dynamics Simulation Combined with a Mapping/Reverse Mapping Procedure. *Macromolecules* **2007**, *40*, 8104−8113.

(7) Eyckens, D. J.; Demir, B.; Randall, J. D.; Gengenbach, T. R.; Servinis, L.; Walsh, T. R.; Henderson, L. C. Using molecular entanglement as a strategy to enhance carbon fiber-epoxy composite interfaces. *Compos. Sci. Technol.* **2020**, *196*, 108225.

(8) Soni, N. J.; Lin, P.-H.; Khare, R. Effect of cross-linker length on the thermal and volumetric properties of cross-linked epoxy networks: A molecular simulation study. *Polymer* **2012**, *53*, 1015−1019.

(9) Auvergne, R.; Caillol, S.; David, G.; Boutevin, B.; Pascault, J.-P. Biobased Thermosetting Epoxy: Present and Future. *Chem. Rev.* **2014**, *114*, 1082−1115 PMID: 24125074.

(10) Froidevaux, V.; Negrell, C.; Caillol, S.; Pascault, J.-P.; Boutevin, B. Biobased Amines: From Synthesis to Polymers; Present and Future. *Chem. Rev.* **2016**, *116*, 14181−14224 PMID: 27809503.

(11) Ehlers, J.-E.; Rondan, N. G.; Huynh, L. K.; Pham, H.; Marks, M.; Truong, T. N. Theoretical Study on Mechanisms of the Epoxy−Amine Curing Reaction. *Macromolecules* **2007**, *40*, 4370−4377.

(12) Swier, S.; Van Assche, G.; Vuchelen, W.; Van Mele, B. Role of Complex Formation in the Polymerization Kinetics of Modified Epoxy−Amine Systems. *Macromolecules* **2005**, *38*, 2281−2288.

(13) Raman, V. I.; Palmese, G. R. Influence of Tetrahydrofuran on Epoxy−Amine Polymerization. *Macromolecules* **2005**, *38*, 6923−6930.

(14) Mora, A.-S.; Tayouo, R.; Boutevin, B.; David, G.; Caillol, S. A perspective approach on the amine reactivity and the hydrogen bonds effect on epoxy-amine systems. *Eur. Polym. J.* **2020**, *123*, 109460.

(15) Okumoto, S.; Yamabe, S. Computational study of epoxy-amine reactions. *J. Comput. Chem.* **2003**, *24*, 244−253.

(16) Ren, Y.; Yamataka, H. The α-Effect in Gas-Phase SN2 Reactions: Existence and the Origin of the Effect. *J. Org. Chem.* **2007**, *72*, 5660−5667 PMID: 17590049.

(17) Nigst, T. A.; Antipova, A.; Mayr, H. Nucleophilic Reactivities of Hydrazines and Amines: The Futile Search for the α-Effect in Hydrazine Reactivities. *J. Org. Chem.* **2012**, *77*, 8142−8155 PMID: 22950800.

(18) Juaristi, E.; dos Passos Gomes, G.; Terent'ev, A. O.; Notario, R.; Alabugin, I. V. Stereoelectronic Interactions as a Probe for the Existence of the Intramolecular α-Effect. *J. Am. Chem. Soc.* **2017**, *139*, 10799−10813 PMID: 28701041.

(19) Bochevarov, A. D.; Harder, E.; Hughes, T. F.; Greenwood, J. R.; Braden, D. A.; Philipp, D. M.; Rinaldo, D.; Halls, M. D.; Zhang, J.; Friesner, R. A. Jaguar: A high-performance quantum chemistry software program with strengths in life and materials sciences. *Int. J. Quantum Chem.* **2013**, *113*, 2110−2142.

(20) Alipour, M. Gauging the performance of some density functionals including dispersion and nonlocal corrections for relative energies of water 20-mers. *J. Mol. Graphics Modell.* **2017**, *75*, 132−136.

(21) Zheng, D.; Wang, F. Performing Molecular Dynamics Simulations and Computing Hydration Free Energies on the B3LYP-D3(BJ) Potential Energy Surface with Adaptive Force Matching: A Benchmark Study with Seven Alcohols and One Amine. *ACS Phys. Chem. Au*, **2021**, *0*( ). null. DOI: 10.1021/acsphyschemau.1c00006

(22) Grimme, S.; Ehrlich, S.; Goerigk, L. Effect of the damping function in dispersion corrected density functional theory. *J. Comput. Chem.* **2011**, *32*, 1456−1465.

(23) Roos, K.; Wu, C.; Damm, W.; Reboul, M.; Stevenson, J. M.; Lu, C.; Dahlgren, M. K.; Mondal, S.; Chen, W.; Wang, L.; Abel, R.; Friesner, R. A.; Harder, E. D. OPLS3e: Extending Force Field Coverage for Drug-Like Small Molecules. *J. Chem. Theory Comput.* **2019**, *15*, 1863−1874 PMID: 30768902.

(24) Brinkley, R. L.; Gupta, R. B. Hydrogen bonding with aromatic rings. *AIChE J.* **2001**, *47*, 948−953.

PUBLICATION

IV
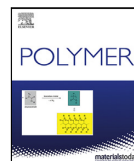
Length-scale discrepancy in the properties of epoxy resin specimens
P. Laurikainen, S. Bhusare, G. Mohanty and E. Sarlin

Length-scale discrepancy in the properties of epoxy resin specimens

P. Laurikainen [*], S. Bhusare, G. Mohanty, E. Sarlin

Tampere University, Faculty of Engineering and Natural Sciences, PO Box 589, FI-33014, Finland

ARTICLE INFO

ABSTRACT

In studies of the fibre-matrix interphase with microscale single fibre methods, the dependence of results on conversion of the thermoset resin – or degree of cure as it is often called – remains an issue. In the microbond method specifically, the curing of picolitre volume drop-on-fibre systems differs significantly from that of macroscale resin batches. The surface-to-volume ratio and vapour pressure can cause volatile components of the resin to evaporate, potentially limiting the degree of cure. Atomistic scale modelling along with experimental thermal analysis were used to understand the curing process and how it translates to resin properties, while nanoindentation was used to experimentally compare the mechanical performance of samples prepared in different length-scales. The evaporation is experimentally verified. Comparable variation in mechanical properties is shown in atomistic scale models of the epoxy network with no evaporation. The origin is in the network morphologies created by varying the curing process. Thus attributing the length-scale discrepancy solely to conversion is likely an oversimplification and understanding the network morphology from different curing conditions is also needed.

1. Introduction

While microscale testing methods are quite widely used for characterising the composite interphase, the discussion surrounding different approaches and the analysis of the results has been conflicted. Several reliable concepts for testing systems have been proposed [1–4], each with their own strengths and drawbacks. Many of the latter relate to the time, effort and reliability of preparing the prerequisite microcomposite samples. The scientific discussion, however, tends to revolve around the theory and physical relevance of the measured results, spanning from the reliability of the analytical methods to problems related to the performance, and length-scale related differences of the samples compared to macroscopic composite laminates and structures.

For the microbond test [1,3], the biggest problems are related to the drop-on-fibre sample preparation, more precisely to the curing of the thermoset resin droplets [5,6]. Generally the embedded length of these droplets ranges from tens to hundreds of micrometers. In such samples, the total volume of the resin is in the range of picolitres, while the surface area ranges in thousands of square micrometers. Thus, it can be expected for the curing process to be hindered by various surface related physico-chemical phenomena — many of which correlate with the surface-to-volume ratio. Significant surface-to-volume ratios are rarely present in macroscale resin or composite samples making these phenomena in most cases insignificant at larger length-scales. Similar problems are also encountered with the oxidisation and crystallisation

of thermoplastic resin droplets, but are outside the current scope for this study.

Zinck et al. [7] have shown that epoxy matrix in microcomposite samples differs from bulk and that, due to the more ductile behaviour of the resin, plastic deformation plays a significant role in microbond testing. Similarly, Rahmani et al. [8] showed that altering the cure cycle affects the results of the microbond test results, especially if the degree of cure is below a specific threshold (approx. 80% achievable maximum for the resin used in the study). Both of these studies largely ignore the massive length-scale difference between bulk scale samples used to study resin properties and the microdroplets they supposedly represent. Zinck et al. [7] acknowledged the possibility of volatile evaporation as a complication for microdroplet curing. Rao and Drzal [5] studied the glass transition temperature of microcomposite samples and noted significant differences with resins that also correlate with the molecular weight, and thus volatility, of the resin components. Evaporation of small molecular weight components from the reactive mixture can limit the achievable degree of cure either through uneven stoichiometry for epoxies [5,9–12], or (localised) depletion of styrene from polyester and vinyl ester resins [13].

Thomason [13] recently reviewed many of the length-scale related problems in microdroplet preparation and highlighted the vapour pressure of the various resin components, which can include various small molecular weight organic molecules such as amines, styrene, epoxides,

anhydrides and alcohols. Moisture content of the droplet was also pointed out as a potential problematic parameter of the curing process and microdroplet properties [13]. His overview concluded that after a suitably high degree of cure – if achieved – the effect of the degree of cure on the microbond test results becomes almost negligible. This conclusion is also supported by finite element (FE) simulations of the role of resin mechanical properties in the test [14].

Other studies on thermoset epoxy resins have highlighted the possible formation of different nanoscale morphology or nanostrucutres in the resin [9,11,15–18]. The core concept being that under specific conditions – or when using certain chemical components in the resin mixture – the epoxy can form regions of high crosslink density connected with regions of significantly less of crosslinks. This would result in materials, with very different properties despite a similar average conversion, and which exhibit varying contributions of solid-like and liquid-like properties [17]. Experimental evidence of length-scale related discrepancy in mechanical performance has also been noted outside the expected probability of encountering defects as damage initiation sites [19].

More general studies on epoxy curing tend to focus either on computational methods [20,21] or experimental methods, such as differential scanning calorimetry (DSC) [22,23] and rheometry [24]. These established approaches suffer from significant gaps in length-scale evoking a question how to attempt a comprehensive approach by combining the methods. The curing process is a complex physico-chemical process involving reaction energetics, molecular mobility, network morphology and surface related effects such as the aforementioned evaporation. Currently no computational method can cover all of these, especially in a single simulation, mainly due to the very different length-scale – and the accompanying system size dependent computational cost – associated with each phenomenon. Conversely, a majority of experimental methods, whether aimed for reaction energetics or physical properties utilise samples with dimensions in the millimetre scale or higher. Bridging these gaps, i.e. figuring out the connections between molecular simulations and experimental methods, is a massive ongoing challenge in the field. Unger et al. [12] compared iterative Molecular Dynamics (MD) crosslinking simulations with near-IR spectroscopy based monitoring of the curing process and found the model to fit experimental data reasonably well. For amine-cured epoxies, a more representative crosslinking simulation can be achieved by determining the relative reaction rates for the primary and secondary reactions to be used as and additional parameter for selection of crosslinking sites [21]. The implementation of a reactive force-field [25] or reactive model [26] can improve the simulations further. Recent efforts to parametrise and utilise such force-fields for crosslinked polymer systems are showing promising results for both bond formation and bond dissociation [27–29] but at a high computational cost.

Nanoindentation has proved a powerful tool for studying the mechanical properties of crosslinked polymer samples that are otherwise difficult to measure, such as thin films [30,31]. Ligot et al. [31] discuss in detail the effects the conversion and sample characteristics have on the results. Hardness, modulus, their ratio and the viscoelastic and creep behaviours are all shown to change with crosslinking as expected. Thin samples on a substrate can show effects from the substrate if the indentation depth is too deep and conversely various sample surface related effects are discussed, at least briefly. Of special interest are results with lower crosslinking degree exhibiting higher stiffness, which were attributed to molecular mobility and/or atmospheric surface effects [31].

In this study, the conversion of unreacted epoxy and amine to the crosslinked epoxy network was explored with atomistic scale simulations for a simple commercial epoxy resin system to estimate the role of conversion to the measurable material properties such as elastic modulus. The simulation outputs were compared to experimental results from macroscale samples with dimensions in the range of several millimetres, and from microscale drop-on-fibre samples with a

high surface-to-volume ratio. Nanoindentation was used as the primary method for experimental characterisation of the resin mechanical properties. Thermal analysis methods, such as differential scanning calorimetry (DSC) and Fourier transform infrared spectroscopy coupled thermogravimetric analysis (TGA-FTIR) were used to empirically study the curing process and any related evaporation of volatiles. These samples were considered as representative of the macroscale behaviour only. This combined methodology was intended to explore the role of conversion – degree of cure – to the microdroplet sample behaviour and further elucidate some of the issues faced when preparing such samples. The hypothesis that the evaporation is not the only reason for the length-scale discrepancy was explored by mitigating its role whenever possible outside the TGA-FTIR measurements specifically intended for studying it.

2. Experimental

2.1. Materials

The resin system used for the experiments was EPON 828 cured with Jeffamine D–230 provided by Huntsman. The EPON 828 resin is a diglycidyl ether of bisphenol–A (DGEBA) epoxy resin with an epoxy equivalent weight of around 190 g/mol [32]. Jeffamine D–230 is poly(oxypropylene) diamine hardener with an average repeating unit count of approximately 2.5 and an amine hydrogen equivalent weight of 60 g/mol [33] subsequently denoted as polyetheramine (PEA). The schematic structures of the molecules are presented in Fig. 1. The stoichiometric mixing ratio is 100:32 by weight. All resin batches were mixed with high shear speeds until visually determined as homogeneous, the actual mixing time depended on batch volume. After mixing the batch was placed in vacuum for 3 min for gas removal.

Macroscopic samples were prepared by casting the resin in open top moulds and cured accordingly to their respective curing cycles denoted in the sample name: Bulk RT cured for 24 h at room temperature, Bulk 50 for 8 h at 50 °C, Bulk 80 (and Bulk ref) for 8 h at 80 °C and the Bulk RT-50 and Bulk RT-80 combinations of the previous. Microdroplet specimens were prepared as in previous studies featuring the microbond method [3,14,34] resulting in drop-on-fibre samples with embedded lengths ranging between 60 and 200 μm and cured for 8 h at 80 °C. While waiting for indentation the samples were kept in a controlled environment at room temperature in sample storage cabinet intended for storing electron microscopy samples.

2.2. Experimental methods

Thermogravimetric analysis (TGA) utilised a Netzsch TG 209F3 *Tarsus* (NETZSCH-Gerätebau GmbH, Germany) coupled to a Bruker Tensor 27 FTIR (Bruker, Germany). TGA measurements were conducted for an unreacted resin mixture and the components of the resin mixture separately. A coupling to the FTIR was included to analyse any evaporating species for their chemical composition. This coupled analysis was used to identify whether the PEA, DGEBA or a combination of the two is primarily evaporated from the resin mixture during the cure cycle. A dynamic heating step was used in the test from −20 to 350 °C with a heating rate of 10 K/min.

Differential scanning calorimetry (DSC) was used to analyse the degree of cure of the bulk resin samples. Dynamic heating from −20 °C to 300 °C was used to determine the glass transition temperature (T_g) from the initial curing and to determine the residual curing enthalpy. The samples were then cooled to −20 °C followed by another dynamic heating step from −20 to 300 °C to ensure no residual reactive potential and that the glass transition matches the fully cured state. Total curing enthalpy was determined by using the same heating steps for an uncured resin mixture. Comparing the residual enthalpy to the total enthalpy of the uncured systems enables the determination of degree of cure relative to the practical maximum, which is rarely equal to
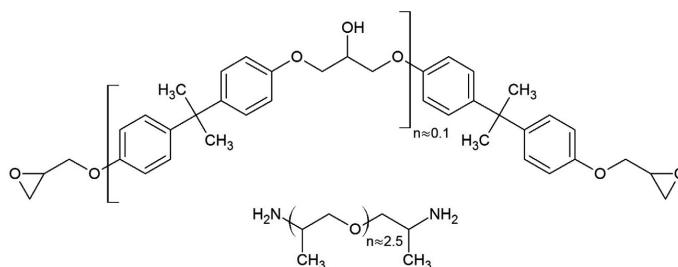
Fig. 1. DGEBA and PEA comprising the epoxy system used in this study. The repeating unit numbers are representative of the used grades.

the theoretical maximum determined by the stoichiometric amount of functional groups due to very restricted molecular mobility at the later stages of cure [24].

Nanointendation tests were carried out with an Alemnis in-situ nanoindenter (Alemnis AG, Switzerland) integrated inside a Scanning Electron Microscope (SEM, Zeiss LEO 1450, Germany). A cube corner pyramidal tip was used for all the indentations performed in this study. Cube corner tip has a smaller included angle and hence, provides better viewing angle for tip positioning on the microdroplet samples compared to the widely used Berkovich tip.

The indents comprised loading, peak hold and unloading segments. Except for the peak hold segment, which was load controlled, all other segments were in displacement-controlled mode [35]. Loading and unloading segments were performed in constant indentation strain rate of 0.6 s^{-1}. In pyramidal indentation, constant indentation strain rate is achieved by maintaining the ratio of instant indentation speed to the instantaneous depth constant [35]. Indentation depth was set to 1.2 μm after contact load of 0.5 mN, which rests in total indentation depths of 1.4 μm. After attaining peak displacement during loading segment, the load was held constant for 3 s to allow the material to creep at peak hold segment. This was followed by constant strain rate unloading from the sample surface. At least 10 indents were performed on each Bulk sample and 3 indents were performed on each microdroplet. The whole loading/unloading cycles were done in less than 30 s. The indentation sites were selected from the thickest parts of the microdroplet to avoid any elastic influence from the fibre and to have the indenter tip oriented as close to the normal of the droplet surface as possible. The load–displacement data from each indentation was analysed with the Oliver-Pharr method [36] to estimate resin modulus and hardness and a minimum of three indents was done to each droplet to ensure consistency. The imaging during indentation used a LaB6 filament with 3.0 kV accelerating voltage. The accelerating voltage was kept low to avoid charging or other interaction with the sample.

3. Computational methods

The molecular network of the DGEBA epoxy and PEA hardener (see Fig. 1) system was modelled in the Maestro graphical interface of the Schrödinger Materials Suite (version 2023-1). The molecular dynamics (MD) calculations used established workflows with the Desmond/GPU code, capable of utilising the high level of parallelisation offered by modern graphical processing units (GPUs) [37]. The current version of the OPLS4 force-field [38–41] was used in all simulations. The overall simulation work comprised the following steps (number of simulation boxes after the simulation steps given in parentheses): Disordered system builder for creating the initial simulation boxes (5), Relaxation to equilibrate the simulation boxes (5), Crosslink polymers simulations to create crosslinked networks with various degrees of conversion (25), stress–strain simulations of the crosslinked networks (25).

To match the epoxy and amine hydrogen equivalent weights provided by the material manufacturers technical data sheets, a mixture

Table 1
Molecules used to create the simulation boxes for the epoxy resin simulations, the value n signifies repeating unit count. For the chemical structures of the components, refer to Fig. 1. The equivalent weight column refers to the epoxy equivalent weight and amine hydrogen equivalent weights of the mixture of different molecular weight components with the datasheet reference value in parentheses [32,33].

Component	MW [g/mol]	Input molecules	Eq. weight [g/mol]
DGEBA, n=0	340.4	112	187.8 (185–192)
DGEBA, n=1	624.8	16	
PEA, n=2	190.3	14	59.1 (60)
PEA, n=3	248.4	50	

of two structures for both epoxy and amine component was selected. The simulations began from the creation of five parallel simulation boxes with the Disordered system builder, through random snapped to grid placement molecules near the centre of the simulation box (steric packing) with van der Waals radii scaling factor of 0.5 to avoid overlaps. After placing the atoms, the simulation box was finalised with 3D orthorhombic periodic boundary conditions. The input molecules and the specific amount of each molecular structure input into the simulation boxes are presented in Table 1.

The simulation boxes were relaxed through a multistep relaxation workflow comprising a total of 8 simulations described in detail in supplementary data S1. All simulations used the Nose–Hoover chain thermostat with a relaxation time of 1 ps and the NPT ensembles utilised the Martyna-Tobias-Klein barostat with isotropic coupling and a relaxation time of 2 ps. The dimensions of the simulation boxes, along with the equilibrated densities of the relaxed simulation boxes, are presented in supplementary data S1.

To create crosslinked networks, the simulation boxes were input to a Crosslink Polymers workflow. This Desmond/GPU workflow is a phenomenological, qualitative model that, instead of attempting to simulate real curing kinetics, forms crosslinks based on the following input criteria: maximum number of crosslinks per iteration, reaction threshold distance and the temperature dependent relative probabilities of the defined reactions. The reaction thresholds were cut-off distances in Ångstroms outside of which a complementary reactive site does not qualify for the reaction, set to 7 Å. The reaction probabilities were computed by the software based on primary and secondary amine reaction activation energies similarly to normalised Bolzmann factors, with the assumption there were no other energy states in the system than the reactions defined in the simulation input.

After forming a set of crosslinks based on the aforementioned criteria, the simulation boxes were equilibrated with MD for 50 ns NPT ensemble at 1.01325 bar. The thermostat target temperature is dependent on the iteration. All simulations (except T$_{max}$ = 300 K) included a simulated heating cycle of increasing temperature by 6.25 K per iteration up to T$_{max}$ followed by decreasing temperature by 6.25 K per iteration until it reaches 300 K or the simulation ends. This change in temperature affects both the probabilities of the defined reactions and the thermostat target temperature for the MD simulation. T$_{max}$

values were selected as 300 K, 400 K, 500 K, 600 K and 700 K to a total of five different average degrees of conversion with 5 parallel simulation boxes for each. These iterations were continued until one of the following conditions was met: the desired degree of conversion is reached or 20 consecutive iterations fail to form crosslinks — because no structures in the simulation box fulfil the defined criteria. The target conversion was set as 100% epoxide functionality, effectively causing the 20 iterations to be the only relevant end criterion. All temperature ramps were simulated starting from 300 K with the same "heating rate", up to a maximum temperature and back to 300 K, to create simulation boxes with different degrees of conversion by varying the maximum temperature. If the temperature ramp ended before the simulation end-criteria were met the iterations continued at 298.15 K. The primary purpose of the workflow was the creation of reasonably representative crosslinked structures for inputs to the stress–strain calculations. It was, however, also expected to provide some qualitative insight into the molecular mobility dependent kinetics at later stages of the crosslinking process.

The stress–strain calculation, in turn, incrementally deformed the simulation box and used Desmond/GPU to examine the system response to this strain from 1.5 ns NVT ensemble at 300 K simulations and recorded the pressure tensor at 5 ps intervals. Trajectory recording interval was set at 10 ps and stress was calculated from the last 20% of the trajectory. Strain rate was determined from the strain step size ($\Delta \varepsilon_1 = -0.0015$) and simulation time (1.5 ns) resulting in a strain rate of 10^6 s^{-1}. Strain type was set as increased dilatation ($\eta = 0.33$). Further description on how these strain steps translate to simulation box deformations, and to the effective strain (and stress) reported in the results, are presented in supplementary data S1. To examine the effect of strain rate on the simulation result, the simulation for the $T_{max} = 600$ K crosslinked networks was repeated with a strain rate of 10^7 s^{-1} – achieved by reducing the simulation time of the NVT ensemble to 150 ps.

No changes in chemical bonding were allowed in the stress–strain simulations, due to the non-reactive nature of the OPLS4 force-field. Covalent bonds were instead stretched according to their force-field determined potential until the simulation ends. This can cause erroneous results as eventually the energy needed to stretch a bond becomes extremely high. To mitigate this issue, compression was used as the primary mode of deformation and the maximum strain was kept low (<20%). Cyclic stress–strain simulation mode was enabled to provide results similar to the nanoindentation tests. The overall strain profile was set as 120 steps of compression followed by a single unloading/loading cycle with 80 simulation steps each. Results such as modulus and residual strain were analysed from the unloading cycle for consistency with the nanoindentation results.

4. Results and discussion

Volatile evaporation is the most commonly cited explanation to the difference in final conversion between samples of different length-scales. To study the phenomenon, a cooled resin mixture was inserted into a TGA coupled to an FTIR to analyse the chemical composition of any gasses evaporating during a controlled heating cycle. The results are presented in Fig. 2.

It is clear from the results that evaporation starts at relatively mild temperatures and based on the vibrations in the IR spectrum the volatile component evaporating is, as expected, the PEA hardener. From a sample inserted into the TGA, with volume in microlitres and open surface area around one millimeter squared, the evaporation is quite low as indicated by the low absorbance values, but detectable even from a larger sample batch such as this. A microdroplet has significantly higher relative surface area and the associated increase in vapour pressure likely both lowers the T_{onset} and increases the intensity of the evaporation. As the heating of the sample is carried out until 350 °C the thermal degradation of the sample contributes to

Table 2
Overview of DSC measurements of the epoxy resin system at different degrees of conversion. Measured from samples corresponding to those used in nanoindentation.

Sample	Enthalpy [J/g]	T_g [°C]	Degree of cure [%]
Bulk RT	42.64	57.1	91.8
Bulk 50	35.3	61.9	93.2
Bulk RT-50	13.3	53.6	97.4
Bulk 80	3.54	83.5	99.3
Bulk RT-80	1.56	82.6	99.7

the detected gasses. However, the CO_2 associated vibrations around 2400 cm^{-1} can be used to estimate when this degradation starts and these vibrations are detected to any significant degree only after a temperature of over 200 °C – well after the onset of the vibrations associated with the evaporation. Therefore, the TGA-FTIR measurement conclusively proves the role of hardener evaporation to the curing of the resin, at least for this epoxy — hardener combination. To support this result, the TGA-FTIR measurements were performed for samples comprising only one of the resin components at a time. These results are presented in supplementary data S2.

Dynamic DSC heating runs were used to study the conversion of the physical samples used as a point of comparison for the MD. Conversion analysed via DSC is discussed as degree of cure to differentiate it from the stoichiometric conversion discussed with the simulations. The degree of cure is determined based on the residual curing enthalpy compared to the total reaction enthalpy of the uncured resin. Pieces of the same bulk samples used for nanoindentation were subjected to two dynamic DSC heating steps to estimate the conversion. Care was taken, similarly to the nanoindentation samples, to measure an internal portion of the cured volume — both to strengthen the correlation with the nanoindentation and to minimise the contributions of evaporation. The conversion was analysed through comparison with the total reaction exotherm of a uncured resin sample, which was using the same DSC parameters determined as 520.6 J/g. After two heating cycles all samples exhibited a similar ultimate T_g of 86.1 ± 1.9 °C. The results of the DSC analysis of the Bulk samples are presented in Table 2.

Nanoindentation was utilised to characterise the mechanical properties of microdroplets directly. The results from microdroplets were compared to the larger Bulk samples prepared from the same mixing batches. The modulus and hardness values along with analysed elastic and plastic energies from the indentation are presented in Table 3. Examples of SEM images and analysis plots are presented in supplementary data S3. The results immediately highlight the quite significant difference between the Bulk and droplet samples. Unfortunately, no direct comparison between the modulus and harness values of two sample types was found based on the results. Some of the common trends can still offer qualitative insights into the behaviour of the epoxy resin at different length-scales. Higher modulus values at lower degree of cure have been previously reported [31] and shown to be especially prominent as a sample surface phenomenon (shallow indentation depth). Similar results are shown here but cannot be – at least fully – attributed to surface effects. The Bulk samples were indented on a polished cross-sectional surface – mitigating the effects of evaporation – with a total indentation depth of over 1 µm as described earlier. Such effects could, however, contribute to the droplet results and the all-round higher measured modulus and hardness values they exhibit as the droplets are indented on their exposed surface.

The samples in Table 3 include two separate batches of samples, the first – done more as proof of concept – included 3 droplet samples and 1 large bulk resin sample cured 8 h at 80 °C. The samples were prepared identically in each case, except for the fact that the "Bulk ref" sample was not indented from a cut cross section but rather the closed mould surface. This might explain why the sample behaviour differs form all others especially in terms of the relative plastic/elastic indentation energies. The main difference of the two sample batches
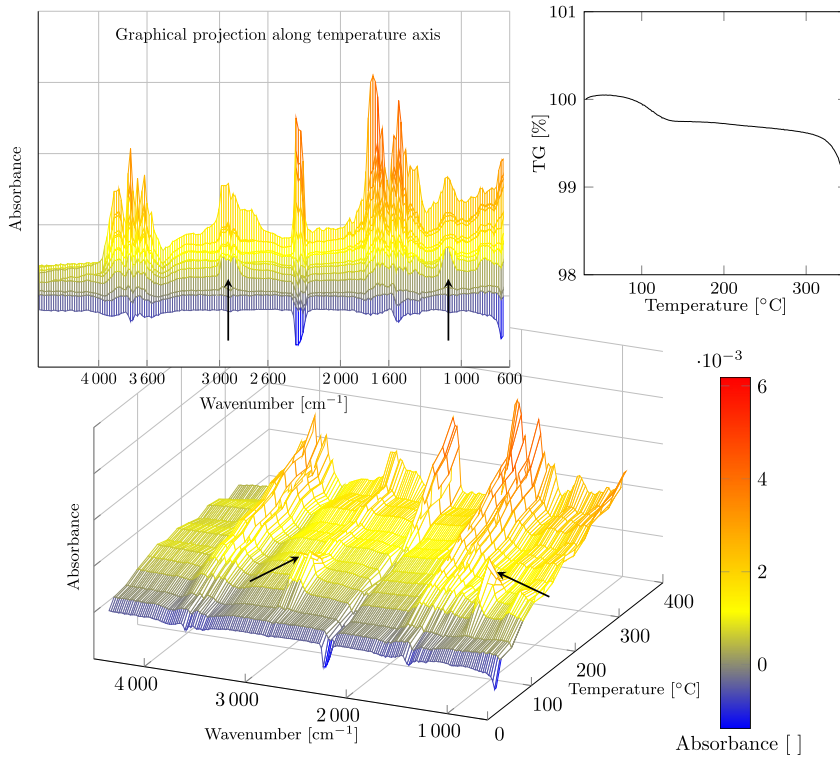
Fig. 2. FTIR coupled TGA measurement of the uncured resin mixture. The corresponding TGA result shown for reference. Arrows in the Figure indicate FTIR signals of evaporating hardener starting at $T_{onset} \approx 85 \,°C$.

Table 3
Overview of the nanoindentation results from different samples. Results represent the average of three indentations per sample.

Sample	Hardness [MPa]	Modulus [GPa]	Hard./Mod. [MPa/MPa]	Plastic [%]	Elastic [%]
Droplet 1[a]	302.8 ± 13.3	5.23 ± 0.12	0.058 ± 0.002	84.99	15.01
Droplet 2[a]	343.5 ± 20.6	5.47 ± 0.15	0.063 ± 0.002	84.20	15.80
Droplet 3[a]	235.0 ± 8.6	4.92 ± 0.33	0.048 ± 0.003	87.74	12.26
Droplet 4	391.1 ± 20.5	5.30 ± 0.12	0.069 ± 0.003	87.12	12.88
Droplet 5	361.4 ± 7.1	4.92 ± 0.09	0.074 ± 0.001	85.94	14.06
Droplet 6	365.4 ± 11.2	5.15 ± 0.24	0.069 ± 0.004	86.63	13.37
Droplet 7	351.9 ± 21.0	5.12 ± 0.14	0.074 ± 0.003	86.66	13.34
Droplet 8	347.7 ± 3.6	4.70 ± 0.04	0.073 ± 0.003	86.28	13.72
Droplet 9	346.1 ± 17.5	5.00 ± 0.10	0.071 ± 0.003	86.86	13.14
Bulk ref[a]	281.1 ± 8.3	4.19 ± 0.08	0.067 ± 0.003	79.52	20.48
Bulk RT	279.1 ± 7.1	4.37 ± 0.12	0.064 ± 0.002	85.44	14.56
Bulk 50	271.8 ± 15.6	4.36 ± 0.20	0.062 ± 0.002	85.74	14.26
Bulk RT-50	274.0 ± 4.8	4.40 ± 0.09	0.063 ± 0.002	84.55	15.45
Bulk 80	272.5 ± 7.4	3.95 ± 0.07	0.069 ± 0.003	83.19	16.81

[a] Earlier batch of samples.

is, however, the time-frame of the measurement. Bulk ref and droplets 1–3 were tested within a month of mixing the resin and creation of the samples. For the rest there was an approximately 6 month wait from mixing and curing the resin to the actual testing. This explains especially the high mechanical performance of the Bulk RT sample, that has had plenty of time to post-cure during the 5–6 month window.

The best match between the macroscale Bulk samples and Droplets 4–9 was found based on the hardness/modulus ratio [31], which is consistently high for all droplets (average value 0.071 ± 0.004 MPa/MPa).

The Bulk 80 sample, exhibits the similar – if slightly lower – ratio of 0.069 ± 0.003. The Bulk RT, Bulk 50 and Bulk RT-50 samples have average ratio of 0.063 ± 0.002. Therefore, the droplets should have an approximate degree of cure ⩾95% even considering evaporation and surface related effects. However, the hardness/modulus ratio of the earlier batch of droplets (Droplets 1–3) was significantly lower, only 0.056 ± 0.006, while for the Bulk ref sample the ratio was only slightly lower than the correspondingly cured Bulk 80 sample (0.067 ± 0.003). This would indicate that the degree of cure of the freshly prepared droplets was much lower, likely ⩽90%, and that post-curing and storage affect the droplets significantly, which is unsurprising but warrants further investigation. The testing of such samples should be at least timed consistently with the sample preparation.

MD simulations were used to study the effect of conversion of the resin system to its properties. In terms of conversion, the gel-point represents the biggest single change in properties. Another closely related term is known as vitrification and while the two are related the distinction is based on the observable change in behaviour. Gel point signifies the formation of an infinite polymer network and change from liquid-like to solid-like dominated behaviour. The classical theory for gel point determination is given by the Flory–Stockmayer theory [42,43], which gives the simulated systems described in Table 1 an estimated gel point of 56.4%. From the simulations, the gel point is determined either from the inflection point of the largest reduced molecular weight or from the maximum of the reduced molecular weight excluding the largest [25]. Both are proposed as representative points for the creation of a molecule percolating throughout the simulation box [25]. Examples these behaviours are presented in supplementary data S4 as
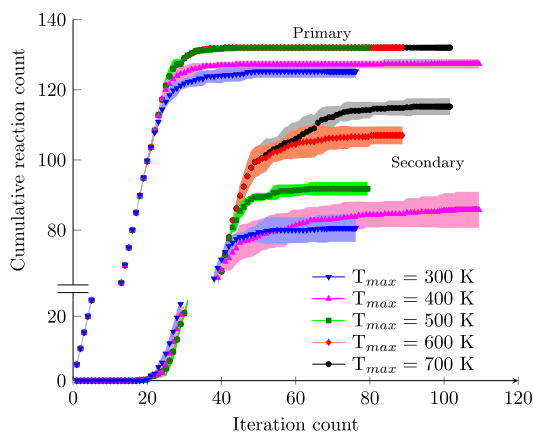
Fig. 3. Primary and secondary amine reactions during crosslinking simulations. Heating cycle simulations 300 K to T_{max}. The scatter plot represents the average and the shaded area the standard deviation of 5 parallel simulations.

Table 4

Overview of MD simulations of the epoxy resin system at different degrees of conversion. All values represent the average of 5 parallel simulations.

T_{max} [K]	Conversion [%]	Modulus [GPa]	Residual strain [%]
300	81.7 ± 1.7	3.25 ± 0.84	10.6 ± 1.2
400	84.6 ± 2.4	3.90 ± 0.91	10.6 ± 0.8
500	88.8 ± 0.8	3.55 ± 1.12	9.6 ± 1.2
600	94.8 ± 1.1	3.44 ± 0.87	9.3 ± 0.8
700	98.1 ± 1.0	2.57 ± 1.19	9.4 ± 1.1

first and second largest reduced molecular weight during the simulations. The two methods resulted in different values: the inflection point method resulted in a gel point of 61.6 ± 3.3% while the maximum method a somewhat higher value of 69.7 ± 4.1% conversion — possibly because only the second highest reduced molecular weight is considered instead of the weight-averaged reduced molecular weight. The gel point also represents the lowest conversion where the resin is expected to exhibit the properties of a solid or solid-like material. At lower conversions its physical nature is a high viscosity liquid and therefore conversions lower than the gel point are not worth of note in this context. Vitrification is more related to the onset of glass-like behaviour of the resin and is also temperature dependent (glass transition). Once vitrification occurs molecular mobility becomes almost impossible severely hindering further reactions unless the material is heated above the current glass transition temperature.

In addition to the gel point, monitoring the overall process of the conversion should help understand the formation of the polymer network and the final material properties. To visualise this, the numbers of primary and secondary amine reactions during the crosslinking simulation were monitored and the results are plotted in Fig. 3. In the early iterations in Fig. 3, the crosslinking simulation is representing the overall process poorly. At the early stages of curing the process is controlled by reaction energetics, which the simulation only considers in a probabilistic sense, meaning the early iterations were only limited by the maximum number of reactions allowed per iteration (5). After 16–20 iterations, slight differences between reaction conditions start to form. The cause is a combination of suitably high number of secondary amine moieties, the activation energy based probability criterion between the two amine types and the increasingly hindered molecular mobility due to already formed crosslinks. Gelling occurs around 30–40 iterations, considering the range of results for the gel point, after which molecular mobility becomes an important limitation to the formation of crosslinks and the simulation becomes significantly more realistic. This also coincides with the saturation of the primary amine reactions.

The crosslinking simulations presented above resulted in 25 different crosslinked systems, 5 for each T_{max}, which were treated as parallel samplings of a single average conversion. The crosslinked systems were input into the stress–strain simulations to estimate the mechanical properties vs. conversion behaviour. An example stress strain curve from T_{max} = 700 K simulation box 3 is presented in Fig. 4. This stress strain simulation corresponded well with the average of the five parallel T_{max} = 700 K simulation boxes. The modulus was estimated from the

slope of the unloading curve – marked red in Fig. 4. Residual strain was likewise estimated form the unloading curve as the strain value at which stress is approximately equal to stress at zero strain. Residual strain was used mainly as a qualitative measure for comparison between identically deformed simulation boxes. Table 4 presents the primary outputs representing material performance for these different degrees of conversion.

The simulations predicted similar trends as the nanoindentation: maximum conversion does not result in highest mechanical performance — or at least highest elastic modulus. Perfect agreement with experimental results was not expected as the result of such atomistic simulations is dependent not only on the strain rate and conversion, but also on system size, polymer chain length and entanglement and other similar factors. These last ones comprise the primary motivation for such simulations, allowing the observation of polymer morphology related contributions to observed properties. Based on the simulations, the modulus peaks at approximately 85% of the stoichiometric maximum conversion (T_{max} = 400 K systems). This conversion also represented a significant outlier in the crosslinking simulations shown in Fig. 3. The variation of the results should also be considered an important factor. For example, the average modulus of T_{max} = 700 K systems is only 2.57 GPa but for simulation box 1 the modulus is 4.5 GPa (stress–strain curve presented in supplementary data S4). Conversion is clearly not the most critical factor to the mechanical response of epoxy networks, at least above a certain threshold value.

As expected, strain rate affects these results somewhat. For the T_{max} = 600 K systems repeating the simulations with a reduced MD stage time (150 ps) – increasing the strain rate to 10^{-7} s^{-1} – reduced the average modulus to 3.16 ± 1.41 MPa and the residual strain to approximately 8.6 ± 1.2%. The average plots of the five parallel stress–strain simulations with the two strain rates are presented in supplementary data S5.

Interesting commonalities can also be found between the MD simulations and the nanoindentation results. In both cases, the most aggressive curing conditions – coinciding with the highest conversion – resulted in a lower elastic modulus compared to an 'optimal' curing cycle. Either result alone could be assumed as an erroneous or otherwise uncorrelated result. The MD simulations had very limited volume and likely cannot capture the full complexity of the epoxy morphology [15]. Conversely, the resin mixture placed into an 80 °C oven directly after casting will experience significant volatile evaporation from the open surface. The common trend, despite these differences, implies there is another phenomenon affecting the properties.

One reasonable hypothesis relates to molecular mobility – the gelling and vitrification of the resin – and the resulting morphology of the epoxy network. The maximum achievable conversion is determined by the possibility of the reactive reaching a suitable proximity and orientation. Not only does this always limit the conversion below 100%, but the molecular mobility throughout the curing reaction can change drastically between different curing conditions. For example consider two systems, one with slow conversion and sufficient time to relax internal stresses in the crosslinked network versus a system that reacts rapidly to a high conversion. These systems were exemplified in the atomistic simulations, by many of the T_{max} = 400 K and 700 K
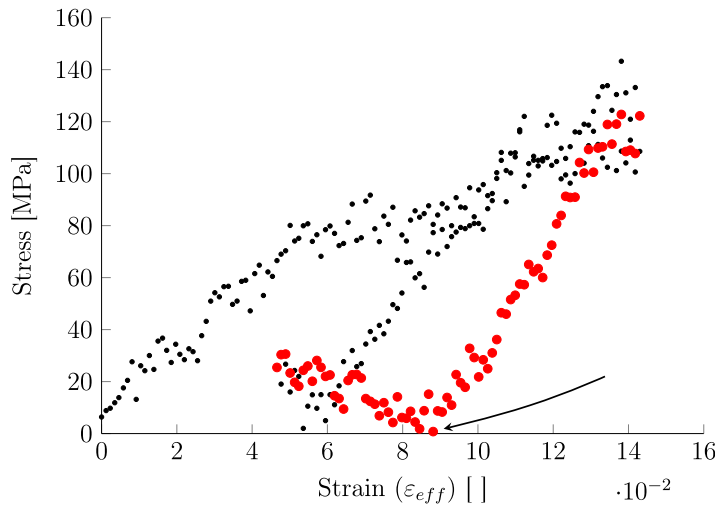
Fig. 4. Stress–strain simulation results for T_{max} = 700 K simulation box 3. The unloading stage of the simulation is highlighted in red. Approximate residual strain is indicated with an arrow. Note that the data includes two loading stages. (For interpretation of the references to colour in this figure legend, the reader is referred to the web version of this article.)
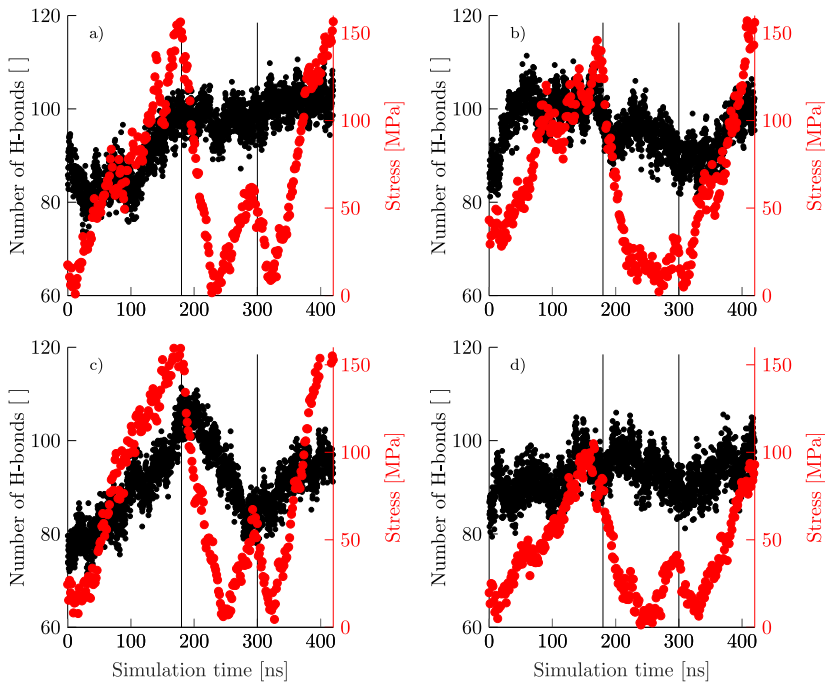

Fig. 5. Potential hydrogen bond interactions during the compressive stress–strain simulations of epoxy resin from selected simulation runs. Stresses are plotted in red for comparison. Vertical lines indicate different cyclic stress–strain stages. (a) T_{max} = 400 K, (b) T_{max} = 500 K, (c) T_{max} = 600 K and (d) T_{max} = 700 K. (For interpretation of the references to colour in this figure legend, the reader is referred to the web version of this article.)

crosslinked networks, respectively, as highlighted by the molecular weight development plots in supplementary data S4.

Additional hints were found based on the hydrogen bonding interactions during the trajectory of the stress–strain simulation. Stress curves representative of the specific conversions from T_{max} = 500–700 K were selected and the estimated amount of hydrogen bonds during the

trajectory are plotted in Fig. 5. The hydrogen bonds were estimated based on the criteria: maximum distance 2.8 Å, Donor minimum angle 120°, Acceptor minimum angle 90°. Aromatic hydrogen bonds are included but the software only considers the aromatic ring as a possible donor. To reduce the scatter in the hydrogen bond estimations a moving average on 5 was used to smooth the data for plotting. For many of
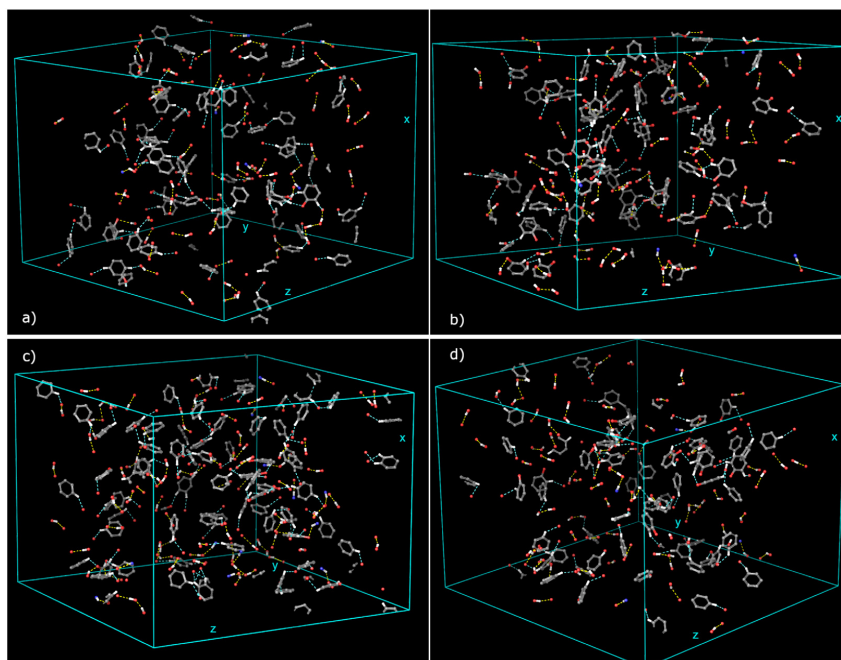
Fig. 6. Visualisation of functional groups participating in hydrogen bonding in the epoxy network during the T_{max} = 600 K simulation box 2 stress–strain simulation. Black areas indicate areas with no H-bonding, not voids (atoms hidden from visualisation). The stress and hydrogen bond counts for this simulation are plotted in Fig. 5(c). Each pane represents a trajectory frame form the simulation: (a) frame 1 (0 ns), (b) frame 10478 (105 ns), (c) frame 18116 (181 ns) and (d) frame 24901 (249 ns).

the simulations, changes in the stress strain behaviour correlate with the predicted hydrogen bonding. Some simulations, however, show less changes in hydrogen bonding – such as Fig. 5(d) – and often also exhibit much lower stress levels during the deformation. While strain is not presented in Fig. 5, the strain in the simulation correlated linearly with simulation time. Unloading started after 180 ns and the second loading cycle after 300 ns.

To explore how this relates to the morphology of the polymer, a selected simulation box (corresponding to Fig. 5(c)) was carefully inspected visually. Four trajectory frames were selected from a single T_{max} = 600 K simulation: the start of the simulation (Frame 1), first notable peak in hydrogen bonding at around 105 ns (Frame 10478), peak load at around 181 ns (Frame 18116) and the minimum load during unloading stage (Frame 24901). These are presented in Fig. 6.

The visualisation reveals specific regions of complex hydrogen bonded networks previously speculated also contributing to the curing kinetics [44]. These complex networks become more prominent with increasing strain and based on the hydrogen bonding — stress comparisons in Fig. 5 contribute to the mechanical response quite significantly. Many of the hydrogen bonds are formed either by aromatic hydrogens or the hydroxyl groups created by the epoxide-amine crosslinking reactions. Both areas of significant hydrogen bonding networks and areas completely without hydrogen bonding can be identified. Further work is needed to verify the result, as it is possible the observed local variations are a system size related anomaly. Nevertheless, considering also the role of the hydrogen bonds with varying conversion indicated in Fig. 5, this could also hint at changes in the epoxy morphology and the role of hydrogen bonding in the overall crosslinked network performance. As the highest stress–strain performance, high hydrogen bond counts and steadily progressing crosslinking simulations all coincide, it is could be that the 'slower' curing enables the epoxy network to orient favourably to maximise the hydrogen bonding contribution to

the mechanical performance, whereas a rapidly vitrified network has no such advantage.

5. Conclusions

The curing of DGEBA based epoxy (EPON 828) with low molecular weight polyether amine hardener (Jeffamine D-230) in microcomposite samples was studied with a multiscale approach combining nanoindentation of macro- and microscale samples, thermal analysis and atomistic simulation. The results indicate the degree of cure of the resin microdroplets was significantly lower than for similarly cured resin, but changes significantly with post-curing over time.

The evaporation of curing agent previously suggested as the cause of the discrepancy in the curing is shown through coupled TGA-FTIR measurement and offers at least a partial explanation. Based on the nanoindentation of samples with different curing cycles – supported by molecular dynamics simulations – the effect of different these curing cycles on the final properties is far from straightforward. This is likely a result of significant differences in the morphology of the epoxy network, which also contributes to the length-scale difference. Based on the stress–strain simulations, a significant portion of the difference can be attributed to differences in hydrogen bonding, which can stabilise the polymer networks with lower conversion leading to more homogeneous, or even improved, mechanical response compared to a rapidly vitrified, high degree of cure polymer network.

The original intent of this study was to find a pathway to evaluate – and hopefully correlate – the microdroplet specimen properties with those of macroscopic samples with similar conversion. However, these results indicate the length-scale discrepancy is unresolvable: the properties of a resin in microcomposite sample will never fully match those of a macroscopic sample, but careful and consistent sample preparation can somewhat mitigate the issue. The results also hint at much more

important concepts. Are the resin properties at different environments, in general, comparable? Is there a difference in the morphology of the resin in a composite compared to unreinforced resin? Answering these questions is crucial not only for improving the microcomposite interfacial tests but also to overall understanding of thermoset resin composites and remain a topic for future study.

CRediT authorship contribution statement

P. Laurikainen: Conceptualization, Methodology, Formal analysis, Investigation, Data curation, Writing – original draft, Writing – review & editing, Visualization. **S. Bhusare:** Conceptualization, Formal analysis, Investigation, Writing – review & editing. **G. Mohanty:** Conceptualization, Methodology, Writing – review & editing, Supervision. **E. Sarlin:** Conceptualization, Resources, Writing – review & editing, Supervision.

Declaration of competing interest

The authors declare that they have no known competing financial interests or personal relationships that could have appeared to influence the work reported in this paper.

Data availability

Data will be made available on request.

Acknowledgements

Appendix A. Supplementary data

Supplementary material related to this article can be found online at https://doi.org/10.1016/j.polymer.2023.126148.

References

[1] B. Miller, P. Muri, L. Rebenfeld, A microbond method for determination of the shear strength of a fiber/resin interface, Compos. Sci. Technol. 28 (1) (1987) 17–32, http://dx.doi.org/10.1016/0266-3538(87)90059-5.

[2] S. Zhandarov, E. Mäder, Peak force as function of the embedded length in pull-out and microbond tests: effect of specimen geometry, J. Adhes. Sci. Technol. 19 (10) (2005) 817–855, http://dx.doi.org/10.1163/1568561054929937.

[3] P. Laurikainen, M. Kakkonen, M. von Essen, O. Tanhuanpää, P. Kallio, E. Sarlin, Identification and compensation of error sources in the microbond test utilising a reliable high-throughput device, Composites A 137 (2020) 105988, http://dx.doi.org/10.1016/j.compositesa.2020.105988.

[4] E. Laukmanis, M. Janowski, S. Horn, J. Moosburger-Will, Effect of the interplay between fiber surface chemistry and sizing reactivity on fiber matrix interaction in carbon fiber reinforced epoxy resin, Compos. Interfaces (2022) 1–31, http://dx.doi.org/10.1080/09276440.2022.2068249.

[5] V. Rao, L.T. Drzal, Loss of curing agent during thin film (droplet) curing of thermoset material, J. Adhes. 35 (4) (1991) 245–249, http://dx.doi.org/10.1080/00218469108041011.

[6] D. Bryce, J. Thomason, L. Yang, Micromechanical and spectroscopic characterisation of the curing performance of epoxy resins in the microbond test, IOP Conf. Ser.: Mater. Sci. Eng. 942 (1) (2020) 012019, http://dx.doi.org/10.1088/1757-899x/942/1/012019.

[7] P. Zinck, H. Wagner, L. Salmon, J. Gerard, Are microcomposites realistic models of the fibre/matrix interface? Ii. physico-chemical approach, Polymer 42 (15) (2001) 6641–6650, http://dx.doi.org/10.1016/S0032-3861(00)00871-5.

[8] N. Rahmani, B. Willard, K. Lease, E.T. Legesse, S.A. Soltani, S. Keshavanarayana, The effect of post cure temperature on fiber/matrix adhesion of T650/cycom 5320-1 using the micro-droplet technique, Polym. Test. 46 (2015) 14–20, http://dx.doi.org/10.1016/j.polymertesting.2015.05.012.

[9] F. Meyer, G. Sanz, A. Eceiza, I. Mondragon, J. Mijović, The effect of stoichiometry and thermal history during cure on structure and properties of epoxy networks, Polymer 36 (7) (1995) 1407–1414, http://dx.doi.org/10.1016/0032-3861(95)95918-Q.

[10] R.F. Minty, L. Yang, J.L. Thomason, The influence of hardener-to-epoxy ratio on the interfacial strength in glass fibre reinforced epoxy composites, Composites A 112 (2018) 64–70, http://dx.doi.org/10.1016/j.compositesa.2018.05.033.

[11] H. Li, G. Chen, H. Su, D. Li, L. Sun, J. Yang, Effect of the stoichiometric ratio on the crosslinked network structure and cryogenic properties of epoxy resins cured at low temperature, Eur. Polym. J. 112 (2019) 792–798, http://dx.doi.org/10.1016/j.eurpolymj.2018.10.051.

[12] R. Unger, U. Braun, J. Fankhänel, B. Daum, B. Arash, R. Rolfes, Molecular modelling of epoxy resin crosslinking experimentally validated by near-infrared spectroscopy, Comput. Mater. Sci. 161 (2019) 223–235, http://dx.doi.org/10.1016/j.commatsci.2019.01.054.

[13] J. Thomason, An overview of some scaling issues in the sample preparation and data interpretation of the microbond test for fibre-matrix interface characterisation, Polym. Test. 111 (2022) 107591, http://dx.doi.org/10.1016/j.polymertesting.2022.107591.

[14] P. Laurikainen, S. Pötz, J. Jokinen, M. von Essen, M. Lindgren, P. Kallio, M. Kanerva, G. Oreski, E. Sarlin, High-throughput mechanical micro-scale characterization of composites and the utilization of the results in finite element analysis, in: Proceedings of the 18th European Conference on Composite Materials, European Society of Composite Materials, 2018.

[15] C.M. Sahagun, K.M. Knauer, S.E. Morgan, Molecular network development and evolution of nanoscale morphology in an epoxy-amine thermoset polymer, J. Appl. Polym. Sci. 126 (4) (2012) 1394–1405, http://dx.doi.org/10.1002/app.36763.

[16] S. Morsch, Y. Liu, P. Greensmith, S.B. Lyon, S.R. Gibbon, Molecularly controlled epoxy network nanostructures, Polymer 108 (2017) 146–153, http://dx.doi.org/10.1016/j.polymer.2016.11.050.

[17] P.V. Komarov, C. Yu-Tsung, C. Shih-Ming, P.G. Khalatur, P. Reineker, Highly cross-linked epoxy resins: An atomistic molecular dynamics simulation combined with a mapping/reverse mapping procedure, Macromolecules 40 (22) (2007) 8104–8113, http://dx.doi.org/10.1021/ma070702+.

[18] Z. Meng, M.A. Bessa, W. Xia, W. Kam Liu, S. Keten, Predicting the macroscopic fracture energy of epoxy resins from atomistic molecular simulations, Macromolecules 49 (2016) 9474–9483, http://dx.doi.org/10.1021/acs.macromol.6b01508.

[19] T. Hobbiebrunken, B. Fiedler, M. Hojo, M. Tanaka, Experimental determination of the true epoxy resin strength using micro-scaled specimens, Composites A 38 (3) (2007) 814–818, http://dx.doi.org/10.1016/j.compositesa.2006.08.006.

[20] N.J. Soni, P.-H. Lin, R. Khare, Effect of cross-linker length on the thermal and volumetric properties of cross-linked epoxy networks: A molecular simulation study, Polymer 53 (4) (2012) 1015–1019, http://dx.doi.org/10.1016/j.polymer.2011.12.051.

[21] C.E. Estridge, The effects of competitive primary and secondary amine reactivity on the structural evolution and properties of an epoxy thermoset resin during cure: A molecular dynamics study, Polymer 141 (2018) 12–20, http://dx.doi.org/10.1016/j.polymer.2018.02.062.

[22] M. Blanco, M.A. Corcuera, C.C. Riccardi, I. Mondragon, Mechanistic kinetic model of an epoxy resin cured with a mixture of amines of different functionalities, Polymer 46 (19) (2005) 7989–8000, http://dx.doi.org/10.1016/j.polymer.2005.06.117, Controlled Macromolecular Synthesis and Controlled Architectures - Supramolecular Polymer Assemblies.

[23] R. Hardis, J.L. Jessop, F.E. Peters, M.R. Kessler, Cure kinetics characterization and monitoring of an epoxy resin using DSC, Raman spectroscopy, and DEA, Composites A 49 (2013) 100–108, http://dx.doi.org/10.1016/j.compositesa.2013.01.021.

[24] N. Sbirrazzuoli, S. Vyazovkin, A. Mititelu, C. Sladic, L. Vincent, A study of epoxy-amine cure kinetics by combining isoconversional analysis with temperature modulated DSC and dynamic rheometry, Macromol. Chem. Phys. 204 (15) (2003) 1815–1821, http://dx.doi.org/10.1002/macp.200350051.

[25] C. Li, A. Strachan, Molecular scale simulations on thermoset polymers: A review, J. Polym. Sci. B: Polym. Phys. 53 (2) (2015) 103–122, http://dx.doi.org/10.1002/polb.23489.

[26] L.J. Abbott, K.E. Hart, C.M. Colina, Polymatic: a generalized simulated polymerization algorithm for amorphous polymers, Theor. Chem. Acc. 132 (2013) http://dx.doi.org/10.1007/s00214-013-1334-z, 1334.

[27] G.M. Odegard, B.D. Jensen, S. Gowtham, J. Wu, J. He, Z. Zhang, Predicting mechanical response of crosslinked epoxy using reaxff, Chem. Phys. Lett. 591 (2014) 175–178, http://dx.doi.org/10.1016/j.cplett.2013.11.036.

[28] B. Damirchi, M. Radue, K. Kanhaiya, H. Heinz, G.M. Odegard, A.C.T. van Duin, Reaxff reactive force field study of polymerization of a polymer matrix in a carbon nanotube-composite system, J. Phys. Chem. C 124 (37) (2020) 20488–20497, http://dx.doi.org/10.1021/acs.jpcc.0c03509.

[29] G.M. Odegard, S.U. Patil, P.P. Deshpande, K. Kanhaiya, J.J. Winetrout, H. Heinz, S.P. Shah, M. Maiaru, Molecular dynamics modeling of epoxy resins using the reactive interface force field, Macromolecules 54 (21) (2021) 9815–9824, http://dx.doi.org/10.1021/acs.macromol.1c01813.

[30] C.D. Petruczok, R. Yang, K.K. Gleason, Controllable cross-linking of vapor-deposited polymer thin films and impact on material properties, Macromolecules 46 (5) (2013) 1832–1840, http://dx.doi.org/10.1021/ma302566r.

[31] S. Ligot, E. Bousser, D. Cossement, J. Klemberg-Sapieha, P. Viville, P. Dubois, R. Snyders, Correlation between mechanical properties and cross-linking degree of ethyl lactate plasma polymer films, Plasma Process. Polym. 12 (6) (2015) 508–518, http://dx.doi.org/10.1002/ppap.201400162.

[32] HEXION Specialty Chemicals, EPON Resin 828, 2005, Technical data sheet.

[33] Huntsman Corporation, JEFFAMINE d-230 polyetheramine, 2007, Technical data sheet.

[34] P. Laurikainen, R. Dsouza, M. Kakkonen, M. Kanerva, E. Sarlin, Exploring the role of fibre sizing to the fatigue of glass fibre composites using a novel, reliable micro-fatigue test, Composites A (2023) 107425, http://dx.doi.org/10.1016/j.compositesa.2023.107425.

[35] J. Wehrs, G. Mohanty, G. Guillonneau, A.A. Taylor, D. Maeder, L. Philippe, S. Mischler, J.M. Wheeler, J. Michler, Comparison of in situ micromechanical strain-rate sensitivity measurement techniques, JOM 67 (8) (2015) 1684–1693, http://dx.doi.org/10.1007/s11837-015-1447-z.

[36] W. Oliver, G. Pharr, Measurement of hardness and elastic modulus by instrumented indentation: Advances in understanding and refinements to methodology, J. Mater. Res. 19 (1) (2004) 3–20, http://dx.doi.org/10.1557/jmr.2004.19.1.3.

[37] M. Bergdorf, S. Baxter, C.A. Rendlman, D. Shaw, Desmond/GPU Performance as of November 2016, Technical Report, D. E. Shaw Research, 2016, URL https://www.deshawresearch.com/publications.

[38] OPLS4, Schrödinger, Inc., 2021.

[39] C. Lu, C. Wu, D. Ghoreishi, W. Chen, L. Wang, W. Damm, G.A. Ross, M.K. Dahlgren, E. Russell, C.D. Von Bargen, R. Abel, R.A. Friesner, E.D. Harder, OPLS4: Improving force field accuracy on challenging regimes of chemical space, J. Chem. Theory Comput. 17 (7) (2021) 4291–4300, http://dx.doi.org/10.1021/acs.jctc.1c00302, PMID: 34096718.

[40] K. Roos, C. Wu, W. Damm, M. Reboul, J.M. Stevenson, C. Lu, M.K. Dahlgren, S. Mondal, W. Chen, L. Wang, R. Abel, R.A. Friesner, E.D. Harder, OPLS3e: Extending force field coverage for drug-like small molecules, J. Chem. Theory Comput. 15 (3) (2019) 1863–1874, http://dx.doi.org/10.1021/acs.jctc.8b01026, PMID: 30768902.

[41] K.H. DuBay, M.L. Hall, T.F. Hughes, C. Wu, D.R. Reichman, R.A. Friesner, Accurate force field development for modeling conjugated polymers, J. Chem. Theory Comput. 8 (11) (2012) 4556–4569, http://dx.doi.org/10.1021/ct300175w, PMID: 26605615.

[42] P.J. Flory, Molecular size distribution in three dimensional polymers. i. Gelation1, J. Am. Chem. Soc. 63 (11) (1941) 3083–3090, http://dx.doi.org/10.1021/ja01856a061.

[43] W.H. Stockmayer, Theory of Molecular Size Distribution and Gel Formation in Branched Polymers II. General Cross Linking, J. Chem. Phys. 12 (4) (1944) 125–131, http://dx.doi.org/10.1063/1.1723922.

[44] P.V. Laurikainen, E.L. Sarlin, Cut-off scale and complex formation in density functional theory computations of epoxy-amine reactivity, ACS Omega 6 (44) (2021) 29424–29431, http://dx.doi.org/10.1021/acsomega.1c03229.